

UNIVERSITY OF CALIFORNIA, BERKELEY

University of California
Berkeley
Geotechnical Engineering

LUNAR SURFACE ENGINEERING PROPERTIES EXPERIMENT DEFINITION

by

James K. Mitchell
Richard E. Goodman
William N. Houston
Paul A. Witherspoon

SECOND QUARTERLY REPORT

Contract Number NAS 8-21432

Control Number DCN 1-8-28-00056 (IF)

February 20, 1969

Submitted to

National Aeronautics and Space Administration

George C. Marshall Space Flight Center

Space Sciences Laboratory Series 10, Issue 6

INTRODUCTION

The objectives of the research under this contract are to define geological and engineering problems associated with lunar exploration that depend on the knowledge of the mechanical properties of soil and rock for solution and to perform critical evaluation of available information relating to the composition, structure, and engineering properties of lunar surface materials. This information is being used to recommend instrumentation and delineate investigations for determining the strength, deformational characteristics (and general engineering behavior of lunar materials under in-situ environmental conditions) during Apollo missions.

The effective date of this contract was June 20, 1968. This quarterly report describes progress for the period October 1 through December 31, 1968. Effort during this period was devoted to the following studies:

I. Lunar soil simulation

(W. N. Houston, L. I. Namiq, and J. K. Mitchell)

II. Friction angle of lunar surface soils estimated from boulder tracks

(H. J. Hovland and J. K. Mitchell)

III. Trafficability of the lunar surface

(J. B. Thompson and J. K. Mitchell)

IV. Chemical impregnation techniques as related to lunar engineering applications

(T. S. Vinson and J. K. Mitchell)

V. Failure of a borehole in soil or rock under dilatometer loading and under borehole jack loading

(T. K. Van and R. E. Goodman)

Appendix — Detailed description of model studies

(K. Drozd, T. K. Van, and R. E. Goodman)

VI. Studies on fluid conductivity of lunar surface materials

(D. F. Katz, D. R. Willis, and P. A. Witherspoon)

Appendix A

Appendix B

This report was prepared by the University of California, Berkeley, under Contract Number NAS 8-21432, Lunar Surface Engineering Properties Experiment Definition, for the George C. Marshall Space Flight Center of the National Aeronautics and Space Administration. The work was administered under the technical direction of the Space Sciences Laboratory of the George C. Marshall Space Flight Center.

I. LUNAR SOIL SIMULATION

(W. N. Houston, L. I. Namiq, J. K. Mitchell)

1. INTRODUCTION

As described in the preceding quarterly report, a simulated lunar soil has been prepared for study of lunar soil properties in general and study of the use of Apollo hand tools for determination of mechanical properties in particular. Activities during this quarter have included (1) further processing of the basic test soil; (2) performance of confined compression tests, triaxial shear tests, and trenching tests for cohesion determination; (3) study of soil placement techniques; (4) performance of boot imprint tests; (5) performance of penetration resistance tests; and (6) reduction, analysis, and summarization of data. These activities are described in detail in the following section.

2. SOIL PROCESSING

To obtain the desired gradation for the simulated lunar soil it was necessary to mix a coarse basalt sand with a fine powder, obtained by grinding the coarser sand in a roller mill. It was found that the percentage of plus No. 8 in the stock coarse material varied erratically and that some particles as large as one inch were present. Therefore it was necessary to sieve approximately one ton of material over the No. 8 sieve before proceeding with the mixing. This process and subsequent mixing resulted in a reduction of the amount larger than the No. 8 sieve size to about 4 or 5 per cent.

Mixing was accomplished by rolling sealed 55-gal drums in a drum roller for at least 30 minutes. The barrels were filled to about one-third capacity with weighed components. After mixing, the gradation was checked to determine uniformity of mixing. The per cent passing the No. 200 sieve was always checked by wet sieving. Several hundred pounds were mixed in this way and the average gradation obtained is shown in Figure 1. This curve is essentially the same as the one shown in Fig. 1-1 of the preceding quarterly report, except that the per cent plus No. 8 is somewhat less for the soil currently being tested.

3. SOIL PLACEMENT

Several methods of placement in the test bin (2' x 2' x 2') were tried including (1) sprinkling through a sieve held just above the soil surface, (2) lifting a sieve through the soil, and (3) sprinkling directly on the soil surface from a constant height of about 3/4 inch. The third method was found to be the most satisfactory. The first method is unacceptable because contact between the sieve and the placed soil is unavoidable. This contact causes disturbance and compression of the deposited soil. The second method is unsatisfactory because the arching and cohesive properties of the soil require that the sieve be extremely coarse or it will not pass through the soil. The third method seems slightly preferable to deposition from a mechanical hopper because the quantity of material to be sprinkled must be low and the height of drop small to obtain low initial densities. The sprinkling method described gives an average density of 1.32 g/cc for the top 1-1.5 inches. The lateral uniformity of density

obtained was checked by filling four containers, side by side, to a depth of 1-1.5 inches. The lateral variation in density was only about 1 per cent which is quite acceptable.

The sprinkling method was tried with heights of drop up to 6 inches. The relationship between height of drop and average density for the top 1-1.5 inches is shown in Figure 2.

4. DETERMINATION OF ϕ

The variation of ϕ with average density has been determined by means of vacuum triaxial tests on air-dried material at confining pressures ranging from 0.04 kg/cm² to 0.15 kg/cm². The lowest confining pressure used was 0.04 kg/cm² because the membrane corrections became too large compared to the strength for lower confining pressures. A confining pressure larger than 0.15 kg/cm² causes too much densification during isotropic consolidation prior to shearing. Confining pressures much less than 0.15 kg/cm² must be used for the very loose specimens if excessive densification is to be avoided. The reported densities are the values obtained after consolidation but before shearing.

The range in confining pressure used for vacuum triaxial tests corresponds to a depth range of about 160 to 600 cm for the actual lunar surface. An effort will be made to measure ϕ values for confining pressures corresponding to much smaller depths by performing sliding block tests to determine soil friction.

As expected, the stress-strain curves for most of the specimens, especially the looser ones, exhibited a plastic-type behavior. A typical stress-strain curve for a triaxial test is shown in Figure 3.

A Mohr envelope for specimens tested at an initial density of 1.7 g/cc is shown in Figure 4 and the variation of ϕ value with density is shown in Figure 5. It is quite difficult to perform a triaxial test on a specimen with an initial density less than 1.6 g/cc because even small confining pressures cause densification. Probable values of ϕ for densities less than 1.6 g/cc have been obtained by extrapolation.

A high degree of accuracy for ϕ values is difficult to obtain in testing very loose specimens at very low confining pressures, due to the relatively low strengths. Subsequent testing will be directed toward narrowing the range of uncertainty associated with the reported values. Nonetheless, the values obtained are consistent with those suggested for actual lunar soil as a result of Surveyor tests.

5. DETERMINATION OF COHESION

The variation of cohesion with average density has been determined by excavating trenches with vertical walls in samples with different density. This method is preferable to obtaining the cohesion from usual strength test results because of the difficulties in determining strengths of materials with very low cohesion at very small confining pressures, where the failure envelope may be in error by as much as 100 per cent. By using the vertical trench wall method, it is believed that errors may be kept as low as about 25 per cent.

Many failures of vertical trench walls were studied and it was found that the sliding block was essentially a Coulomb wedge. Tension cracks usually appeared at the surface, but they did not appear to cover an

appreciable percentage of the slip surface. Figure 6 shows a photo of a trench excavation for cohesion determination. A tension crack appears about midway along the length of the wall. The wall height shown in the photo is about two inches. Failure has occurred along part of the wall. The procedure for calculating the cohesion consisted of (1) measuring the wall height at which failure developed, (2) assuming Coulomb wedge failure, (3) assigning an appropriate value of ϕ and calculating the shearing resistance force due to friction, and (4) assigning the remaining resistance required for stability to cohesion. The calculated value of cohesion was found not to be highly sensitive to either the value of ϕ assigned or the inclination of the failure surface.

A relationship between cohesion, c , and density, ρ , has been obtained by this method for a limited range of densities and is shown in Figure 7. It should be noted that the value of cohesion is dependent on the value of the air-dry water content. Additional testing will be done to determine this dependency.

It is of interest to note that a vertical wall of 2-inch height for terrestrial soil corresponds to a vertical wall of about 12-inch height for lunar soil of the same density and cohesion, due to reduced gravity stresses. This observation indicates that it will probably not be difficult to excavate around a "cake" of lunar soil, forming four vertical walls. However, additional testing and analysis is needed to assess the chances of being able to scoop the "cake-like" piece of soil up for a density determination without breaking it apart.

The conclusion appears warranted that the simulated lunar soil exhibits cohesion values appropriate for the range estimated for the actual lunar soil from Surveyor test results.

6. DETERMINATION OF DENSITY, VERTICAL STRESS, AND SHEAR STRENGTH
VARIATIONS WITH DEPTH

A 16-inch layer of soil was placed in the 2' x 2' x 2' box for the purpose of conducting trenching tests and other model tests. Placement was accomplished by sprinkling from a height of about 3/4 inch as described in the Soil Placement section. In order to estimate the variations of vertical stress and shear strength with depth it was necessary to know the variation of density with depth. Confined compression tests were performed on specimens with different initial densities to provide compressibility data to be used in computing the needed density values. The tests were carried out using a 2.8-inch diameter teflon-lined consolidation ring. The initial specimen height was one inch.

The compression curves obtained from these tests are shown in Figure 8. The values of initial density, ρ_i , are shown on the figure. The curves show that the rebound on load release is extremely small. The same data plotted in terms of stress and density are shown in Figure 9. The curves marked L and T were obtained by extrapolation and are discussed in the following paragraphs.

It is of special interest to note that all the curves merge at a density of 1.9 g/cc and a stress of about 1000 g/cm², and that the semi-log plot shown on Figure 9 indicates a linear variation of density with log pressure. These facts make extrapolation and interpolation for other initial densities possible.

The placement method used produces a density near the surface of about 1.32 g/cc. Therefore it was desirable to obtain a compression curve with this initial density. Although confined compression specimens could

be placed at this initial density, they could not be tested without significantly increasing the initial density, because the process of scraping a plane surface on the top of the specimen produced densification. Therefore it was necessary to obtain the probable position of this compression curve by extrapolation. Fortunately, the data in Figure 9 show that the desired curve should be a straight line merging with the other curves at a stress of about 1000 g/cm². A second point on the curve was obtained by using the known value of initial average density at the surface and assigning an average value of vertical stress due to the weight of a surficial layer. The compression curve thus obtained is shown in Figure 9 and marked "T" to signify its applicability to the *terrestrial* soil in the test box.

The straight-line compression curves shown in Figure 9 have equations of the form:

$$\rho = K_1 + K_2 \log_{10} \sigma \quad (1)$$

where σ = vertical compressive stress

ρ = corresponding density

K_1 = value of ρ for $\sigma = 1$

K_2 = change in ρ for one log cycle change in σ .

Equation (1) can be written in exponential form giving:

$$\sigma = e^{\frac{K_3(\rho - K_1)}{K_2}} \quad (2)$$

$$\text{where } K_3 = \frac{2.303}{K_2}$$

It is possible to relate the density to the depth of deposit as follows. First, it may be assumed that a layer of soil of differential thickness, dz , is deposited on the bottom of the box at an initial density, ρ_i , and that subsequent densification is due only to the compressive stresses applied by the weight of additional material placed on top. The increase in stress, $d\sigma$, due to the addition of a layer of thickness dz is equal to the thickness of the layer times its density, ρ_i .

$$d\sigma = \rho_i dz \quad (3)$$

In order to develop a relationship between density and depth, it is necessary to substitute an expression for $d\sigma$ in terms of ρ obtained by differentiating Equation (2).

$$d\sigma = K_3 e^{K_3(\rho - K_1)} d\rho \quad (4)$$

Substitution in Equation (3) gives

$$K_3 e^{K_3(\rho - K_1)} d\rho = \rho_i dz$$

Integration gives the following expression

$$\frac{1}{\rho_i} e^{K_3(\rho - K_1)} = z + c \quad (5)$$

The constant of integration, c , can be evaluated by applying the boundary condition that $\rho = \rho_i$ for $z = 0$; therefore,

$$c = \frac{1}{\rho_i} e^{K_3(\rho_i - K_1)} \quad (6)$$

For convenience the constant c is retained in Equation (5), which can be rewritten as,

$$\rho = \frac{\ln[\rho_i(z + c)]}{K_3} + K_1 \quad (7)$$

Equation (7) is the desired relationship between density and depth. There is one additional boundary condition which facilitates the evaluation of ρ_i . The average density, ρ_{ave} , of the 16-inch layer of soil was determined by measuring its total volume and weight after placement and found to be 1.50 g/cc. The use of this value in evaluating ρ_i requires an expression for ρ_{ave} in terms of z and ρ_i . The average density for any depth of material, z (i.e., the average density for all material between the surface and depth z), can be obtained by integrating Equation (7) with respect to z and dividing the result by z .

$$\left(\rho_{ave}\right)_z = \frac{\int \left\{ \frac{\ln[\rho_i(z + c)]}{K_3} + K_1 \right\} dz}{z}$$

Integration gives

$$\left(\rho_{ave}\right)_z = \frac{1}{K_3} \left\{ \left(1 + \frac{c}{z}\right) \left[\ln[\rho_i(z + c)] - 1 \right] - \frac{c}{z} \left[\ln \rho_i c - 1 \right] \right\} + K_1 \quad (8)$$

Equation (8) is the desired relationship between ρ_{ave} , ρ_i , and z . Examination of curve "T" in Figure 9 shows that $K_1 = 1.20$ and $K_2 = 0.223$ from which $K_3 = 10.32$ can be calculated. Using these compression parameters

and the condition that $\rho_{ave} = 1.50$ g/cc for $z = 15.7$ inches (39.8 cm), solution of Equation (8) for ρ_i gives $\rho_i = 1.30$ g/cc. This value of ρ_i was then used in Equations (7) and (8) to compute the variations of ρ and ρ_{ave} with depth as shown in Figure 10(a). The vertical stress at any depth z is given by

$$\sigma = z \cdot \left(\rho_{ave} \right)_z \quad (9)$$

Equation (9) and the data in Figure 10(a) were used to compute the vertical stress variation with depth shown in Figure 10(b). The agreement between the computed stresses and densities shown in Figures 10(a) and (b) and the stress-density relationship given by curve "T" of Figure 9 indicates that the method used and assumptions made are acceptable. An additional check is provided by the fact that the computed value of ρ_{ave} for the upper few centimeters compares very well with the value obtained experimentally.

It should be noted that precise agreement between the computed density-depth relationship shown in Figure 10 and that implied by the confined compression curve shown in Figure 9 should not be expected for very small depths because two modes of densification are involved. The actual soil placement process involves densification due largely to vibration — resulting in a layer of finite thickness at the surface with essentially constant density. This surface layer is then subsequently compressed in accordance with the relationships depicted in Figure 9. However, the calculated density-depth relationship shown in Figure 10(a) is based on the assumption that all densification is by static compression

alone; i.e. the initially deposited surface layer of density ρ_i has only differential thickness. The difference caused by this assumption becomes negligible after the stress exceeds a few grams per cm^2 .

Using the data presented in Figures 5, 7, and 10(a,b) it was possible to compute the variation of cohesion, c , and shear strength on a horizontal plane, s_h , with depth, as shown in Figure 10(c). Figure 10(c) shows that the shear strength variation is nearly linear, although not precisely so, and that the contribution due to cohesion is appreciable for the first 10 to 15 cm.

A similar analysis was made to determine the probable variation of density, vertical stress, and shear strength with depth for the actual lunar surface under conditions of reduced gravity. As in the case of the terrestrial section of soil, it was necessary to determine a compression curve relating density and stress. The position of this curve was determined by assuming that the lunar soil fits the compressibility pattern established in Figure 9. It was further assumed that the average density of the top 40 cm of lunar soil is 1.50 g/cc, in accordance with estimates of this property from Surveyor data. Using these two assumptions it was possible to obtain a probable position for the compressibility curve as shown in Figure 9 by the curve marked "L" to signify its applicability to the lunar soil under reduced gravity. The compressibility curve was found by making a trial and error solution for K_1 , K_3 , and ρ_i .

Before discussing the trial and error solution, a preliminary observation can be made which shows that the curve "L" must be appreciably flatter than curve "T." If ρ_{ave} for the top 40 cm is 1.50 g/cc, then the vertical compressive stress due to gravity at this depth must be:

$$\sigma_{(z = 40 \text{ cm})} = (1.50)(40)(1/6) \approx 10 \text{ g/cm}^2$$

since the gravity-induced stress is only 1/6 of the value for the same soil on the earth's surface. [Note: Although stresses are, by definition, expressed in dynes/cm² in the metric system, expression in grams/cm² is used herein for both terrestrial and lunar applications because of the better "feel" for behavior that is obtained with these units. For computation of lunar gravitational forces, a density equal to 1/6 of the mass density is used.] In order that ρ_{ave} be equal to 1.50 g/cc for the top 40 cm, it is necessary that the value of ρ at a depth of 40 cm be appreciably greater than 1.50 g/cc. The preceding observation shows that the value of $\rho = 1.56 \text{ g/cc}$ for $\sigma = 10 \text{ g/cm}^2$ shown by Curve L is a reasonable value. The same argument can be used to show that ρ_i for the actual lunar surface should be greater than ρ_i for the terrestrial section prepared in the test bin if both sections have the same value of ρ_{ave} . This relationship is necessary because the increase in density with increase in depth is smaller for the lunar soil due to reduced gravity stresses.

Modifications in the derivations of expressions for ρ and ρ_{ave} to account for reduced gravity consist simply of substituting $\rho_i/6$ for ρ_i in cases where gravity stresses are being calculated. Thus, the expression for $d\sigma$, the incremental stress increase due to the weight of a small additional surface layer, as given by Equation (3) becomes:

$$d\sigma = (\rho_i/6) dz \quad (3a)$$

and the desired relationships between ρ , ρ_{ave} , and depth are:

$$\rho = \frac{\ln[(\rho_i/6)(z+c)]}{K_3} + K_1 \quad (7a)$$

and

$$\rho_{ave} = \frac{1}{K_3} \left\{ \left(1 + \frac{c}{z} \right) \left[\ln[(\rho_i/6)(z+c)] - 1 \right] - \frac{c}{z} \left[\ln \frac{\rho_i c}{6} - 1 \right] \right\} + K_1 \quad (8a)$$

However, the boundary condition that $\rho = \rho_i$ for $z = 0$ holds for the lunar soil section as it did for the terrestrial soil section; therefore the expression for the constant of integration, c , is:

$$c = \frac{6}{\rho_i} e^{K_3(\rho_i - K_1)} \quad (6a)$$

Solutions of Equations (7a) and (8a) gave the best agreement between the computed stress-density relationship and the confined compression curve when $K_3 = 13.55$, $K_1 = 1.39$, and $\rho_i = 1.37$ g/cc. Using these values the distributions shown in Figure 11(a) were determined. The variations of vertical stress, cohesion, and shear strength with depth shown in Figure 11(b,c) were obtained by combining data from Figures 11(a), 5, and 7.

Under conditions of lunar gravity the cohesion, c , constitutes a very significant percentage of the total shear strength on a horizontal plane, s_h , as shown by Figure 11(c). However, the significance of the cohesion component is likely to be much less in the case of shear induced by surface loading, because of the additional confinement provided by applied direct stresses. For example, although it is difficult to estimate the

minimum contact pressure to be exerted by the wheels of lunar roving vehicles at this point in time, it seems likely that this pressure will be greater than 0.75 psi (absolute pounds force). This contact stress will, of course, both cause some densification and dissipate with depth. Assuming that most of the deformation occurs within the top 15 to 20 cm of material, it is reasonable to assume that the average normal stress within most of this zone is at least 0.45 psi (about 30 g/cm²). This value of normal stress would cause densification of the lunar soil to a density of about 1.64 g/cm² for which cohesion, $c = 4.6 \text{ g/cm}^2$ and $s_h = 27.4 \text{ g/cm}^2$. Therefore a conservative estimate of the percentage contribution of cohesion to the shear strength is about 17% for this case.

7. PENETRATION RESISTANCE

Penetration resistance measurements are being considered as a means by which astronauts may gather data leading to the assessment of lunar surface soil properties. Approximate values of resistance are needed for design of penetrometers that may be utilized on Apollo missions. An important application of penetration resistance data may be for the design of lunar roving vehicles. The Corps of Engineers utilizes cone penetrometer data for cohesionless soils in trafficability analysis by obtaining the slope, G , of the penetration resistance (in psi) versus depth of penetration (in inches). Although the lunar soil is not considered to be completely cohesionless, it may still be possible to utilize such a modulus. As a first step toward obtaining penetration data for a simulated lunar soil, a series of rods of different sizes were used as penetrometers in the soil represented by Figure 10. The rod sizes and the G values obtained from them are shown in Table I-1. All rods had flat ends. In most cases, the rods were simply allowed to sink under their own weight.

TABLE I-1
SUMMARY OF ROD PENETRATION DATA

Rod Diameter (in.)	Area (in. ²)	G #/in. ³
0.50	0.1965	1.9
0.50	0.1965	2.5
0.90	0.636	1.8
0.95	0.71	2.5
1.35	1.43	2.2
1.35	1.43	2.3
2.0	3.14	1.5
4.0	12.6	1.9
Ave. $\approx 2.1 \pm 0.5$		

The rod penetration data in Table I-1 show an average value of $G = 2.1 \text{ \#/in.}^3$. It appears that G is not appreciably affected by the rod size, but the scatter in the data is about $\pm 0.5 \text{ \#/in.}^3$ so the effect of rod size may be obscured. An idea of the effect of rod size can be obtained by considering the rod to be a square footing and equating its bearing capacity to the penetration resistance.

$$q_{ult} = \frac{b\gamma}{2} N_{\gamma} K_1 + d\gamma N_q + cN_c \quad (10)$$

where

q_{ult} = bearing capacity

b = width of footing

γ = unit weight

N_γ = function of ϕ

K_1 = foundation shape factor

d = depth of footing

N_q = function of ϕ

c = cohesion

N_c \approx constant (relatively insensitive to depth change)

The constants N_γ and N_ϕ are of about the same magnitude and are considerably larger than N_c . This bearing capacity equation shows that the depth term should predominate after the depth exceeds a few rod diameters and that the penetration resistance should become essentially proportional to depth. However, the rod diameter obviously should have a significant effect on penetration resistance at very shallow depths.

A first approximation of the value of G applicable to the actual lunar surface (reduced gravity) can be obtained by assuming the penetration resistance is proportional to the shear strength. A comparison of Figures 10 and 11 shows that the rate of increase in shear strength with depth for the simulated lunar soil is about five times the rate of increase for the probable lunar profile. Therefore,

$$G_{\text{Earth}} \sim 5 G_{\text{Moon}}$$

or

$$G_{\text{Moon}} \approx \frac{2.1}{5} = 0.42 \pm 0.1 \text{ \#/in.}^3$$

Note that the units for G_{Moon} are absolute pounds force per cubic inch.

If $G_{\text{Moon}} \approx 0.4 \text{ \#/in.}^3$, then a 10# (absolute pounds force) vertical load could be used to drive a 1-inch-diameter penetrometer about 30 inches (75 cm) into the lunar soil. Therefore, penetrometers of 1-inch-diameter and smaller can probably be used successfully with much smaller loads.

An additional observation of interest made during the performance of the penetration tests was that the maximum downward thrust that could be exerted on a rod was about 45 pounds — with hands at chest level and about 15 inches from the chest.

Figures 5, 7, and 11 show that the initial density profile of the lunar surface will probably have a very pronounced effect on the compressibility as well as the shear strength. Therefore the effect of variable density is of importance. It is of interest to estimate the possible effect of changing the average density about 10 per cent (say 1.5 to 1.65) on the value of G . The cohesion would be more or less uniformly increased, but this increase would have little effect on the rate of increase in shear strength with depth. However, Figure 5 shows that $\tan \phi$ might increase by about 20 per cent. Assuming $\tan \phi$ were proportional to G , a 20 per cent increase in G would result. Similarly a 5 per cent increase in density might cause an increase of about 10 per cent in G . This comparison indicates that measured G values for the lunar surface material may, in fact, be good indicators of variation in density and shear strength.

8. ANALYSIS OF FOOTPRINT DATA

Figures 12 and 13 show photographs and sketches of a boot imprint made by stepping down on the surface of the simulated soil with a weight of 180 pounds. The profile of the simulated soil is represented in Figure 10. The dimensioned sketch of the boot used (see Figure 13) shows that the bearing area is about 45 sq in. Although the stress distribution under the boot was not expected to be uniform, the average stress was 4 psi. The observed maximum depth of the footprint was 3.5 inches.

In order to provide a basis for comparing the depth of footprint in the simulated lunar soil and in the actual lunar soil, it was assumed that the boot was a 4-inch-wide strip footing and that the contact stress dissipated with depth according to elastic theory (Boussinesq solution). The variation of the existing vertical stress and the total vertical stress including surface load with depth is shown in Figure 14(a). The magnitude of stress due to surface load which still exists at the bottom of the box shows that boundary effects were appreciable for this depth of soil. This point is discussed further subsequently. The compressibility curve T of Figure 9 was used to determine the variation of final density with depth as shown in Figure 14(b). The vertical strain, ϵ_v , was calculated at various depths by

$$\epsilon_v = 1 - \frac{\rho_1}{\rho_2}$$

where ρ_1 = original density

ρ_2 = final density

and plotted in Figure 15. The area to the left of the curve gives the predicted depth of footprint, 2.3 inches. The fact that the predicted

depth of footprint, 2.3 inches, does not compare well with the observed value, 3.5 inches, indicates that the assumption of stress dissipation by elastic theory may not be good. Furthermore, shear deformations were neglected in making this estimate; only deformations due to compression were considered. Nevertheless, the method used serves as a basis for comparing depth of footprint in the test bin and the corresponding depth of footprint for the lunar surface.

The prediction was repeated for the actual lunar surface using the properties given in Figures 9 and 11, except that the force applied to the boot was assumed to be 275 earth lb (46 lunar lbs) giving a surface contact stress of about 1 psi, assuming the same contact area of 45 in.². The results of this prediction are shown in Figure 16. The predicted depth of footprint was 1.8 inches. Comparison shows that:

$$\frac{\Delta_{\text{Lunar surface}}}{\Delta_{\text{Terrestrial surface}}} = \frac{1.8}{2.3} = 0.78$$

This ratio can now be applied to the observed depth of footprint for the simulated soil in the test bin. However, the observed depth must first be corrected for the boundary effects exerted by the bottom of the box. Figure 15 indicates that the depth of footprint might have been about 20 per cent greater had the box been infinitely deep, in which case the observed depth of footprint would have been about 4.2 inches. Using this value, a reasonable estimate of the depth of footprint for the actual lunar surface, with $\rho_{\text{ave}} = 1.50 \text{ g/cc}$, can be obtained by

$$\text{Depth} = (4.2)(0.78) = 3.3 \text{ inches}$$

The depth of footprint for three lunar soil profiles with ρ_{ave} varying from 1.40 to 1.60 g/cc were compared by assuming reasonable compressibility parameters. The results are shown in Table 2 below.

TABLE I-2

ρ_{ave} (before loading) in g/cc	Probable Depth of Footprint in Inches
1.40	4.3
1.50	3.3
1.60	2.5

These comparisons indicate that depth of footprint may be useful as an indicator of density and shear strength. This conclusion is only tentative, however, and will be checked by conducting more footprint tests on soils with different ρ_{ave} values and by making more refined analyses, including, for example, shear deformations.

9. PLANNED STUDIES FOR NEXT QUARTER

Additional triaxial tests are required to establish the ϕ -density relationship over a wider range of densities and to decrease the uncertainty associated with ϕ values reported herein. A small number of plane strain tests will also be performed to determine the magnitude of any differences in ϕ values for plane strain and triaxial tests.

Trenching tests for cohesion determination will be performed to establish the cohesion-density relationship with more certainty and over a wider range of densities. The effect of variation in air-dried moisture content on cohesion will also be investigated.

More confined compression tests will be performed in an effort to expand the pattern presented in Figure 9 to cover a wider range of initial densities.

Additional penetration tests will be made on soils with different soil density profiles to study the variation of G with shear strength and ρ_{ave} and to determine the extent of the effect of rod size on G . Penetration tests will be performed using a 30-degree cone. Some dynamic penetration observations will also be made.

The performance of more boot imprint tests in deeper soils with different density profiles will allow study of the effect of density and shear strength on footprint depth, mode of deformation, and tension crack pattern. A more rigorous analysis of boot imprint deformations using the finite element method is also planned.

GEOTECHNICAL ENGINEERING
UNIVERSITY OF CALIFORNIA

GRADING ANALYSIS

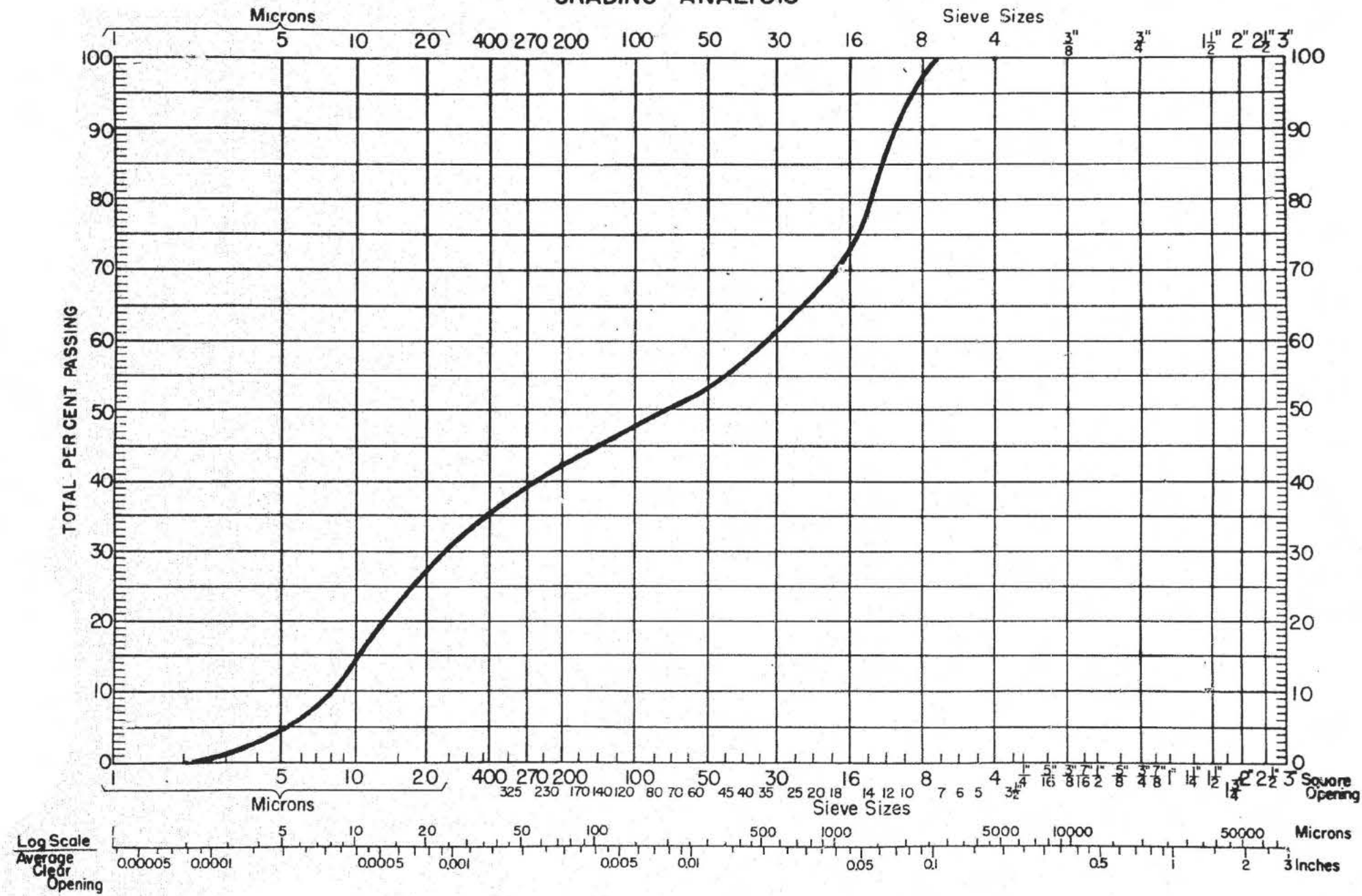


FIGURE 1. Gradation curve for basic test soil

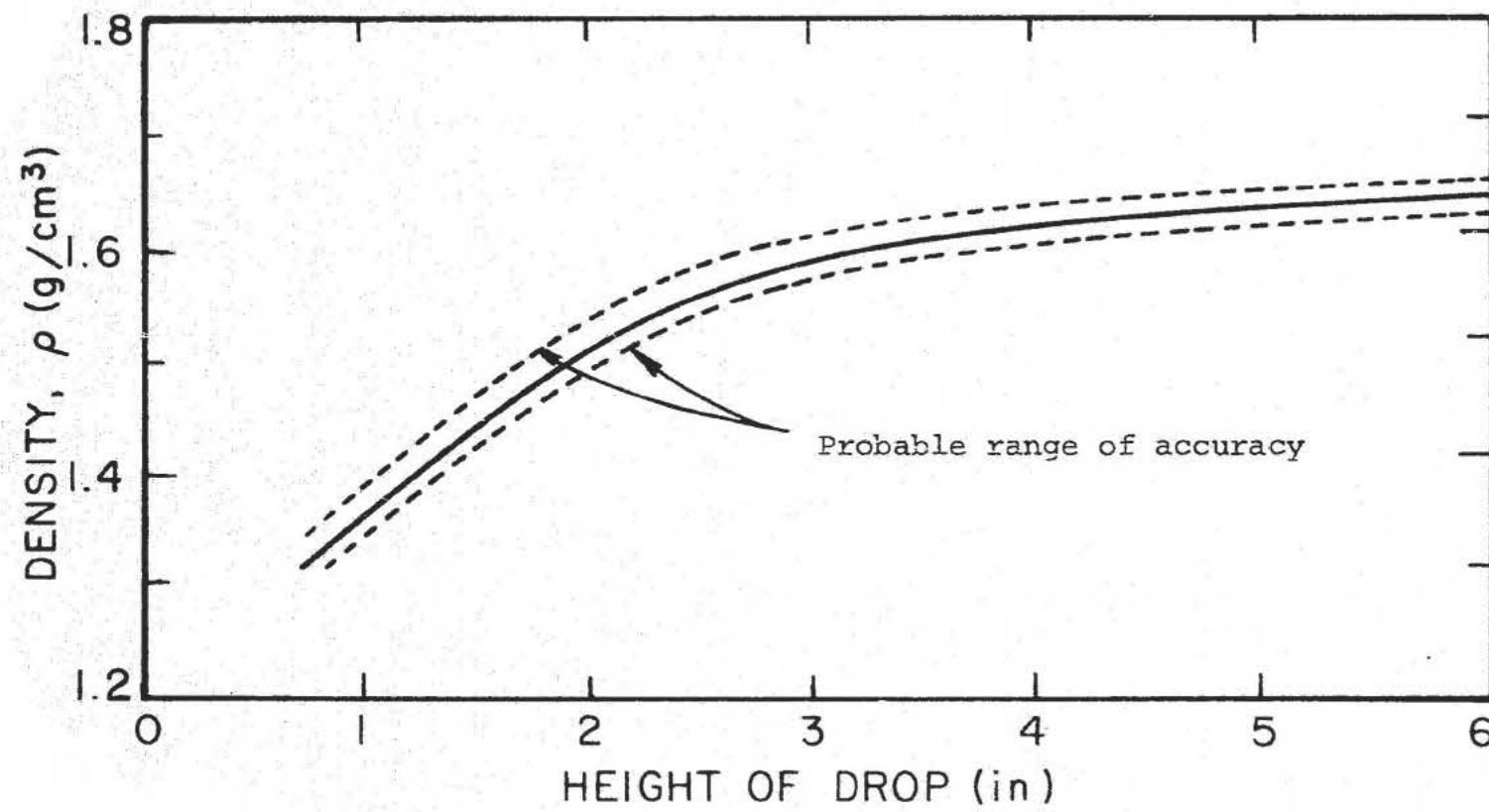


FIGURE 2. Variation of density with height of drop during placement

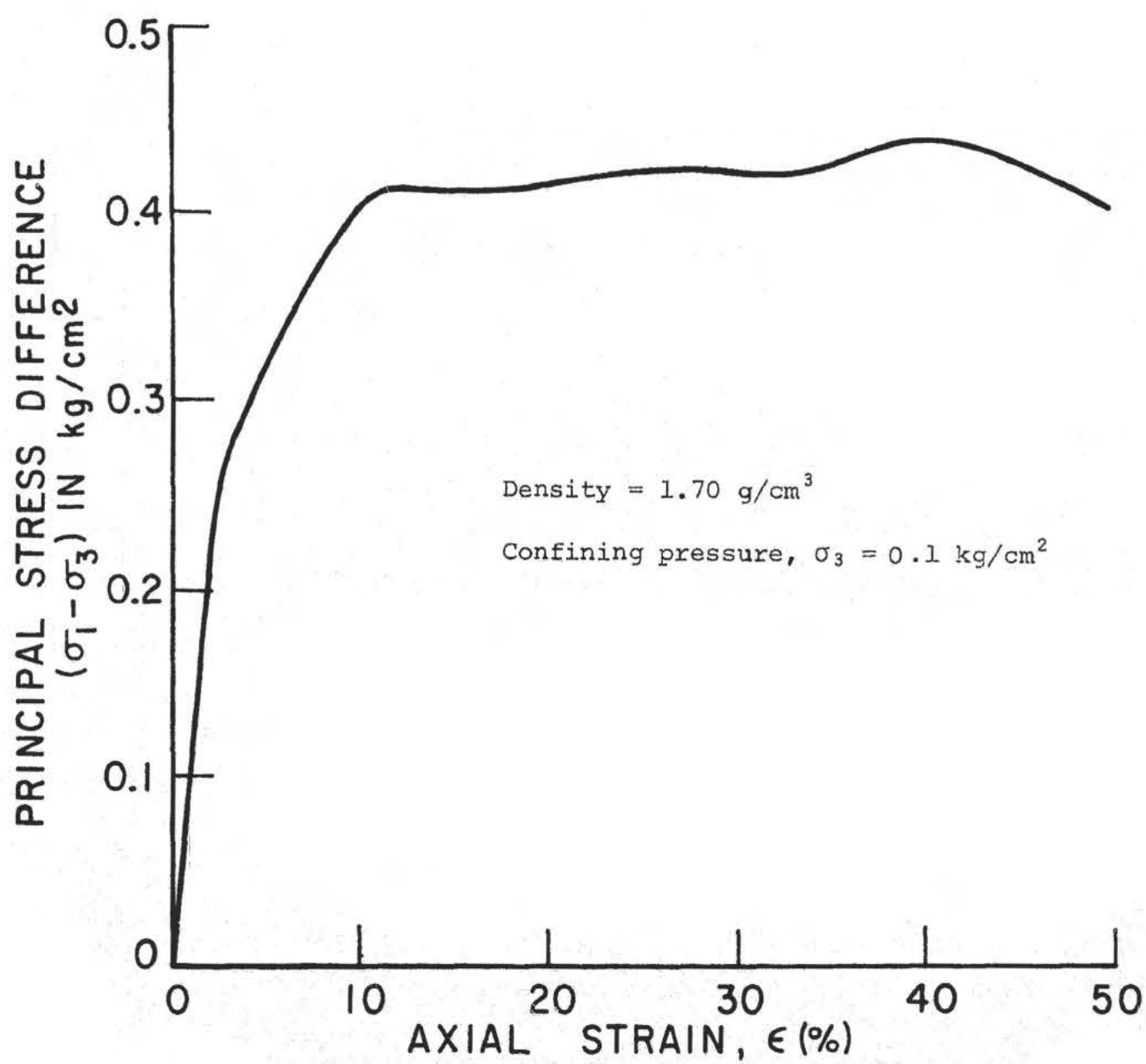


FIGURE 3. Triaxial stress-strain curve

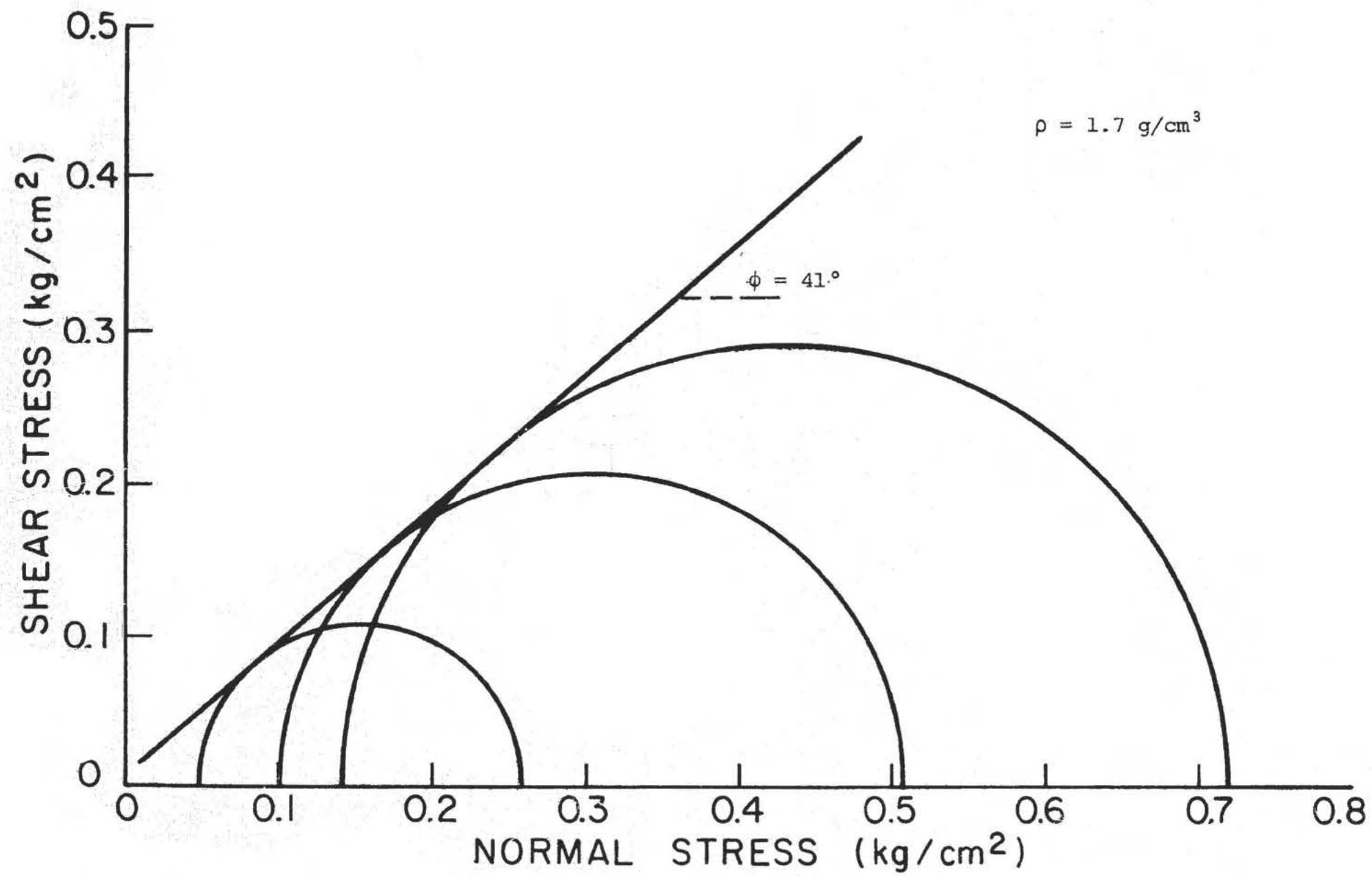


FIGURE 4. Mohr envelope for density = 1.7

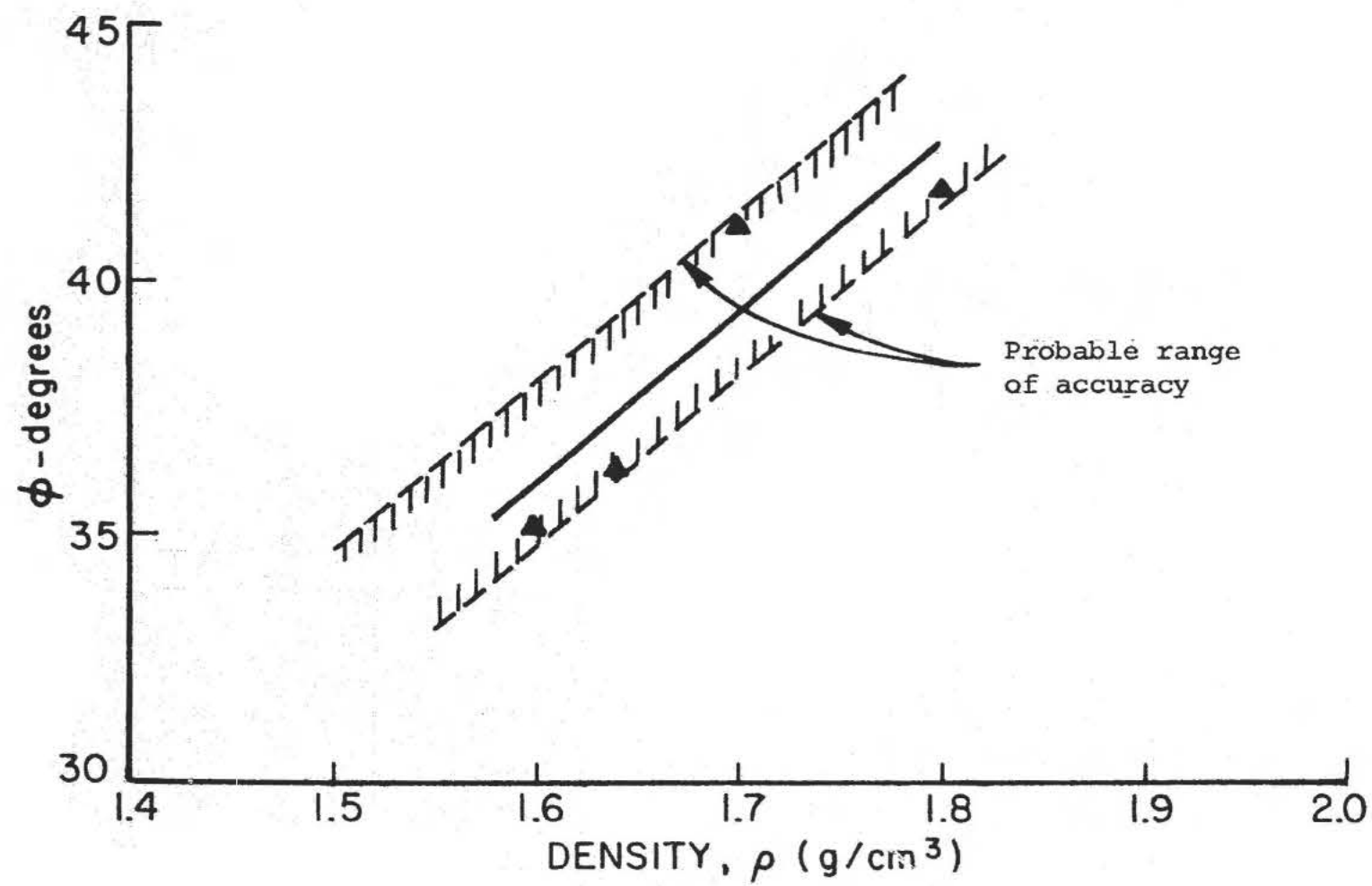


FIGURE 5. ϕ vs density



FIGURE 6 . Trench excavation for cohesion determination.

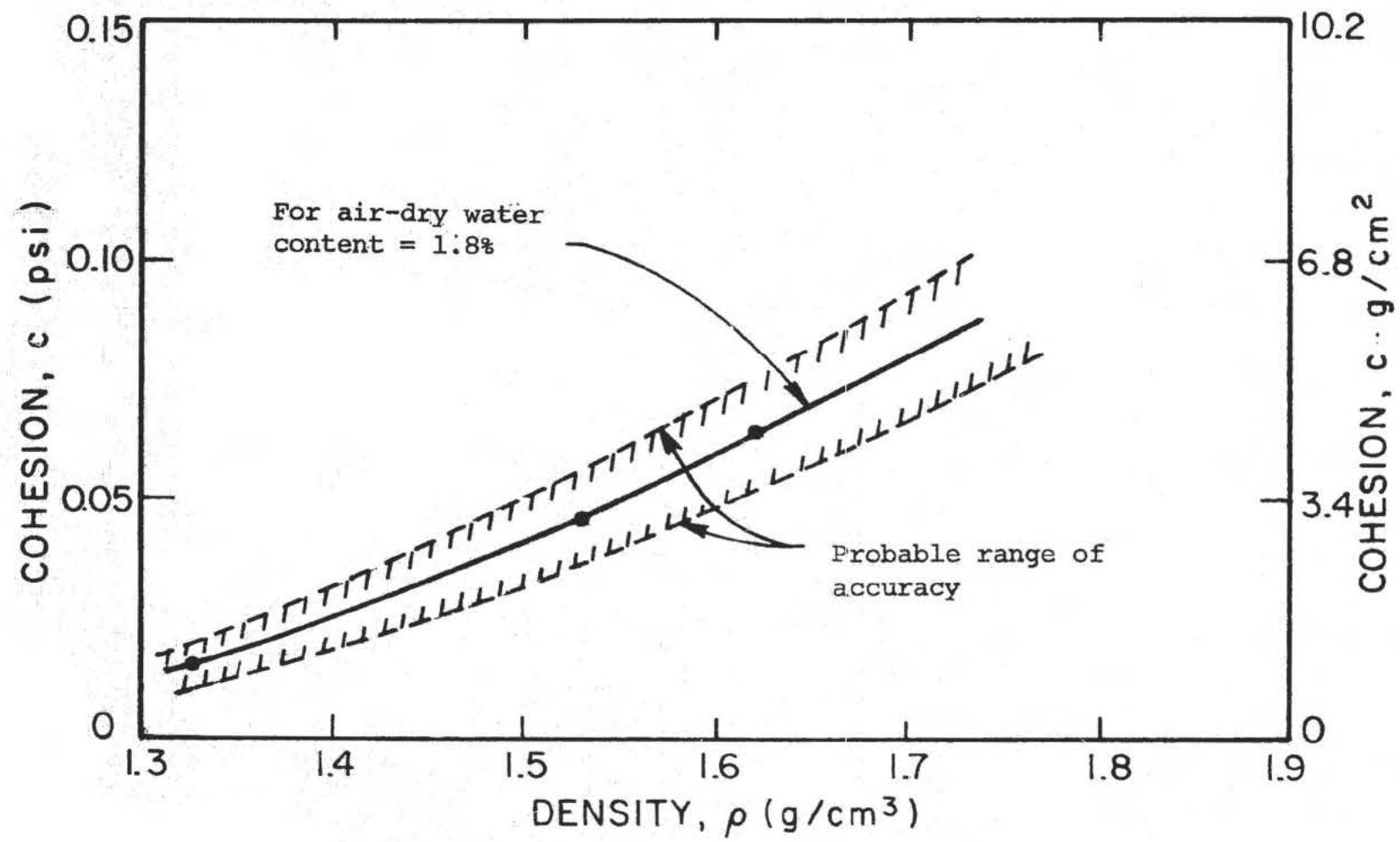


FIGURE 7. Cohesion vs density

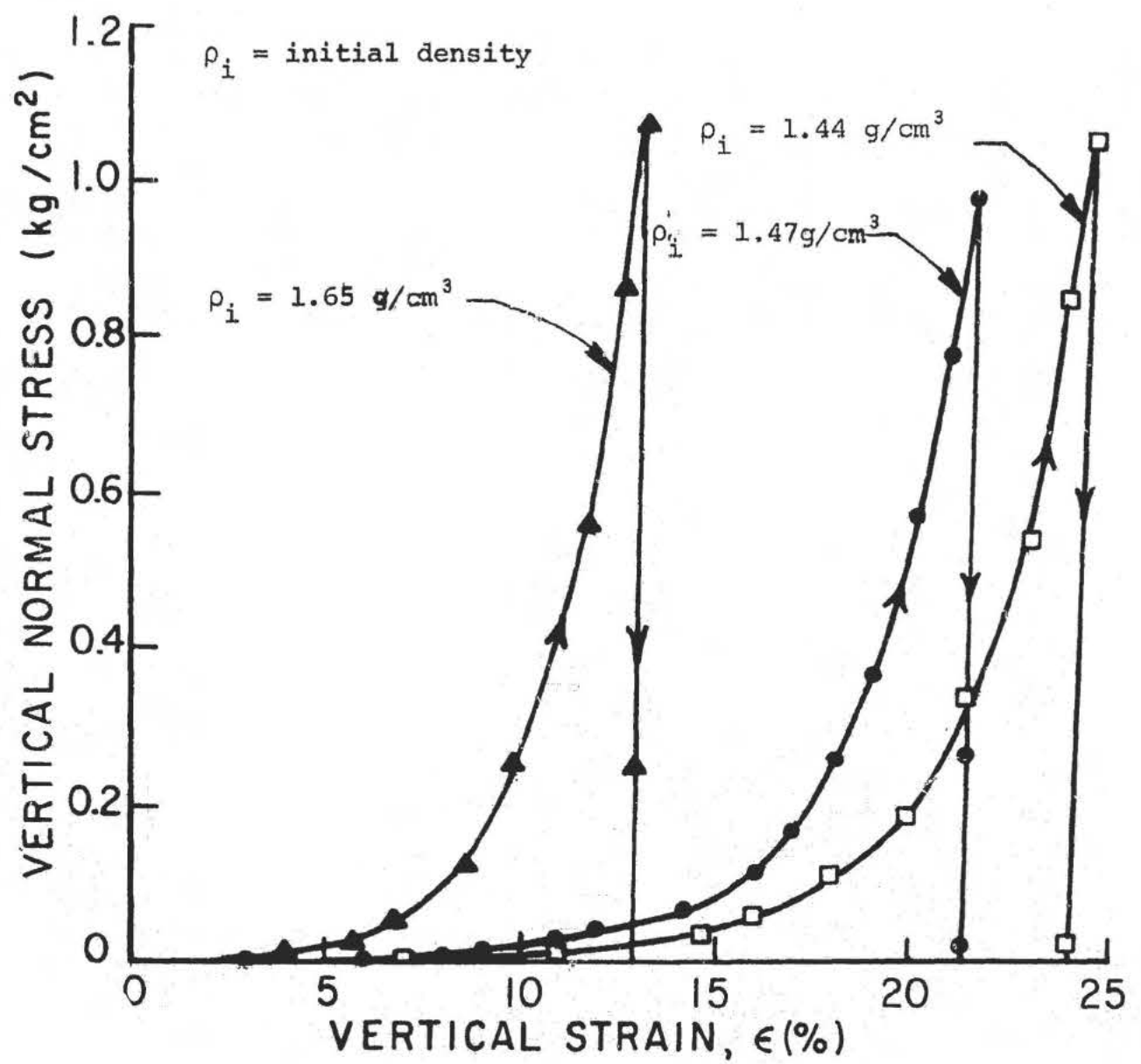


FIGURE 8. Confined compression stress-strain curves for different initial densities

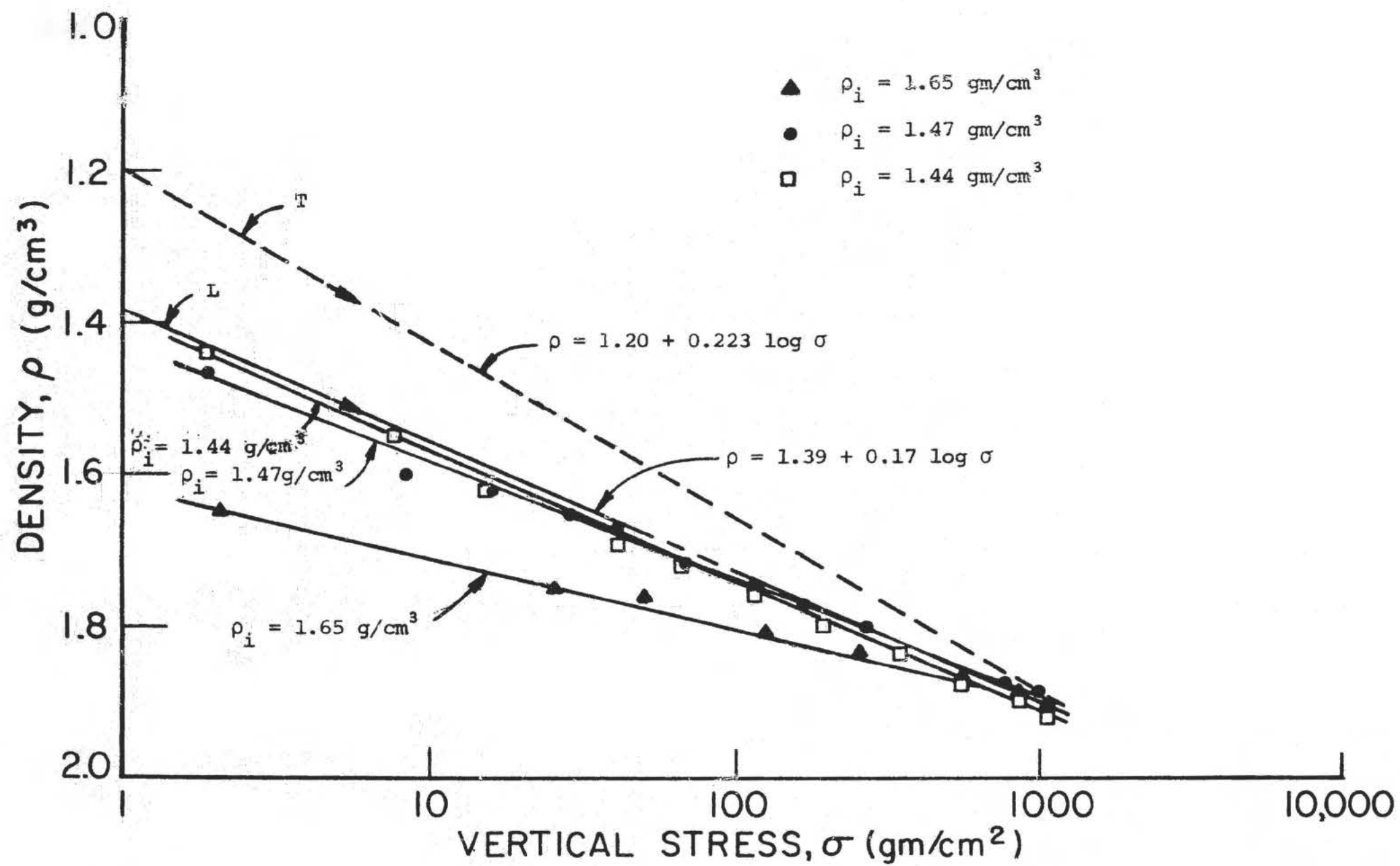


FIGURE 9. Confined compressive stress vs density

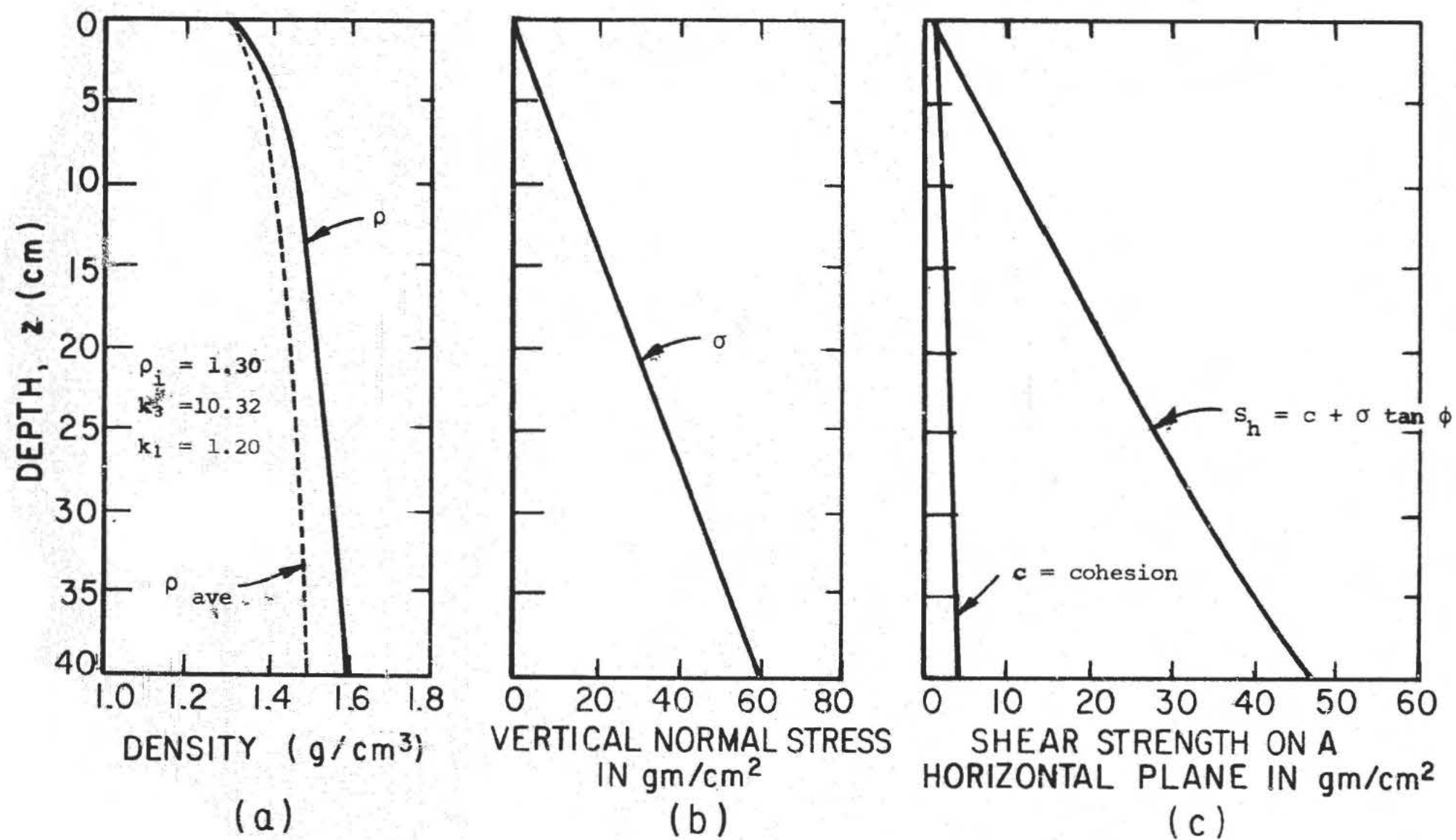


FIGURE 10. Variation of density, vertical stress, and shear strength with depth for simulated lunar soil

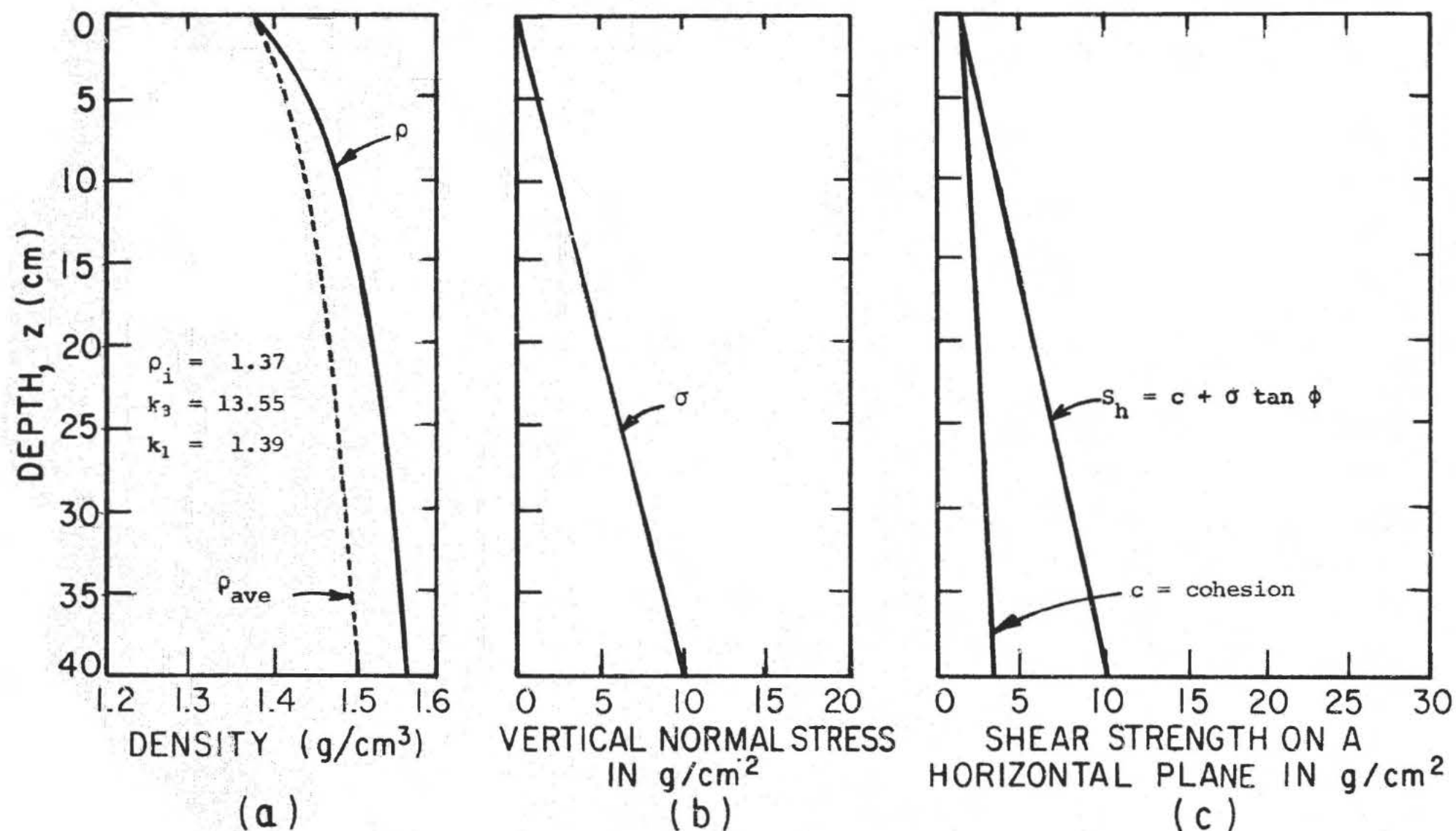


FIGURE 11. Estimated variation of density, vertical stress, and shear strength with depth for actual lunar soil (reduced gravity field)



FIGURE 12. Footprint in simulated lunar soil.

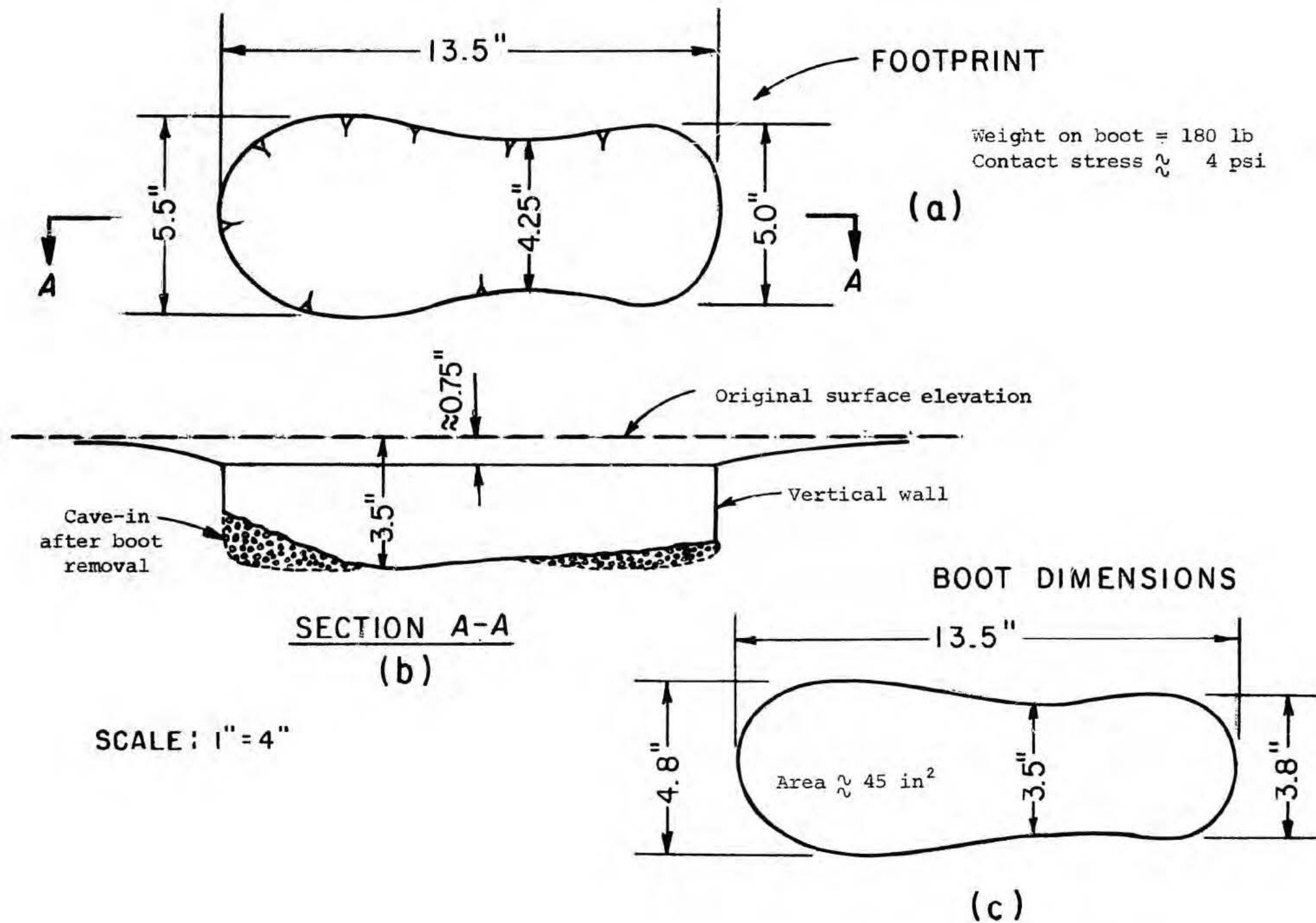


FIGURE 13. Footprint details

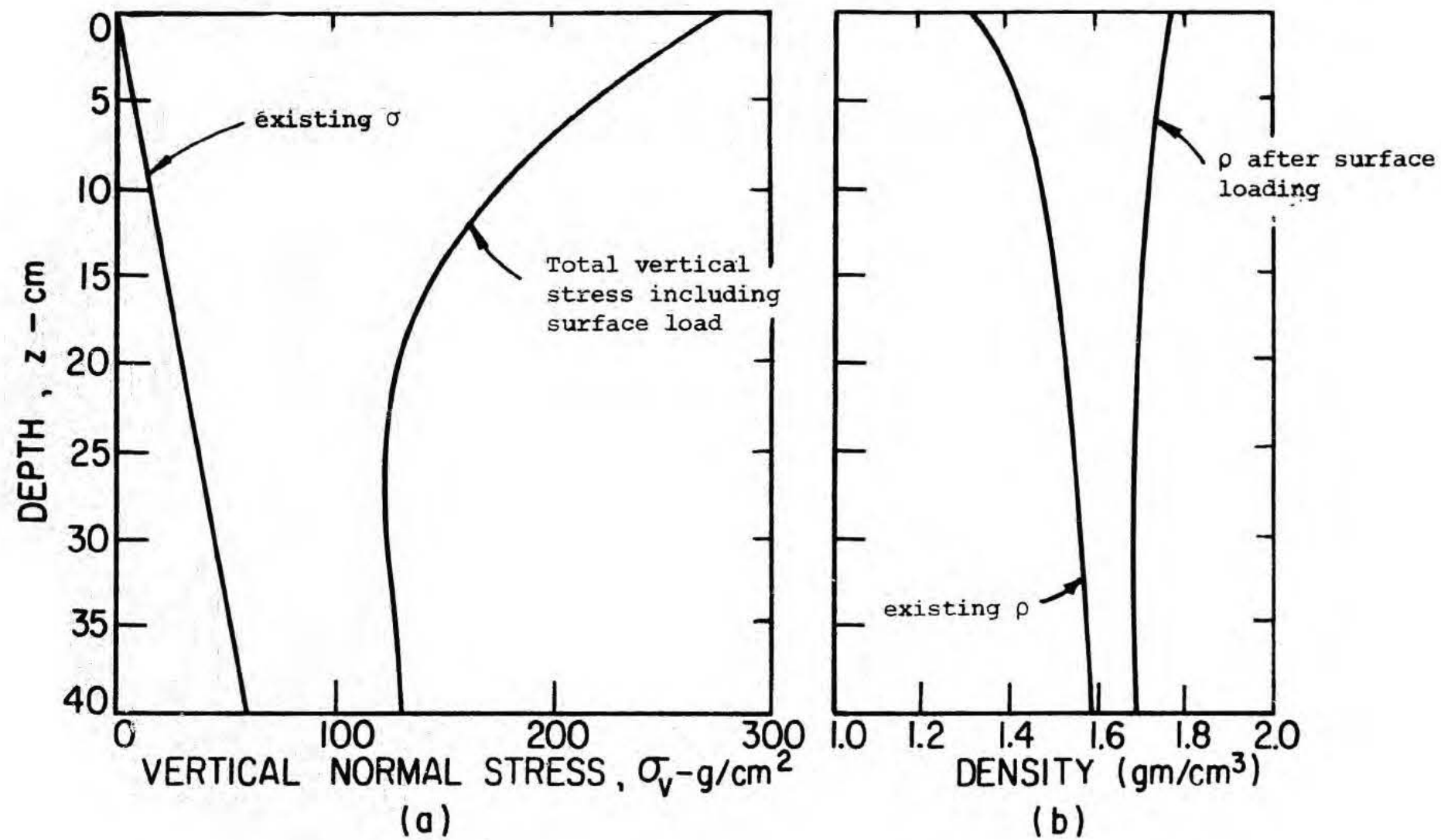


FIGURE 14. Variation of vertical stress and density before and after surface loading for simulated lunar soil

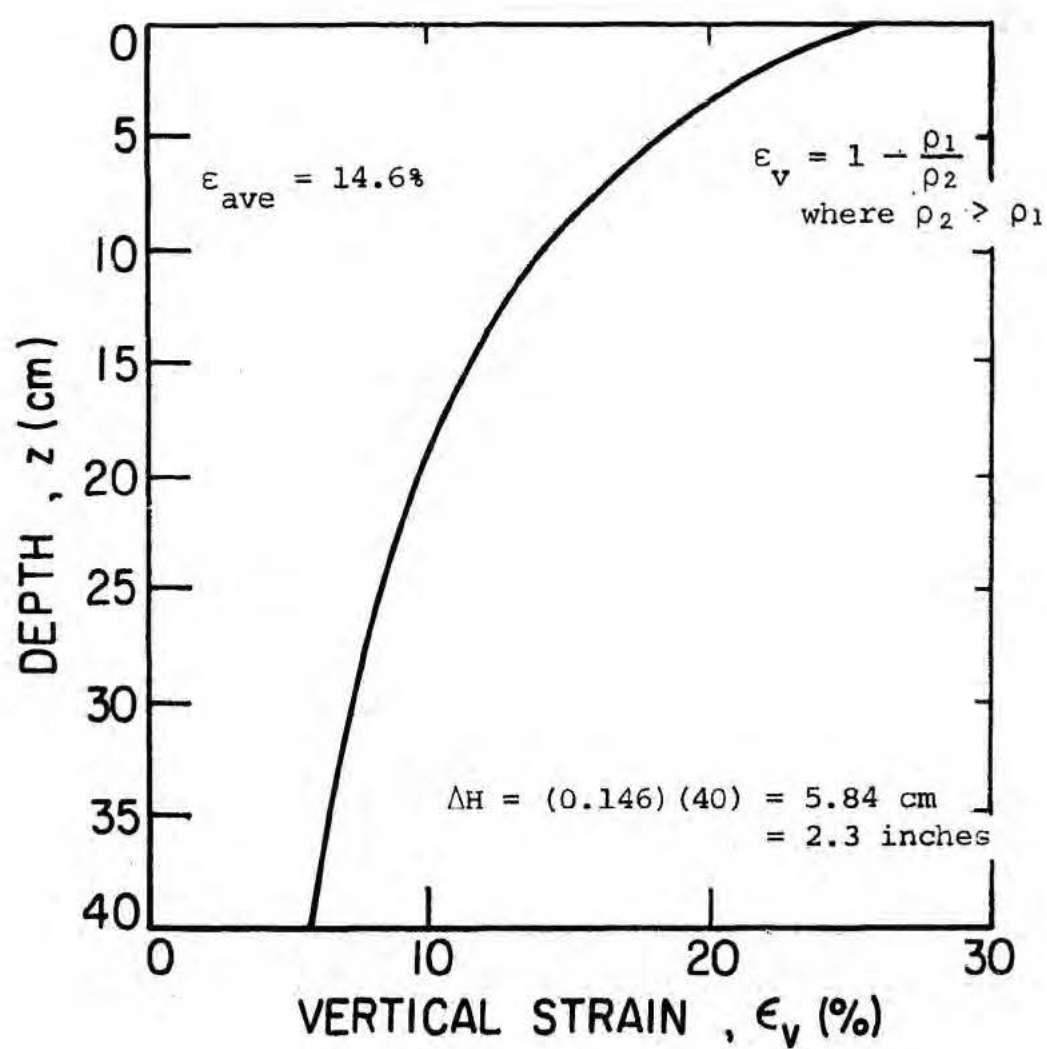


FIGURE 15. Variation of vertical strain with depth for simulated lunar soil

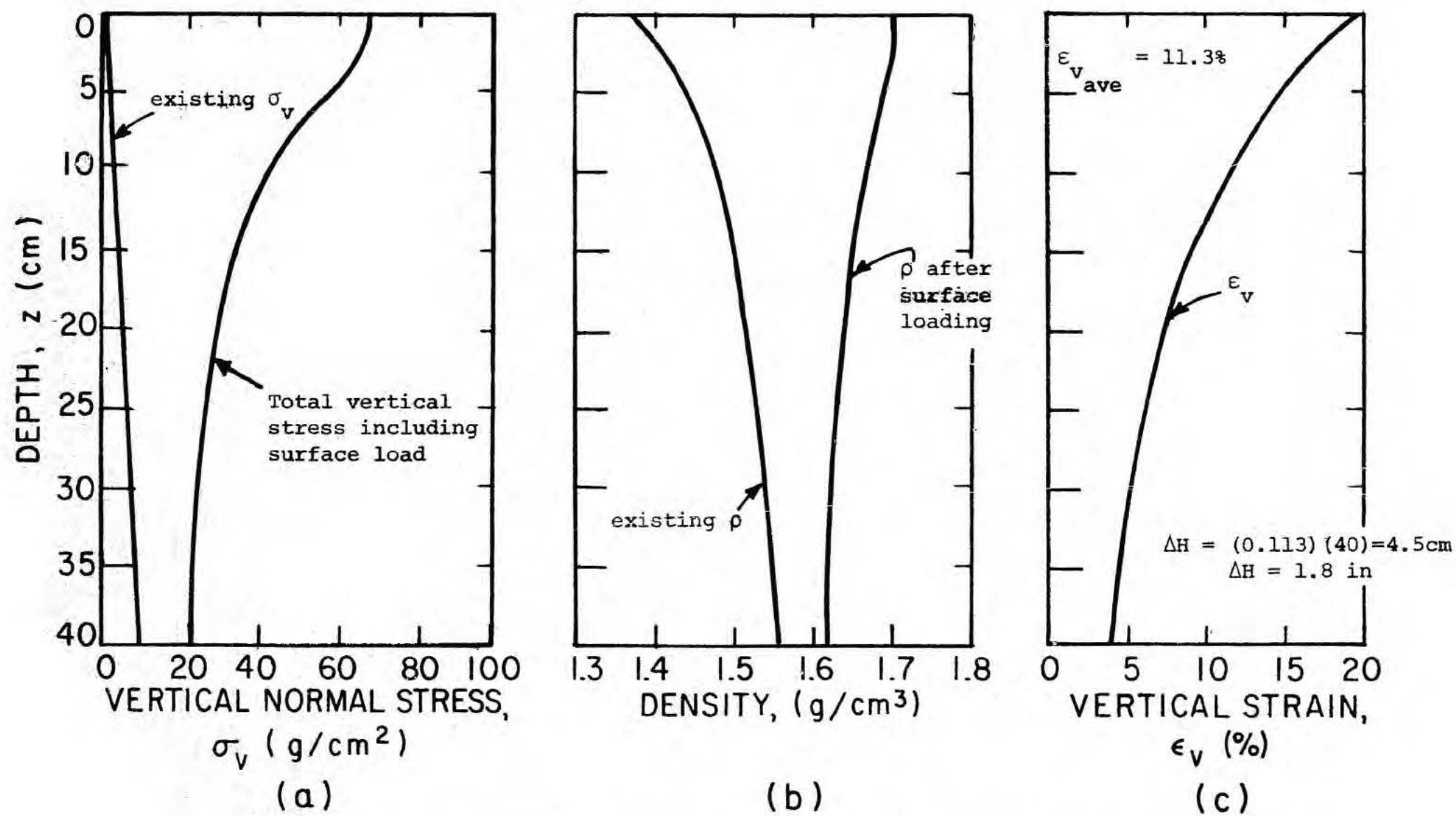


FIGURE 16. Probable variation of vertical stress, density, and vertical strain before and after surface loading for actual lunar soil (reduced gravity field)

II. FRICTION ANGLE OF LUNAR SURFACE SOILS ESTIMATED FROM BOULDER TRACKS

(H. J. Hovland and J. K. Mitchell)

1. INTRODUCTION

Among the conspicuous and interesting features on the surface of the moon observed on lunar orbiter photographs are boulders or blocks of rock and the tracks that some of these boulders left as they rolled down slopes. Some of these boulders have been studied in previous investigations (Moore and Martin, 1967; Filice, 1967; Eggleston et al., 1968).

Early investigations of the relationship between boulder size and track width were aimed primarily at determining the static bearing capacity of lunar surface soil. Currently we are investigating the possibility of deducing strength parameters (cohesion and angle of internal friction). A summary of past work done by our group on the study of lunar boulder tracks was presented in the final report for Contract NSR 05-003-189 (Mitchell et al., 1968). In this report, several methods for utilizing boulder-track data were considered, each giving somewhat different results. It was recommended that the boulder-track phenomena be further studied, and that if variability is to be determined, it is important to use the same method throughout.

Dr. Henry Moore of the U. S. Geological Survey, Menlo Park, California, is also performing similar studies. It is understood that Dr. Moore has investigated boulder-track phenomena for Orbiter II photographs primarily.

His results indicate friction angles in the range of 20 to 25 degrees. In his analysis the bearing capacity required at the point where the boulder rests, utilizing a full circular bearing area corrected for determinable flatness of boulder shape is considered. In our analyses an attempt has been made to relate the boulder to the track at failure and, hence, to determine a limiting friction angle required for stability. Dr. Moore's analysis on the other hand determines a friction angle for partially mobilized resistance. Therefore, his values for ϕ are somewhat lower than those obtained in the analyses to follow. The present report describes the status of current studies.

2. METHOD OF ANALYSIS

(a) General:

From observation of boulder-track combinations from orbiter photographs and terrestrial boulder-track phenomena it appears that boulders can be nearly spherical, quite rectangular with one distinct shorter dimension, or intermediate in shape and still form a relatively smooth track. However, the nearly spherical boulder should leave the smoothest track. Tracks have been observed to be smooth, chain-like or disconnected as shown in last year's final report. These tracks imply either uniform rolling motion or jumping motion with a combination of translation and rotation both when the boulder is or is not in contact with the ground.

(b) A Rolling Sphere - Theory:

A boulder rolling on a slope where the soil fails, in general shear, i.e., the soil behaves essentially as an incompressible material, would leave a track with a raised rim as shown on Fig. 1. For the purpose of

the present analysis, the theory will be developed for a somewhat more idealized situation, as shown on Fig. 2.

From the above illustration, it may be seen that the track depth will be given by

$$z = r(1 - \cos\theta) = r(1 - \cos[\sin^{-1} \frac{\omega}{2r}])$$

The semicircular soil-boulder contact area may be represented by an equivalent rectangular area defined by

$$2b^2 = \frac{\omega^2}{4} \frac{\pi}{2}, \quad b = \frac{\omega}{4} \sqrt{\pi} = 0.444 \omega$$

If $\alpha = 0$, i.e. a horizontal surface, the resultant force causing the sphere to move and form the track must naturally be inclined at some angle with respect to the direction of the weight of the sphere. Assuming that this resultant goes through the centroid of the soil-boulder contact area, the maximum value of this resultant would be approximately $\sqrt{2}$ (weight of boulder) when the ratio of ω/r is maximum or 2. For smaller ratios of ω/r and slope angles greater than zero, the magnitude of the resultant would be more nearly equal to the weight of the sphere. It will, therefore, be assumed in the following analysis that the magnitude of the resultant force equals the weight of the boulder.

(c) Bearing Capacity Theory:

The general bearing capacity equation for a strip footing is (c.f. Leonards, 1962)

$$q = \frac{\gamma b}{2} N_{\gamma} + c N_c + q' N_q$$

For a rectangular footing this equation may be modified to give

$$q = \frac{\gamma b}{2} N_{\gamma} s_{\gamma} + c N_c s_c + q' N_q s_q$$

In these equations

q = unit bearing capacity

γ = soil unit weight

b = breadth of footing

c = soil cohesion

q' = surcharge

s_{γ}, s_c, s_q = shape factors

N_{γ}, N_c, N_q = bearing capacity factors which have values dependent on the soil friction angle, ϕ .

Skempton (1951) indicated that for $\phi = 0$ the value of s_c can be taken as $(1 + 0.2 b/L)$, where L is the length of a rectangular footing. Meyerhof (1951) proposed that for $\phi = 30^\circ$, s_q equals approximately $(1 + 0.2 b/L)$. The shape factor, s_{γ} , is given by $(1 - 0.3 b/L)$ according to Lundgren and Hansen (1955) and Hansen (1957).

Thus the bearing capacity equation becomes

$$q = \frac{\gamma b}{2} (1 - 0.3 b/L) N_{\gamma} + c(1 + 0.2 b/L) N_c + q'(1 + 0.2 b/L) N_q$$

Meyerhof (1951) has presented bearing capacity factors for footings on slopes. Meyerhof's factors used in this study are presented in Figures 3, 4, and 5.

For the sphere considered representative of a rolling boulder, $b/L = 1/2$ and $b = 0.444 w$. If an average surcharge depth is taken as $z/2$, then the bearing capacity equation becomes

$$q = \frac{0.85}{2} (0.444 w) \gamma N_{\gamma} + 1.1 c N_c + \frac{1.1}{2} \gamma z N_q$$

Since lunar gravity is one sixth earth gravity unit weights must be correspondingly reduced. Thus if γ_e represents the unit weight of the lunar soil in the earth's gravitational field, the bearing capacity on the moon will be given by

$$q_m = \frac{0.85(0.444)}{12} w \gamma_e N_{\gamma} + 1.1 c N_c + \frac{1.1}{12} \gamma_e z N_q$$

or

$$q_m = 0.0314 w \gamma_e N_{\gamma} + 1.1 c N_c + 0.0916 z \gamma_e N_q$$

The bearing capacity may be taken as the boulder weight divided by the bearing area. For the geometry assumed herein,

$$q_m = \frac{\text{Boulder weight}}{\text{Bearing area}} = \frac{\frac{4}{3} \pi r^3}{\frac{\pi \omega^2}{2 \cdot 4}} \gamma_b = \frac{32}{3} \frac{r^3}{\omega^2}$$

where

$$\gamma_b = \text{unit weight of boulder (lunar gravity)}$$

d. Analysis

In applying the above theory to lunar boulder tracks it was assumed that the boulders are spherical. To make this assumption valid only boulders appearing equidimensional on the lunar orbiter photographs and having relatively smooth tracks were selected. The most recent estimates, Mitchell et al. (1968) of average lunar soil properties give $\gamma_e \approx 100$ pcf, $c_{ave} \approx 2.08$ psf (value assumed by Dr. H. Moore) and, $\gamma_b = 2.7 \left(\frac{62.4}{6} \right)$ pcf. By measuring the track width and boulder diameter on the photographs, the bearing capacity equation was solved by trial for the friction angle. The results are presented in the following table for 16 boulder tracks revealed by Orbiter V photographs and one boulder track shown in Orbiter II photographs.

For most of the above boulders it was assumed that the boulder came to rest on a slope of $\alpha = 0^\circ$.

It may be seen from these results that while lunar soil friction angles in the range of 25° to 45° are required to account for the results, the majority of the values fall between 32° and 38° . An assumption of a larger value of cohesion, e.g. 20 psf has very little effect on the results obtained, amounting to a reduction in the required friction angle of about 2° .

3. DISCUSSION

It should be noted that the assumptions involved in computing the bearing capacity " q_m " are considerably fewer than are required to deduce ϕ from the bearing capacity equation.

Table 1

Location	Frame	Framelet (boulder location)*	Boulder Diameter m	Track Width m	Slope α (assumed)	q_m psf	ϕ
Hadley Rille	V-105H	233 + 9.0 mm, 232 mm	15.3	10.3	0	4150	31°
	"	233 + 11.0 mm, 234 mm	14.7	8.8	0	5020	33°
	"	234 + 8.0 mm, 235 mm	14.7	8.8	0	5020	33°
Schröter's Valley	V-204H	221 + 18.0 mm, 161 mm	12.8	6.1	0	6920	38°
	"	210 + 15.0 mm, 242 mm	12.8	7.3	0	4820	34°
	"	210 + 14.0 mm, 177 mm	11.2	5.5	0	5700	38°
	"	202 + 7.0 mm, 253 mm	19.5	12.2	0	6120	33°
So. E part of Hyginus	V-95H	957 + 11.5 mm, 164.0 mm	8.4	6.0	0	2020	29°
		959 + 12.5 mm, 161.0 mm	8.4	4.8	0	3160	34°
		962 + 3.0 mm, 167.0 mm	8.8	4.5	0	4100	37°
		965 + 11.0 mm, 239.0 mm	9.1	4.8	0	4030	37°
		968 + 13.0 mm, 253.0 mm	11.0	3.6	0	12600	45°
		970 + 7.0 mm, 246.0 mm	14.4	9.2	0	4300	31°
		978 + 13.0 mm, 252.0 mm	6.0	4.8	0	1150	**25°
Large hill so. of Alexander	V-88H	011 + 8.5 mm, 230 mm	19.5	10.6	0	8100	36°
Sabine D	II-76H	364 +	8.7	6.4	0	1970	28°
	II-76H	364 + (same)	8.7	6.4	13°		32°
No. E part of Hyginus	V-96H	092 + 1.0 mm, 46.0 mm	15.9	10.6	10°	4380	32°

*Framelet number, distance from framelet edge, distance from data edge

** $\beta = +10^\circ$ was used on the Meyerhof's charts.

Values of the internal friction angle and cohesion are of importance in advancing our understanding of lunar soils. That the results in the above table give reasonably consistent and uniform values of ϕ within different areas should imply first, that by analyzing a sufficient number of boulder-track phenomena an approximate average value of ϕ can be obtained within limits of the theory used and, second, that lunar soils may be uniform with respect to ϕ and c and do not vary greatly from place to place. It is also to be noted that the results imply that lunar soils appear to behave primarily as cohesionless materials, since cohesion of a magnitude consistent with Surveyor results gives an insignificant contribution in the bearing capacity equation.

4. CONCLUSIONS

Several assumptions were made in the application of the bearing capacity equation to the boulder problem. Boulder track formation is a dynamic problem. Since general bearing capacity theory is based on statics, it cannot be expected to hold rigorously for dynamic conditions. Consequently further theoretical and experimental studies are being initiated by us to enable better analysis of the boulder-track features so common on the lunar surface. The following studies are proposed:

1. Analysis of additional boulder-track phenomena using the method described above and refined as suggested below, so that statistically valid average values of ϕ and c can be established within limits of the theory used.
2. Refinement of the present approach by correcting for boulder shape, slope, and observable and measurable features. This is to a certain extent already possible; for example, it may not

be necessary to assume that a boulder is equidimensional, instead boulder dimensions can be checked using plan measurements and shadow data.

3. Development of additional approaches or equations so that an independent solution for cohesion is possible.
4. Observation of terrestrial boulder tracks to aid in development of a feel for the variables and the limitations inherent in this type of study.
5. Development of a theory which describes the dynamic rolling boulder problem, and verification of this theory by experimental investigations.

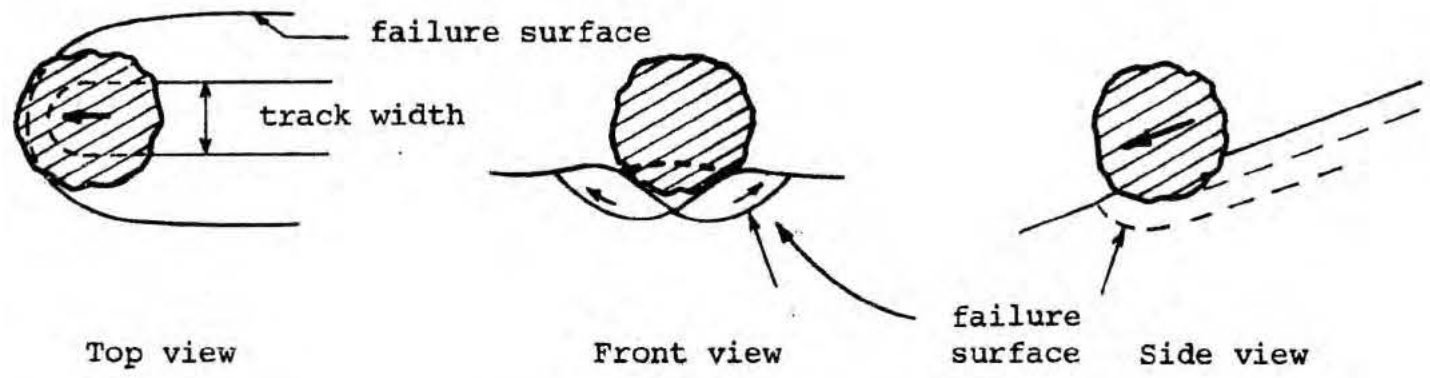


FIGURE 1

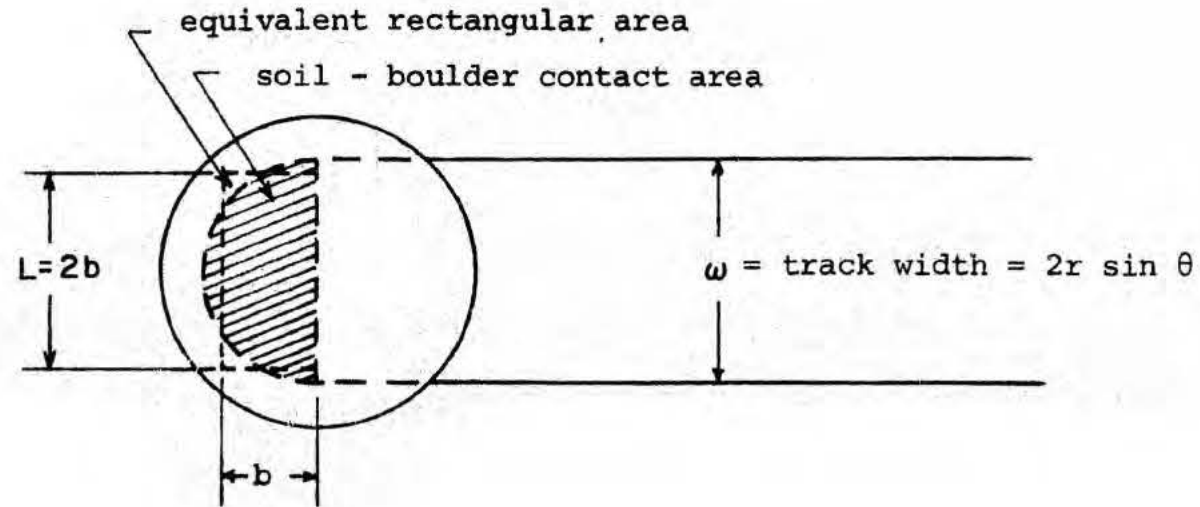
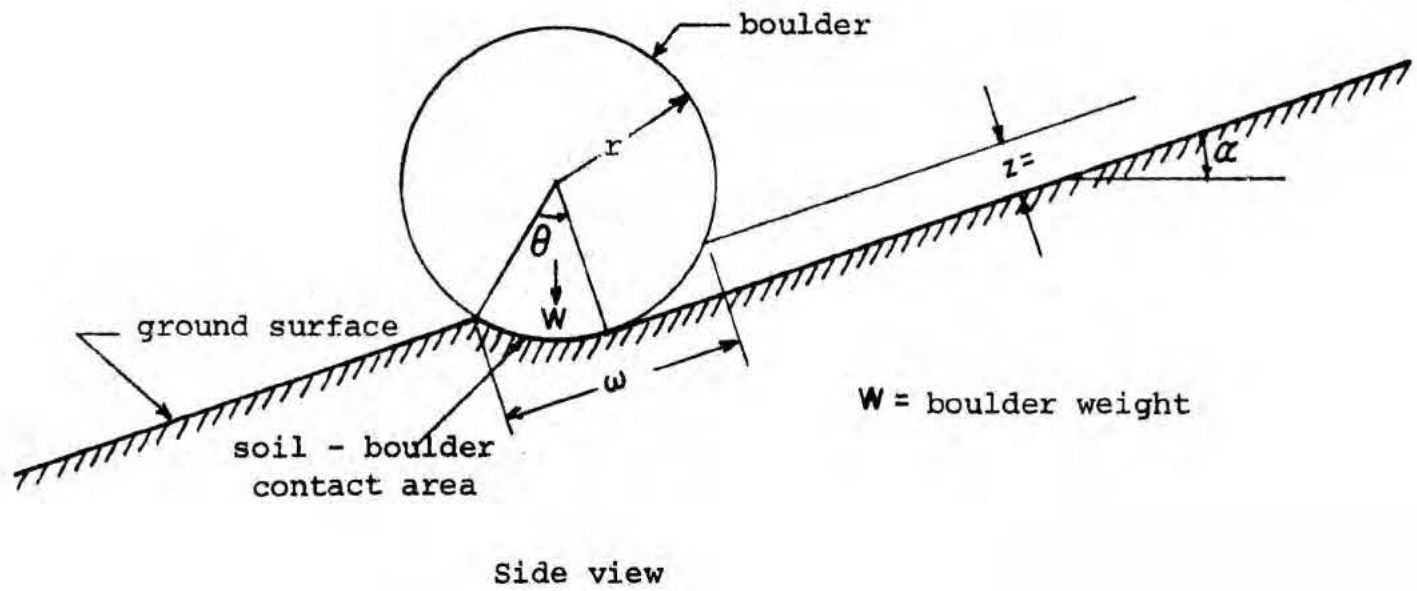


FIGURE 2

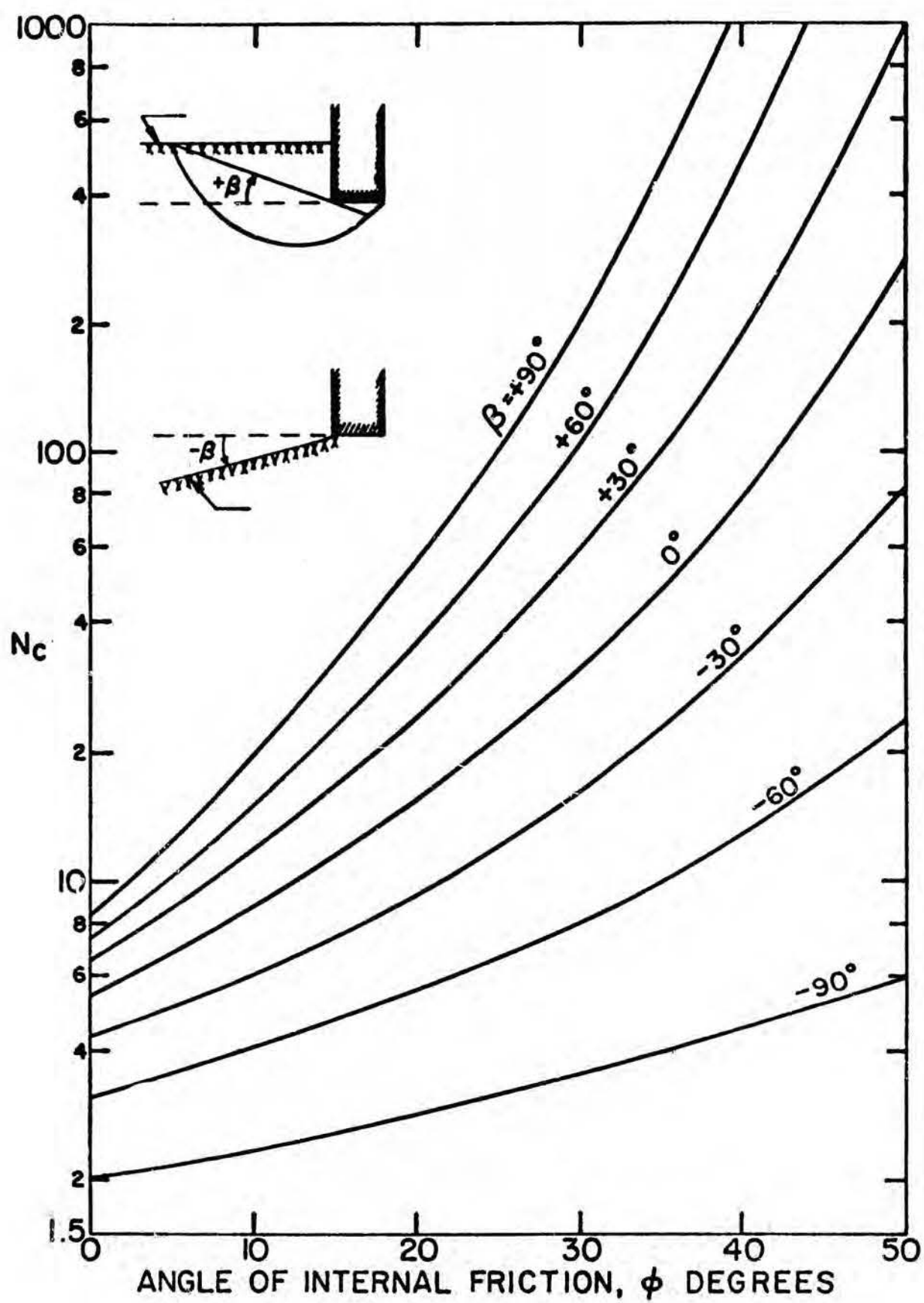


FIGURE 3. General Bearing Capacity Factor N_c for Strip Foundation (after Meyerhoff, 1951).

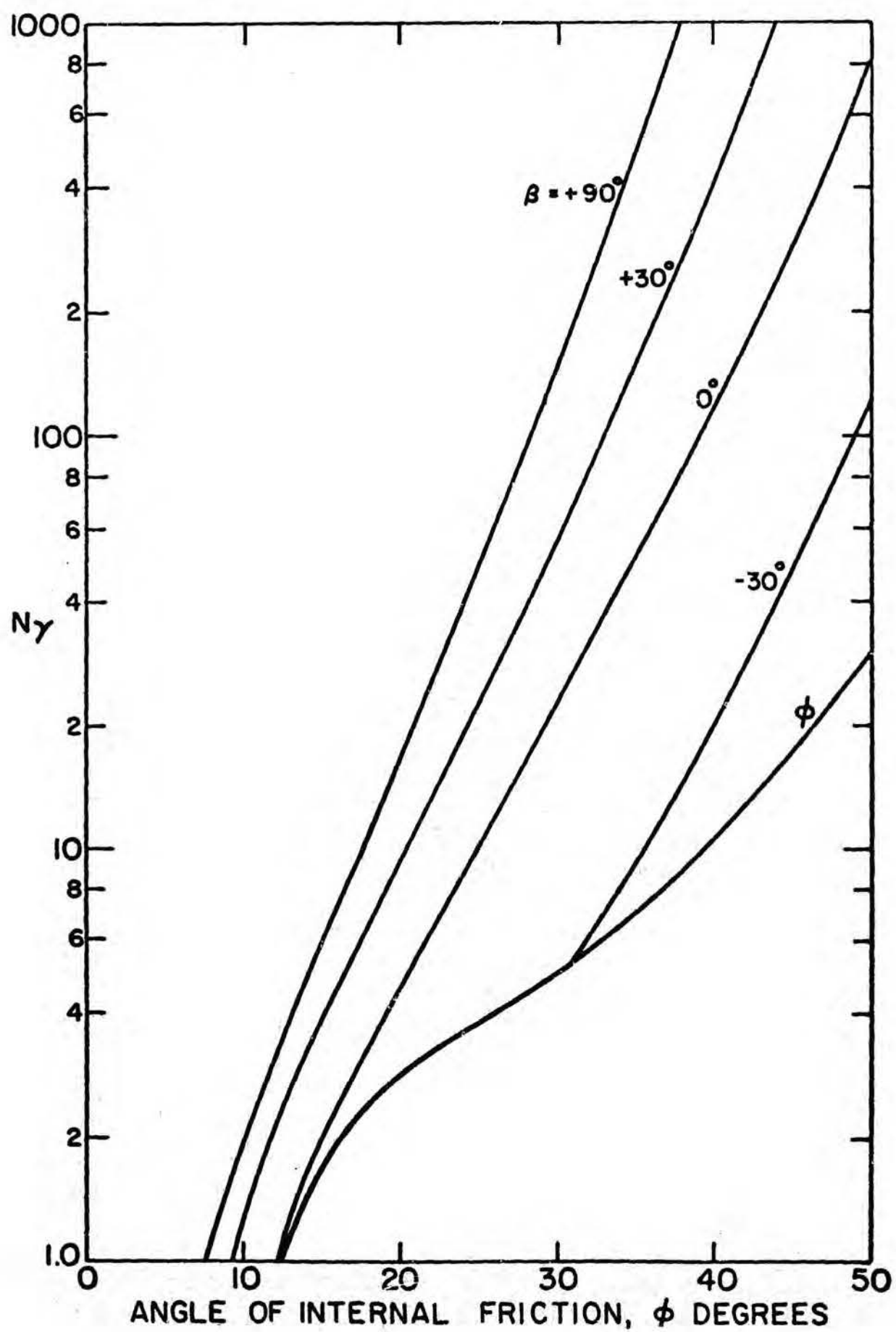


FIGURE 4. General Bearing Capacity Factor N_γ for Strip Foundation (after Meyerhoff, 1951).

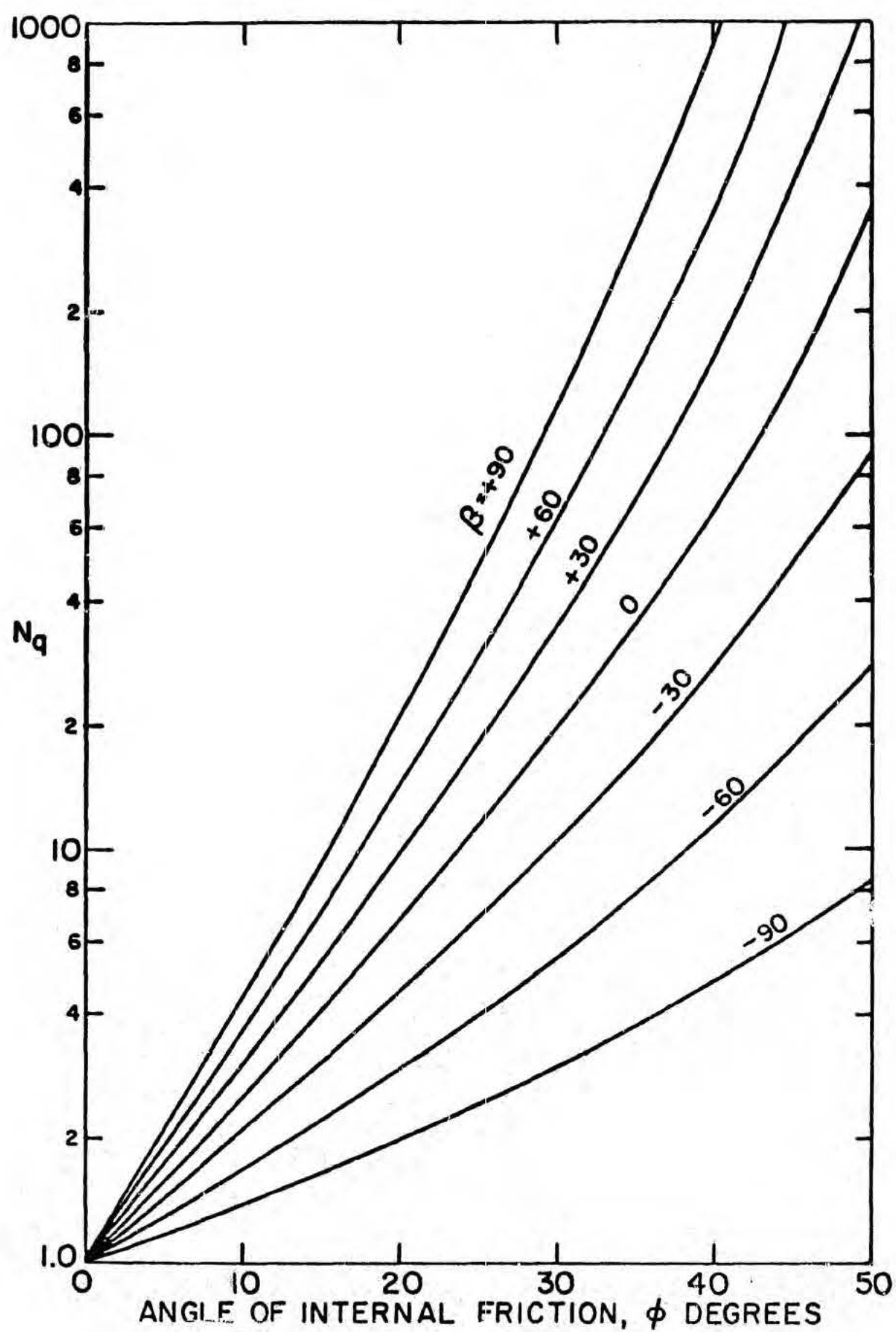


FIGURE 5. General Bearing Capacity Factor N_q for Strip Foundation (after Meyerhoff, 1951).

REFERENCES

1. Eggleston, J. M., Patteson, A. W., Throop, J. E., Arant, W. H. and Spooner, D. L., "Lunar Rolling Stones," Photographic Engineering, Vol. 34, No. 3, March 1968.
2. Filice, A. L., "Lunar Surface Strength Estimates from Orbiter II Photographs," Science, Vol. 156, p. 1486, 1967.
3. Hansen, J. B., "Foundations of Structures - (a) General Subjects and Foundations other than Piled Foundations," Proc. of the Fourth Int. Conf. on Soil Mech. & Found. Eng., London, 1957.
4. J.P.L., Cal. Inst. of Tech., "Lunar Traverse Seminar," Document 760-27, July 1968.
5. Leonards, G. A., "Foundation Engineering," McGraw-Hill Book Co., Inc., 1962.
6. Lundgren, H. and Hansen, J. B., "Geoteknik," Teknisk Forlag, Kobenhavn. 1958.
7. Meyerhof, G. G., "The Ultimate Bearing Capacity of Foundations," Geotechnique, Vol. II, 1951, p. 301.
8. Mitchell, J. K. et al, "Material Studies Related to Lunar Surface Exploration," Final Report, Contract NSR 05-003-189, University of California, Berkeley, July 1968.
9. Moore, H. and Martin, G., "Lunar Boulder Tracks," Orbiter Supporting Data No. 1, 1967.
10. Skempton, A. W. (1951): The Bearing Capacity of Clays, Proc. Bldg. Res. Congr., London 1951.

SYMBOLS

b	width of equivalent rectangle
c	apparent cohesion
D	diameter of boulder
H	high resolution
L	length of equivalent rectangle
N_c, N_γ, N_q	bearing capacity factors
q	unit bearing capacity
q'	surcharge
q_e	unit bearing capacity in earth gravity
q_m	unit bearing capacity in lunar gravity
r	radius of boulder
s_c, s_γ, s_q	shape factors in the bearing capacity equation
W	boulder weight
z	sinkage or track depth
α	slope angle
β	angle defining equivalent free surface on Meyerhof's charts
γ	unit weight
γ_b	boulder unit weight in lunar gravity
γ_e	unit weight of soil in earth gravity
ϕ	apparent angle of internal friction
θ	angle defining soil-boulder contact
ω	track width
II	orbiter two
V	orbiter five

III. TRAFFICABILITY OF THE LUNAR SURFACE

(J. B. Thompson and J. K. Mitchell)

1. INTRODUCTION

The current state-of-the-art of vehicle mobility and trafficability prediction as related to the design and operation of lunar roving vehicles was reviewed and evaluated under contract NSR 05-003-189. It was noted that there is at present no method that is completely suitable for the reliable prediction of needed trafficability and vehicle-soil interaction parameters. Recommendations were made that intensive studies of both an experimental and theoretical nature be initiated in order to develop the information necessary for design and performance prediction of lunar roving vehicles.

On October 8 and 9 a Working Group meeting was held at NASA Headquarters for the purpose of establishing design criteria for a dual mode lunar roving vehicle. The lack of a proven method for trafficability analysis, even when reasonably close estimates of soil properties are available, was readily apparent at this meeting. A subsequent meeting was held on November 15, 1968 at the Jet Propulsion Laboratory to consider further the problem of soil vehicle interaction. As a result of these meetings it is understood that a proposal for experimental model studies has been prepared by the Waterways Experiment Station for the purposes of establishing the performance parameters of wheels of a type proposed for lunar vehicles and answering basic performance questions such as the maximum slope that may be negotiated on the lunar surface. The results of experimental studies of this type may be useful also for the establishment of similitude relationships for lunar

trafficability analysis once cone index values for lunar soils are available. The essential elements of this method are described in the Final Report for Contract NSR 05-003-189.

Our group has concerned itself during the past quarter with some analytical aspects of lunar soil trafficability. As a result of the discussions at the Working Group Meeting for the Dual Mode Lunar Roving Vehicle we became concerned with the question "How much difference is a variation in soil conditions likely to make on the performance parameters of a lunar roving vehicle?" In order to gain insight into this question a series of analyses have been made using the Bekker "Soil Value System" method of analysis. That there are many limitations and inconsistencies in this method is well recognized. Nonetheless it is about the only quasi-theoretical method available, and furthermore a considerable body of previous trafficability work for lunar exploration purposes has been done using this method. Consequently, it is believed that the results of the analyses reported below help to define those soil and wheel characteristics that will be of greatest concern in further studies of lunar soil trafficability.

2. BASIC RELATIONSHIPS

The key relationships that are developed in the "Soil Value System" are for wheel or track thrust, motion resistance, and drawbar pull (Bekker, 1960). The merits and limitations of the theory underlying these relationships and the test methods used for the determination of needed soil parameters have been discussed at length in the literature

and are summarized in Chapter I of Vol. III of the Final Report for Contract NSR 05-003-189.

The appropriate relationships are as follows:

Wheel or Track Thrust -

$$H = (\ell bc + W \tan \phi) \left(1 - \frac{K}{i_0 \ell} \left(1 - e^{-i_0 \ell / K} \right) \right) \quad (1)$$

The above equation is applicable for a soil exhibiting a stress-deflection curve in which stress continuously increases with deflection. For a soil which exhibits a stress strain curve in which stress falls off after a certain deflection is reached, another expression in terms of two parameters K_1 and K_2 can be written for thrust. Because little information is available on the stress-strain properties of the lunar soil, it will be assumed that the soil is of the first type. If the results of the Bevameter annular shear test are plotted as the ratio of the recorded shear stress to the soil shear strength versus the deflection, K is equal to the inverse of the slope of the curve at zero deflection. In other words the magnitude of the stress strain parameter indicates the steepness of the stress-strain curve.

Motion Resistance

Rigid Wheel -

$$R = \left(b \left(\frac{k_c}{b} + k_\phi \right) \right)^{\frac{-1}{2n+1}} \frac{1}{n+1} \left(\frac{3W}{3-n} \right)^{\frac{2n+2}{2n+1}} D^{\frac{-n-1}{2n+1}} \quad (2)$$

Track -

$$R = \left[b \left(\frac{k_c}{b} + k_\phi \right) \right]^{\frac{1}{n}} \frac{1}{n+1} \left(\frac{W}{\ell} \right)^{\frac{n+1}{n}} \quad (3)$$

Drawbar Pull -

$$DP = H - R$$

where:

- ℓ - wheel or track contact length
- b - wheel or track contact width
- D - wheel diameter
- W - wheel or track load
- i_0 - slip of wheel or track
- K - soil stress-strain parameter
- c, ϕ - soil strength constants
- n, k_c, k_ϕ - soil sinkage parameters

3. PARAMETER STUDY

The wheel dimensions and load-deflection characteristics adopted for this study were taken from the results of a metal wheel test program conducted by AC Electronics (1967). The wheels used in this test program were 40 inches in diameter and 10 inches in width across the contact surface. Because the contact length was not measured during testing, it was estimated from the load-deflection characteristics of the wheels. For the purpose of this study the following wheel loads and corresponding contact lengths were used:

W (lbf.)	ℓ (in.)
50	14.7
75	16.5
100	18.2
150	20.6

From a consideration of the deflection characteristics of the wheels studied it might be anticipated that the motion resistance characteristics would fall between those of a track and a rigid wheel. Therefore, equations 2 and 3 should theoretically envelope the measured motion resistance values. This hypothesis is examined subsequently.

Values assumed for soil cohesion (c) and angle of internal friction (ϕ) were as follows, based on available data from the Surveyor program.

$$c = 0.05 \text{ to } 0.15 \text{ psi}$$

$$\phi = 37^\circ \pm 4$$

The soil sinkage parameters k_c , k_ϕ , and n are less certain. Scott (1968)* reported values for n of 1.0 and 0.7 determined from load-sinkage tests using the Surveyor Surface Sampler with the scoop closed and open respectively. For the purpose of this study, k_c and k_ϕ were combined into a single parameter, $k = \frac{k_c}{b} + k_\phi$, and the following ranges of values for k and n were assumed for this study:

*Verbal communication as stated at the Lunar Soil Wheel Interaction Meeting at the Jet Propulsion Laboratory, November 15, 1968.

$$k = \frac{k_c}{b} + k_\phi = 0.5 \text{ to } 6.0$$

$$n = 0.75 \text{ to } 1.25$$

Estimates of the soil stress-strain parameter K can be based only on terrestrial experience as appropriate tests have as yet not been conducted on the lunar surface. The range assumed was:

$$K = 0.5 \text{ to } 1.5$$

Using the values stated above for the various wheel and soil parameters, the performance indicators wheel thrust, motion resistance (for both rigid wheel and track), and drawbar pull (for both rigid wheel and track) were calculated. The results are presented in Figures 1 through 5. The sensitivity of each of these performance indicators to each of the assumed soil parameters is discussed below.

A. Influence of K , Soil Stress-Strain Parameter - K affects the calculated thrust as shown in Figure 1, and consequently drawbar pull as indicated in Figures 4 and 5. The influence is greatest for low values of K and for high wheel loads. For example, at a slip of 10 percent and a wheel load of 150 pounds, the variation in the calculated thrust over the range of K assumed in this study is 38.5 pounds. For any given wheel load, the influence of K decreases appreciably with increasing slip.

B. Influence of Soil Sinkage Parameters - The assumed values of the soil sinkage constants affect the calculated motion resistance (Figures 2 and 3) and consequently drawbar pull (Figures 4 and 5). The effect of each is discussed separately below.

- i) n - Within the range of k generally considered applicable to lunar soil (i.e., 2.5 or greater), the effect of the assumed value of n on the calculated motion resistance is seen to be small in the range of wheel loads studied. This is true whether the metal wheel is assumed to behave as a rigid wheel or track. The variation in the calculated motion resistance with n increases with increasing wheel load and k value and is largest in the case of the rigid wheel assumption. For a wheel load of 150 pounds and a value of k of 6, the variation in the calculated motion resistance of a rigid wheel is only 2.2 pounds for the range of n values studied. Therefore, wheel performance does not appear to be sensitive to variation in values of n .

An interesting observation from Figures 2 and 3 is that contrary to the usual way of thinking, larger values of n result in larger values of motion resistance in the applicable range of k values. Therefore, a consistently conservative design should recognize this fact.

- ii) k or $\frac{k}{b} + k_{\phi}$ - The effect of k on the motion resistance increases with a decrease in the value of the parameter and an increase in the wheel load and is greatest for the rigid wheel assumption. For a wheel load of 150 pounds, the difference between the motion resistance of the rigid wheel at values for k of 2 and 6 is 7.7 pounds. The effect of k on the motion resistance of a track is negligible within the applicable range of the parameter, and a value of $k = 4$ was used in calculating the drawbar pull of a track.

C. Influence of Soil Strength Constants - In order to clearly present the effect of the other parameters in Figures 1 through 5, the wheel performance indicators were calculated with the assumed soil strength values of $c = 0.1$ psi and $\phi = 35$ degrees. These two parameters affect the calculated wheel thrust and consequently drawbar pull. The influence of the assumed values of c and ϕ can be seen most easily by examining the thrust equation, Equation 1. For given values of k , l , and i_0 the term in brackets has a fixed value which is multiplied by another term, in parentheses, whose value is determined by values of l , b , c , W , and ϕ . Therefore, for a given wheel load, and consequently contact length, and for the wheel width specified above, it is possible to express in percent the effect of deviations in values of c and ϕ , from 0.1 psi and 35 degrees respectively, on the calculated value of thrust.

The percent change in the calculated value of thrust as a function of the assumed values of c and ϕ is shown in Figure 6. Over the range of c and ϕ values of probable significance, that is $0.05 \text{ psi} < c < 0.15 \text{ psi}$ and $33^\circ < \phi < 41^\circ$, and over the range of wheel loads studied, the maximum variations in the calculated thrust are theoretically 30 and 26 percent due to deviations in c and ϕ respectively. Therefore, the assumed soil strength parameters may be expected to have a significant effect on the vehicle performance. It is noteworthy that the effect of the wheel load on the percent change in the calculated value of thrust is the result of the load-deflection characteristics of the wheel. If the wheel load-contact length relationship for the wheel were linear, the percent change would be independent of the wheel load.

Figure 6 can be used to adjust values of thrust for one assumed set of strength parameters to another. For example if a given wheel at a given wheel load is to be tested on several different soils one would only need to calculate the performance indicators based on one set of soil strength parameters and then 1) enter Figure 6 (a) and (b) at the revised parameter values and read the percent change, 2) add the two values together, 3) multiply the thrust calculated for the original set of strength parameter values by the quantity one plus or minus the net percent change divided by one hundred, and 4) plot the adjusted thrust and drawbar pull curves. This approach assumes, of course, that for each wheel load, there is a corresponding contact length independent of the test soil.

The effects of the wheel load, wheel diameter, contact length, and contact width on the wheel drawbar pull have not been presented in the preceding graphs. However, study of Equations (1), (2), and (3) shows that the wheel diameter, contact length, and contact width should be maximized to maximize drawbar pull. With the exception of the motion resistance of the track, in the applicable range of k , the wheel load has a significant effect on the performance indicators (Figures 1 through 5). An increase in wheel load results in an increase in the calculated thrust, motion resistance, and drawbar pull.

An important problem in lunar trafficability investigations is likely to be the mobility of a rover on slopes. Bekker (1960) stated that the maximum slope a vehicle can climb is given by the drawbar pull to weight ratio. Although this conclusion does not consider such important factors as the general stability of the soil mass, it will be used here as a first order measure of the slope climbing capability

of a vehicle. Calculated drawbar pull to weight ratios are shown in Figures 7 and 8. These plots indicate that in spite of the fact that the heavier wheel loads result in larger values of drawbar pull, the increase in wheel load is not matched by an increase in hypothetical slope climbing ability. It appears therefore that for values of slip greater than approximately 10 percent, the axle load should be minimized in order to maximize the slope climbing ability of a vehicle.

4. COMPARISON OF THEORY WITH EXISTING TEST RESULTS

The conclusions reached in this parameter study are obviously only significant if the "Soil Value System" method adequately evaluates the mobility of any proposed lunar vehicle. Very limited metal wheel test results that may be used for an evaluation of the accuracy of the method were reported by AC Electronics (1967).

Mobility tests on both wire mesh and metal elastic wheels were conducted. Because the performance of both wheel types was nearly identical, average values of the measured performance indicators are used in this discussion.

The soil used in this wheel test program was a dry sand with the following parameter values.

$$c = 0.035 \text{ psi}$$

$$\phi = 31^\circ$$

$$\left. \begin{array}{l} k_c = 0 \\ k_\phi = 6 \end{array} \right\} k = 6$$

$$n = 1$$

$$K = (\text{not measured})$$

Tests were performed using wheel loads of 50, 75, 100 and 150 pounds force. The test wheel dimensions and load-deflection characteristics were the same as those used in performing the parameter study in the previous section. Therefore, the various values of the performance indicators calculated for the parameter study can be compared directly with the measured values except that the calculated thrust and drawbar pull values must be corrected to the values of c and ϕ exhibited by the soil used in this test program. From Figure 6, the following percent corrections of the calculated thrust are required for each wheel load.

Table II

W (lbf.)	Percent Change in Thrust
50	-29.2
75	-27.0
100	-24.1
150	-22.6

Plots of the predicted and measured wheel thrust, motion resistance, and drawbar pull are shown in Figures 9 through 11.

A. Thrust - Unfortunately, the soil stress-strain parameter, K , was apparently not measured in this test program. Therefore a value of K of 0.5 was assumed since it resulted in the best fit between the predicted and measured values of thrust as shown in Figure 9. For the wheel loads of 50 and 75 pounds force, the predicted and measured values of thrust are quite close. However for the wheel loads of 100

and 150 pounds force the predicted values of thrust are increasingly larger than the measured values. The explanation for this difference offered by AC Electronics was that slip between the wheel and the soil occurred and therefore the optimum soil strength was not mobilized. Although this explanation seems plausible, a possible inadequacy of the "Soil Value System" method should not be overlooked. However, it is encouraging that the general shape of the predicted and measured thrust plots correspond quite well.

The apparent slip between the wheel and the soil noticed in this test program points out an important problem in terrestrial wheel testing. Since terrestrial wheel-soil friction and adhesion may differ from those on the moon, lunar conditions may have to be artificially duplicated in order to accurately model the wheel-soil interaction.

B. Motion Resistance - The measured, predicted, and corrected predicted values of motion resistance are plotted in Figure 10. Because the "Soil Value System" method provides only for the calculation of the motion resistance due to the force exerted on the wheel by the soil, a correction must be made for the inherent resistance of a given wheel to motion. One way of approaching this problem is to measure the motion resistance of the wheel on a hard flat surface at specified wheel loads. Values of the inherent wheel motion resistance were measured by AC Electronics using this method, and the appropriate corrections have been applied to the predicted values of motion resistance.

As predicted in Section 3 the rigid wheel and track motion resistance assumptions do envelope the measured values of motion resistance. The measured values of motion resistance are small and the

test wheels appear to behave more like a track than a rigid wheel. This is of course what one would expect considering that 1) the reported sinkage was on the order of 1 in., and 2) the contact length, ℓ , was on the order of 15 to 20 in.

C. Drawbar Pull - The predicted and measured values of drawbar pull are plotted in Figure 11. The predicted and measured values of drawbar pull correspond quite well for the wheel loads of 50 and 75 pounds force but for the wheels loads of 100 and 150 pounds force the predicted values are increasingly greater than the measured values.

5. CONCLUSIONS

The following conclusions may be derived from the study of the "Soil Value System" method parameters. Of course the validity of these conclusions is entirely dependent on the validity of the Equations (1), (2), and (3).

- 1) The effect of variations of the soil stress-strain parameter, K , on the calculated value of thrust is greatest at low values of slip and increases with increase in wheel load. Because efficient use of available energy will require the operation of the lunar rover at low values of slip, an accurate estimate of this parameter may be required for adequate prediction of vehicle performance.
- 2) The effect of variations of the soil sinkage constant, n , on the calculated motion resistance is relatively small in the applicable range of values of k . Therefore, an accurate

estimate of this parameter will not be required to adequately predict vehicle performance. However, a consistently conservative design should adopt the maximum value of n in the range considered applicable.

- 3) The effect of variations of the soil sinkage constant, k , on the calculated motion resistance increases with an increase in wheel load and is only significant in the case of the rigid wheel assumption. The required accuracy in the estimation of this parameter will depend to a great extent on the anticipated wheel load and wheel deflection characteristics. For the wheels investigated in this study, an accurate prediction of this parameter will not be required if wheel loads on the order of 100 pounds force are anticipated as the maximum error in motion resistance prediction would only be approximately 4 pounds.
- 4) The effect of variations of the soil strength parameters, c and ϕ , on the calculated value of thrust is significant and accurate prediction of these parameters is required if the vehicle performance is to be adequately evaluated.
- 5) An increase in the wheel load leads to an increase in the calculated thrust, motion resistance, and drawbar pull. However by taking the drawbar pull-weight ratio as an indicator of the slope climbing ability of a vehicle, the lighter the wheel load the steeper a slope the vehicle should be able to climb.
- 6) The characteristic wheel dimensions of contact width, contact

length, and diameter should be maximized from a trafficability viewpoint.

The comparison of the predicted metal wheel performance indicators to those measured by AC Electronics in a test program resulted in the following conclusions.

- 1) For those wheels tested, the predicted and measured values of thrust compared quite well at the low wheel loads. However, the deviation between the predicted and measured values was considerable for the larger wheel loads.
- 2) The measured values of the motion resistance of the wheel were enveloped by the two assumptions a) the wheel behaved as a rigid wheel and b) the wheel behaved as a track. The wheels tested exhibited values of motion resistance which suggest that this type of wheel behaves more like a track than a rigid wheel.
- 3) Even though deviations between predicted and measured values of the performance parameters were evident, the general shape of the predicted and measured thrust, motion resistance, and drawbar pull plots were similar.

A conclusive statement can not be made at this time concerning the applicability of the "Soil Value System" approach to the prediction of the mobility of the proposed lunar roving vehicle. Although the metal wheel test results presently available are encouraging, future wheel test programs are required. In addition modifications of the basic theory should be examined and, if possible, the approach must be extended to prediction of mobility on slopes. Studies are proceeding along these lines.

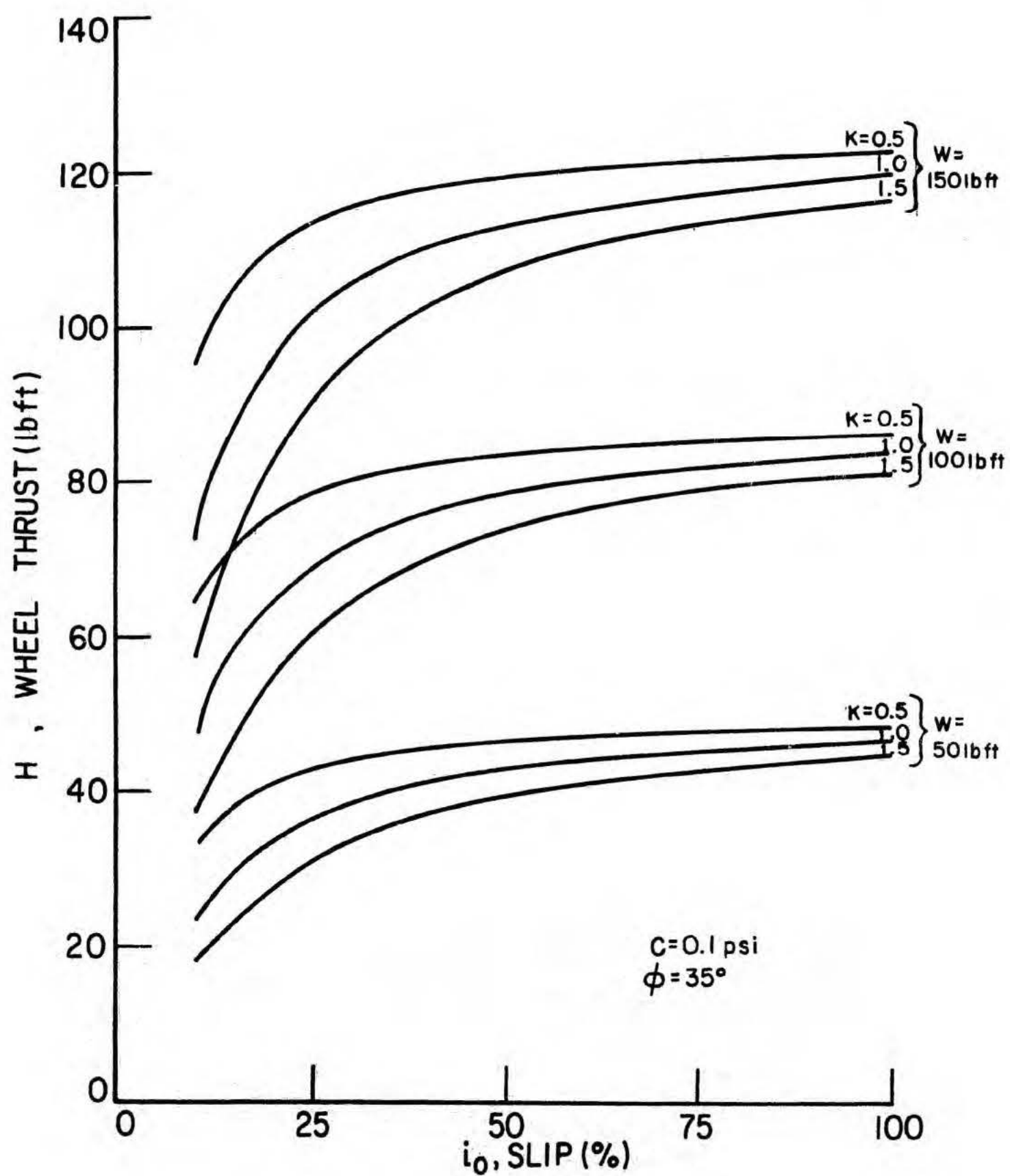


FIGURE 1. Wheel Thrust vs. Slip.

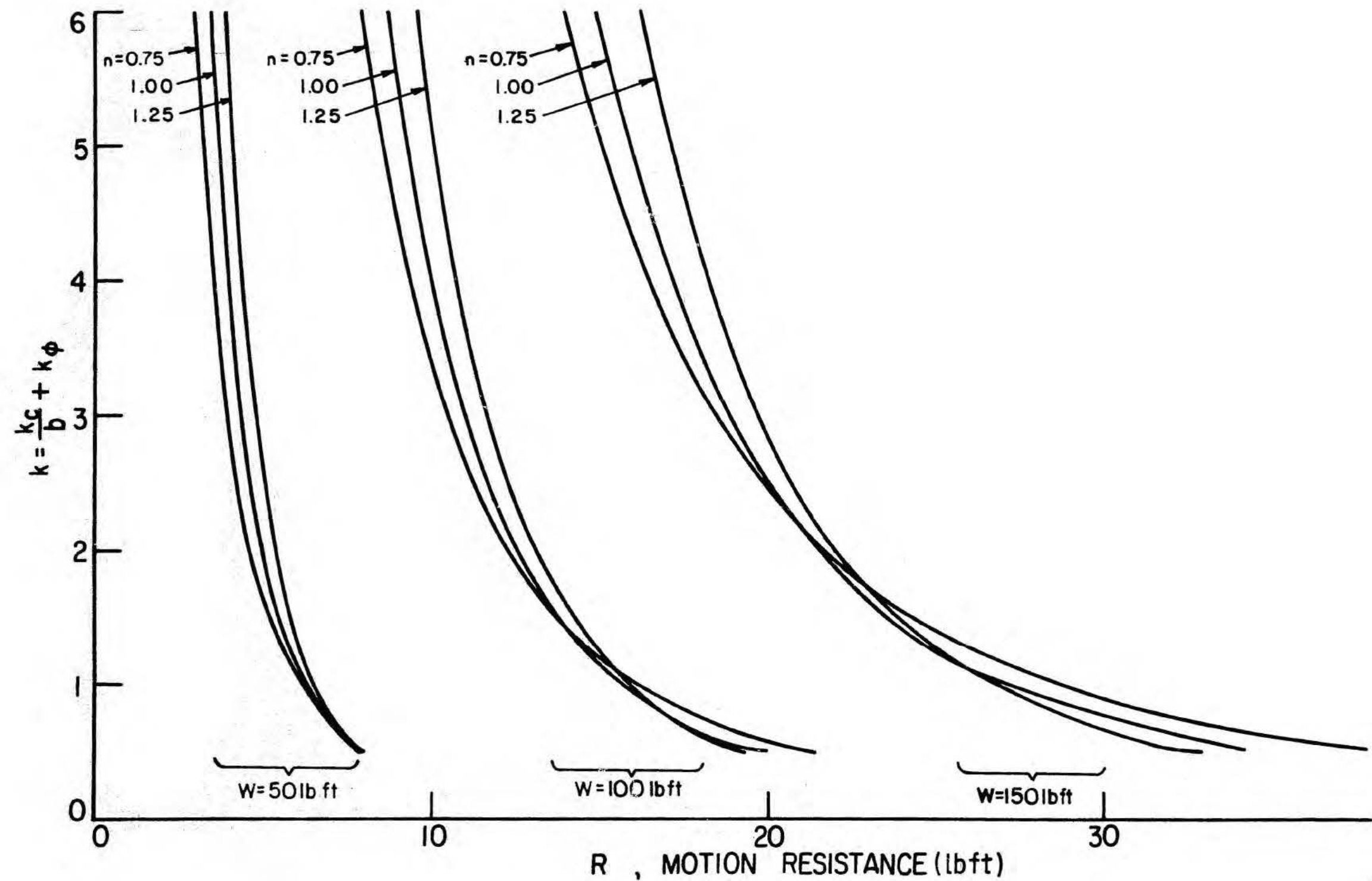


FIGURE 2. Motion Resistance vs. $(\frac{k_c}{b} + k_\phi)$ for a Rigid Wheel.

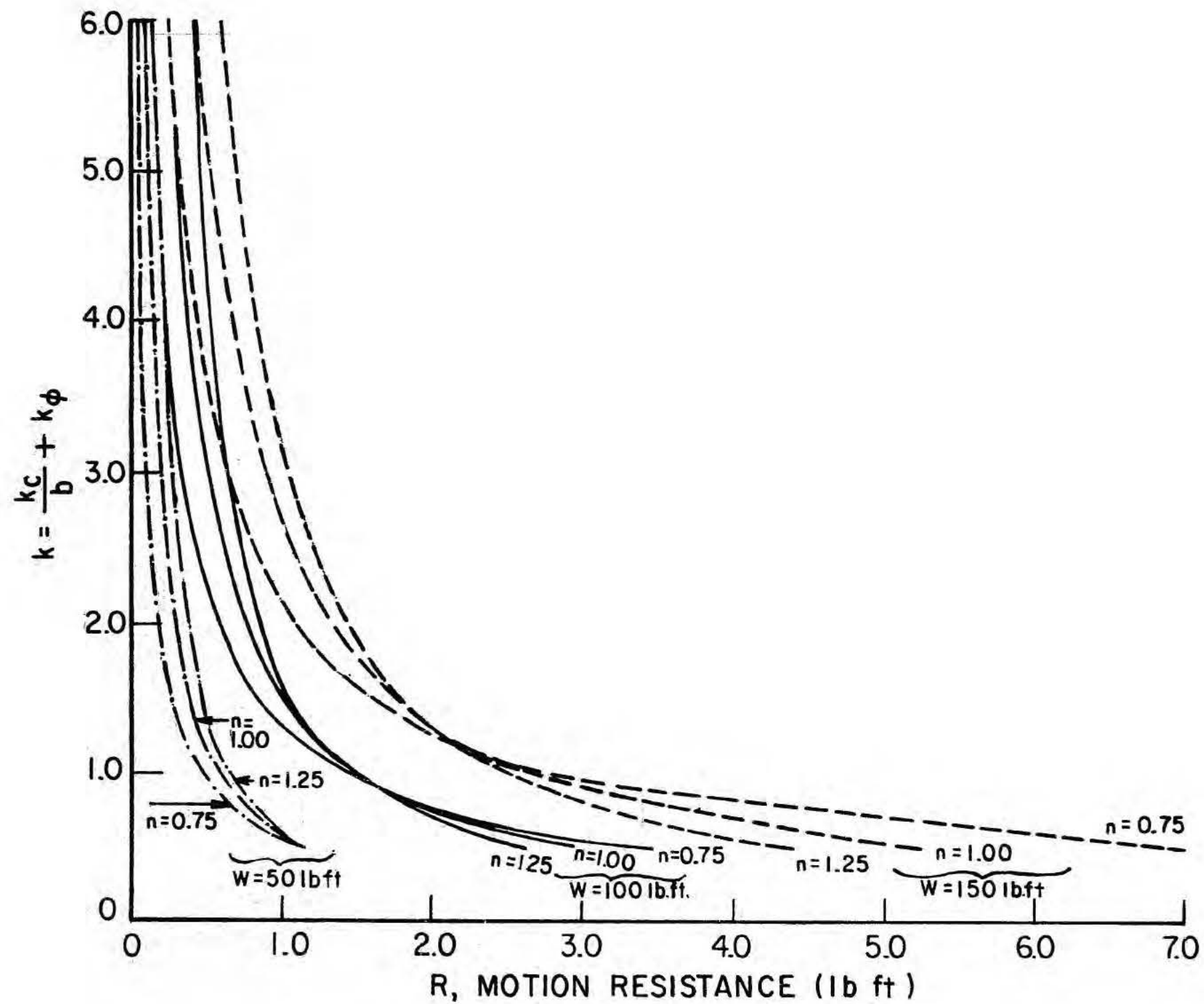


FIGURE 3. Motion Resistance vs $(\frac{k_c}{b} + k_\phi)$ for a Track.

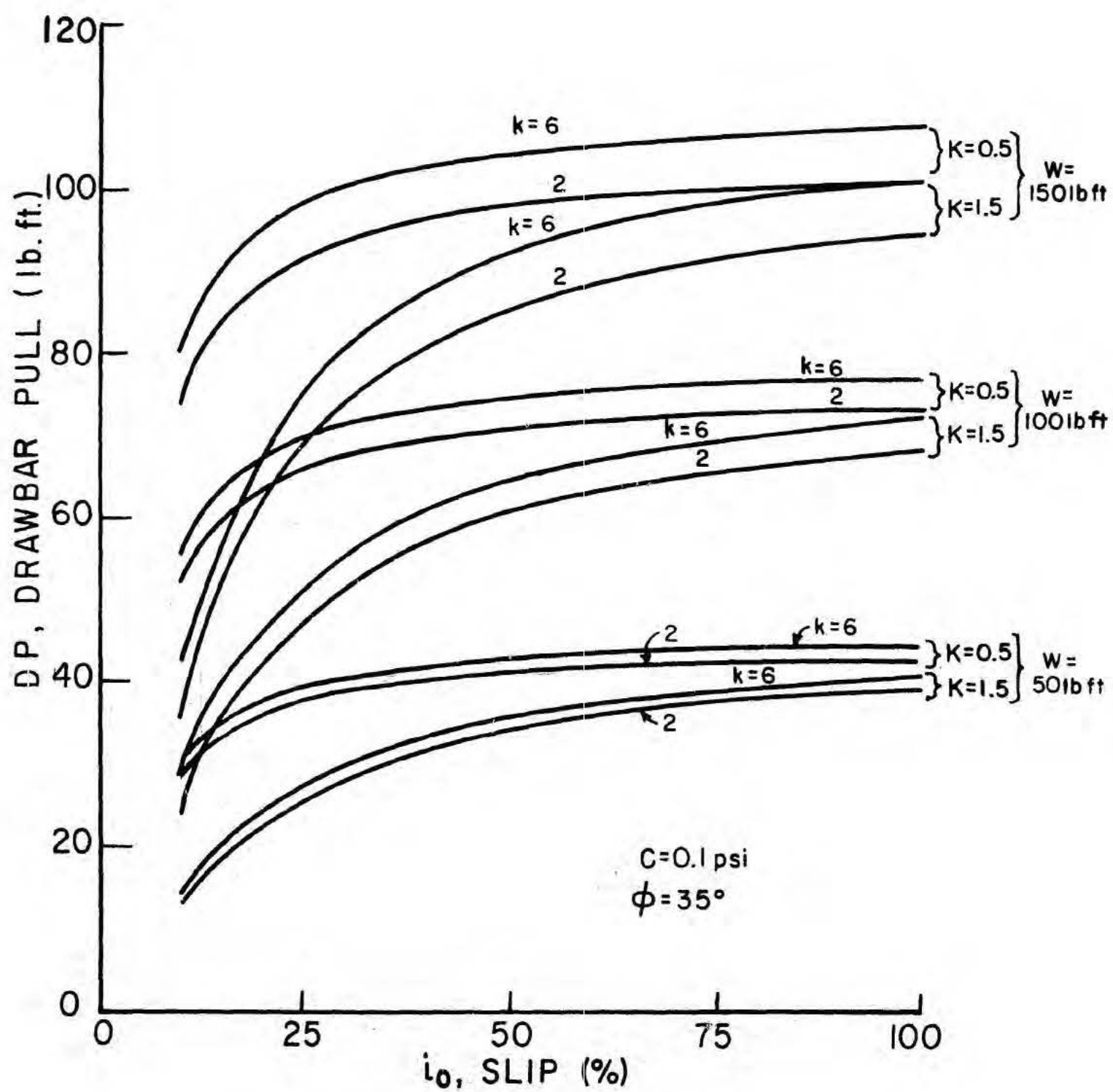


FIGURE 4. Drawbar Pull vs. Slip for a Rigid Wheel

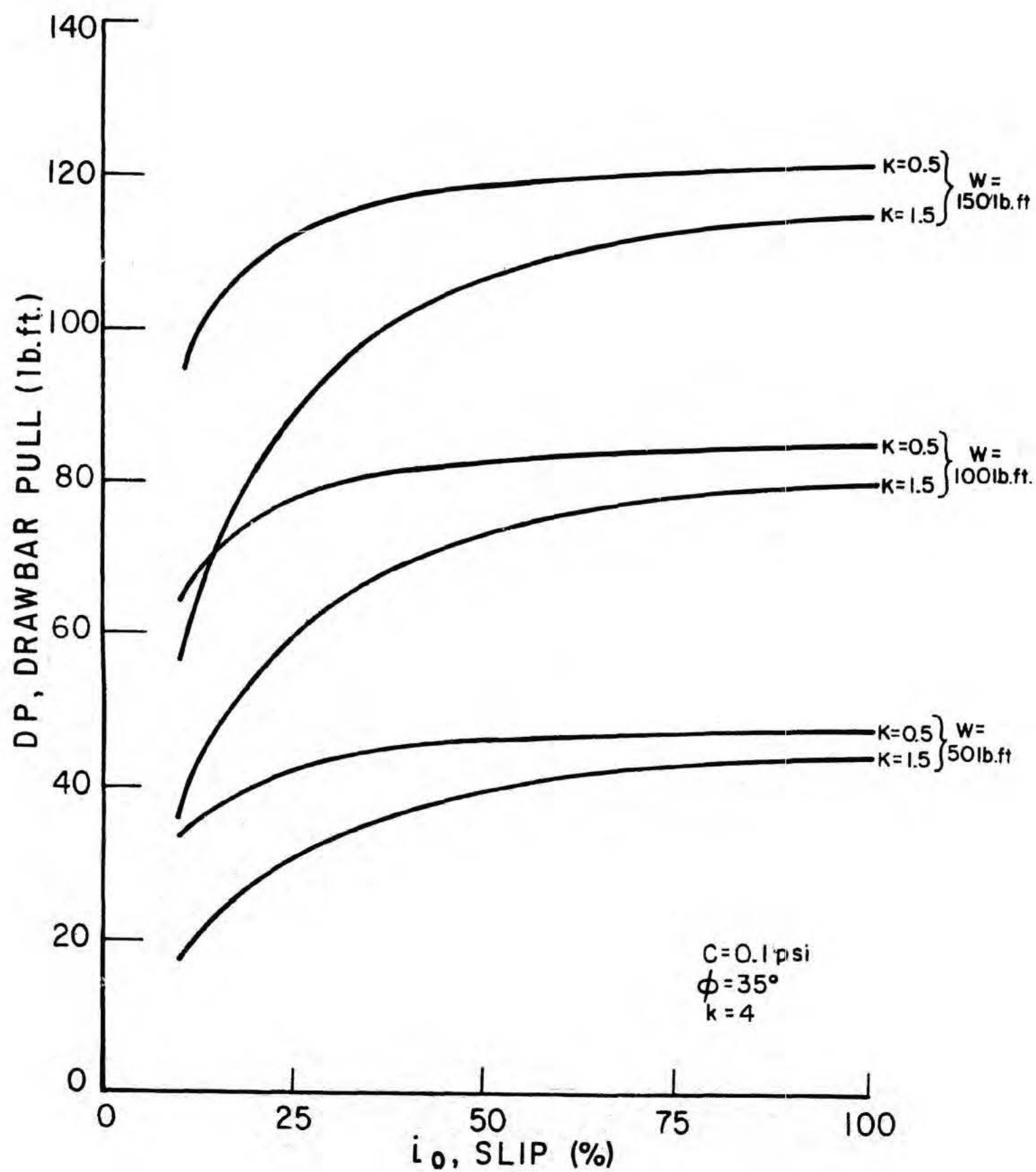
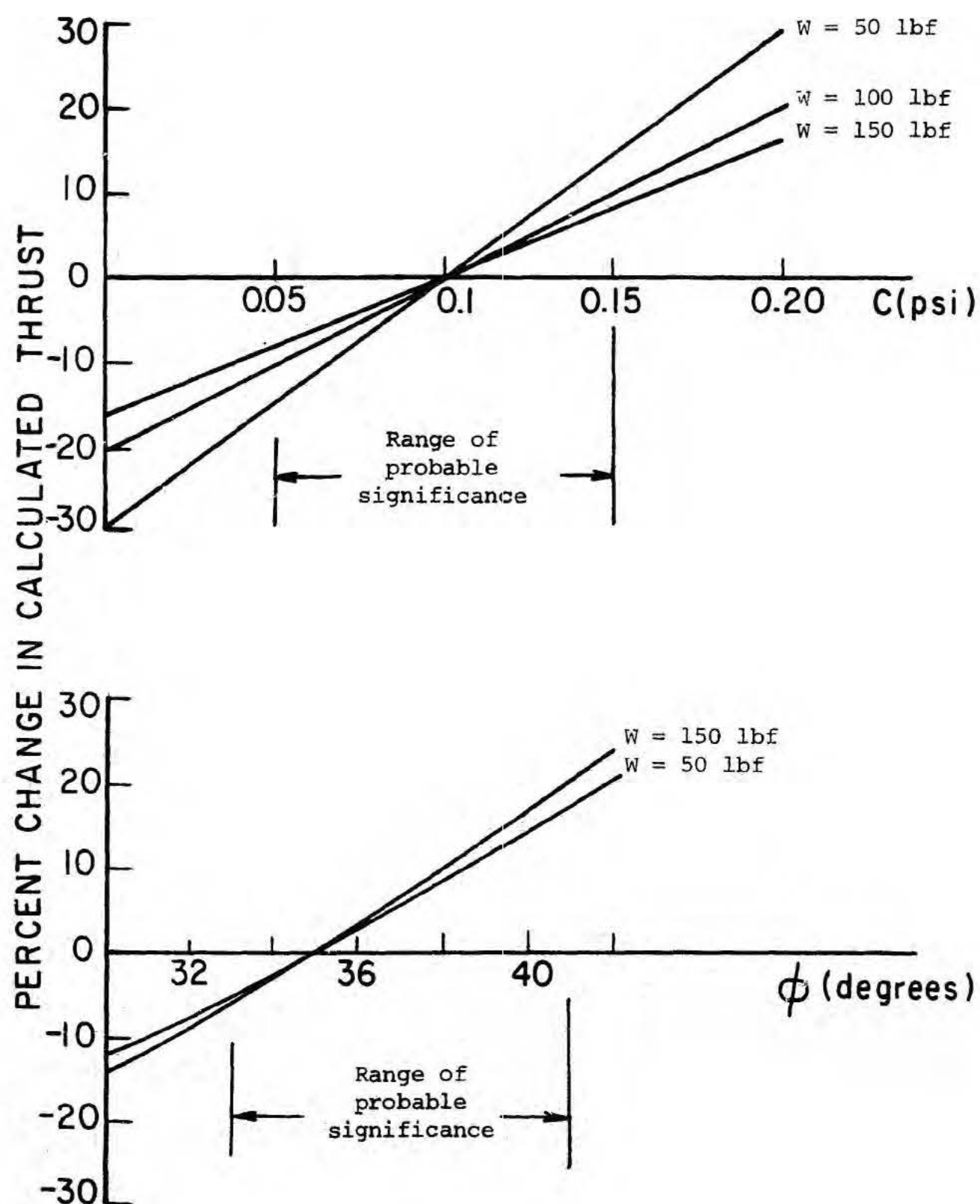


FIGURE 5. Drawbar Pull vs. Slip for a Track.

FIGURE 6. Percent Change in Calculated Thrust vs. c and ϕ .

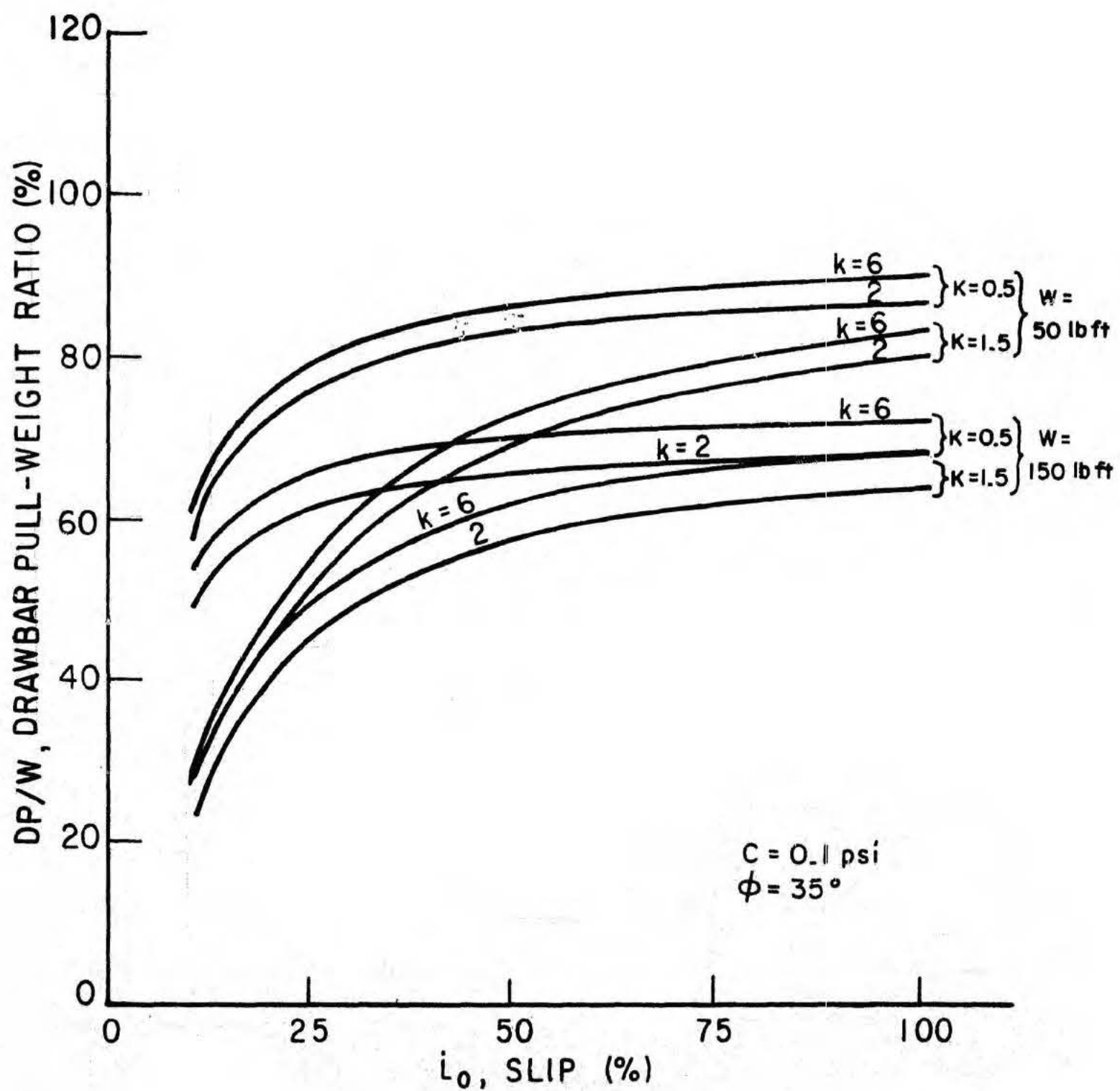


FIGURE 7. $\frac{DP}{W}$, Drawbar Pull - Weight Ratio for a Rigid Wheel.

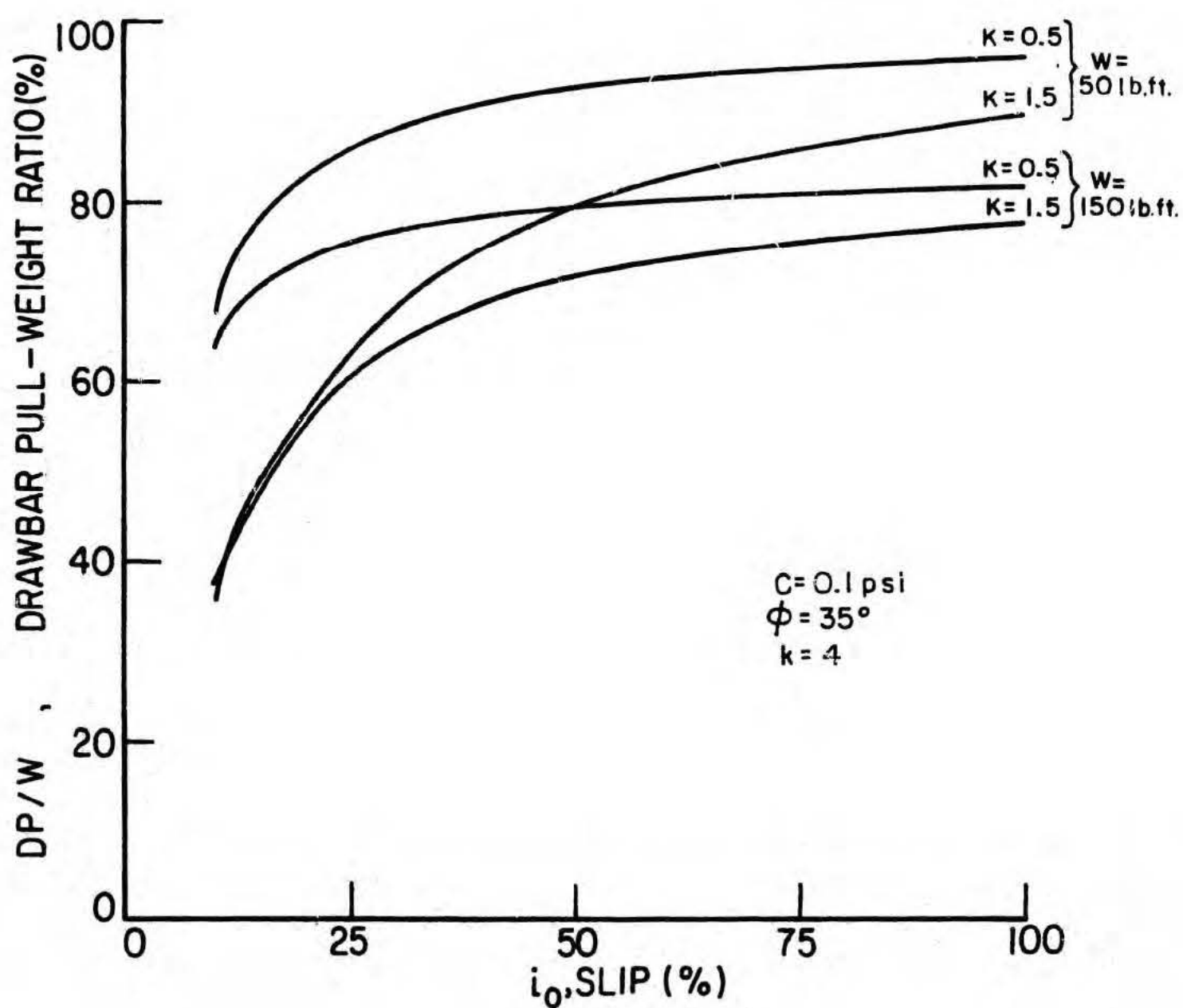


FIGURE 8. $\frac{DP}{W}$, Drawbar Pull - Weight Ratio for a Track.

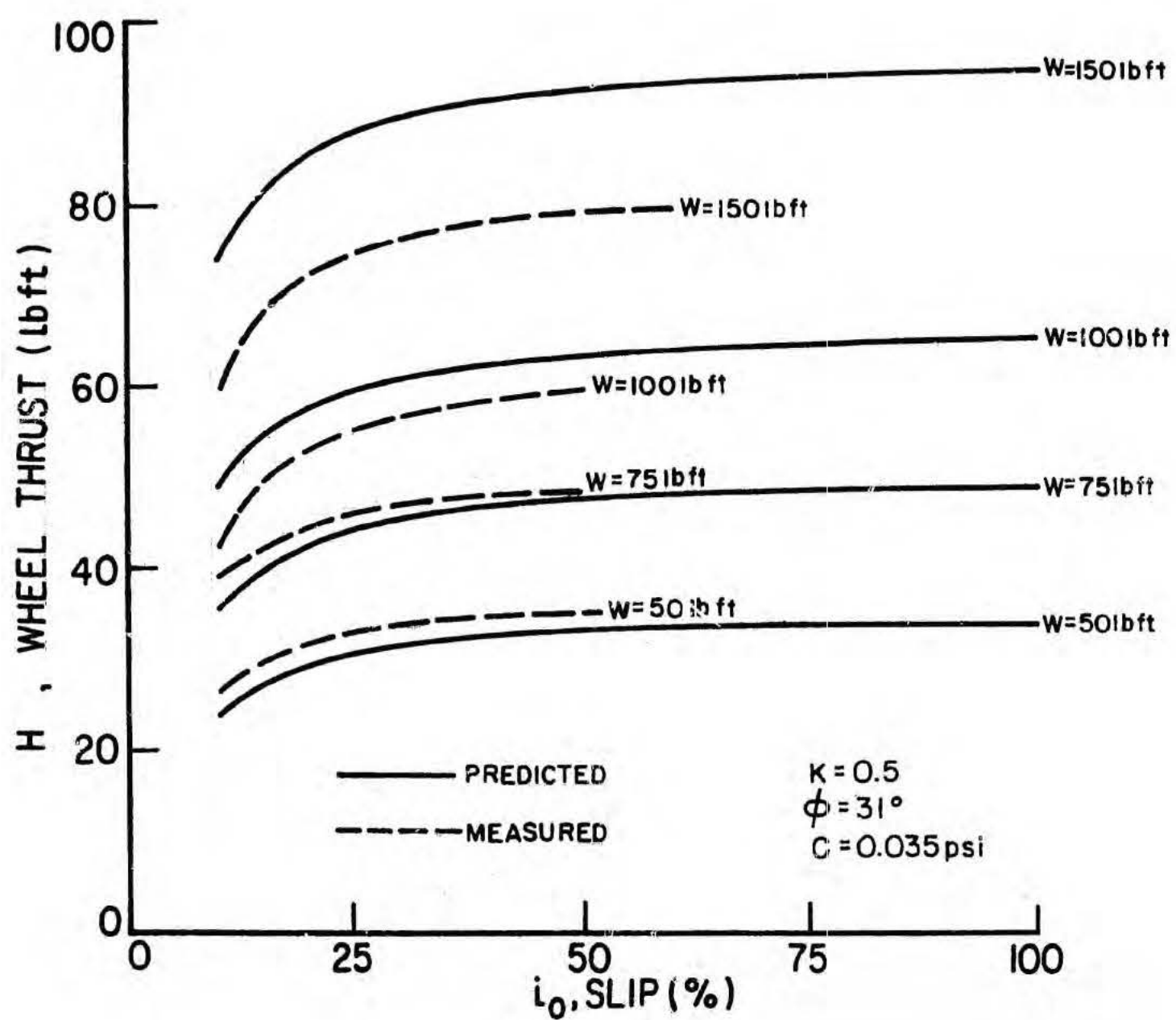


FIGURE 9. Comparison Between Predicted and Actual Wheel Thrust vs. Slip.

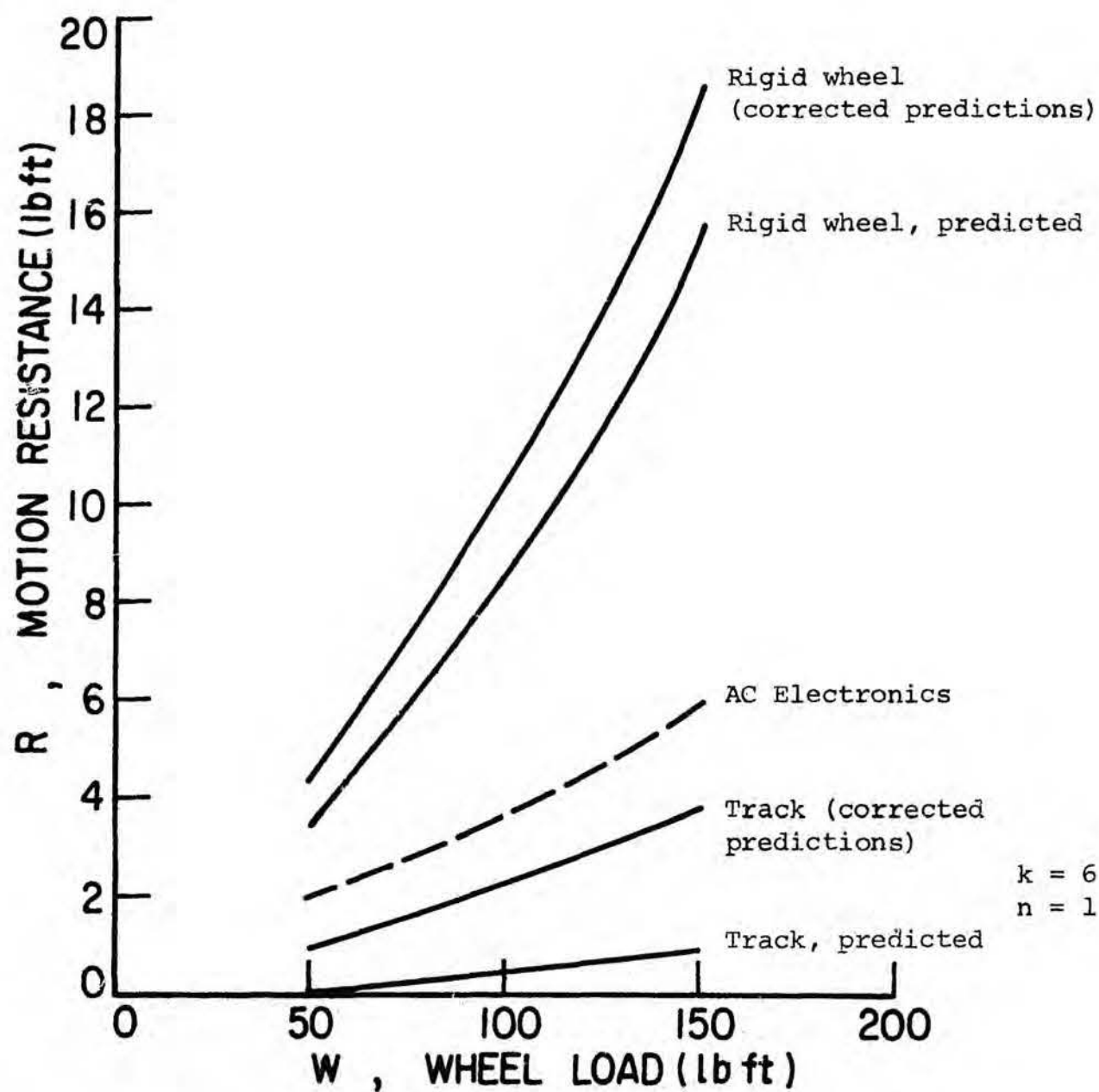


FIGURE 10. Comparison Between Predicted and Actual Motion Resistance vs. Wheel Load.

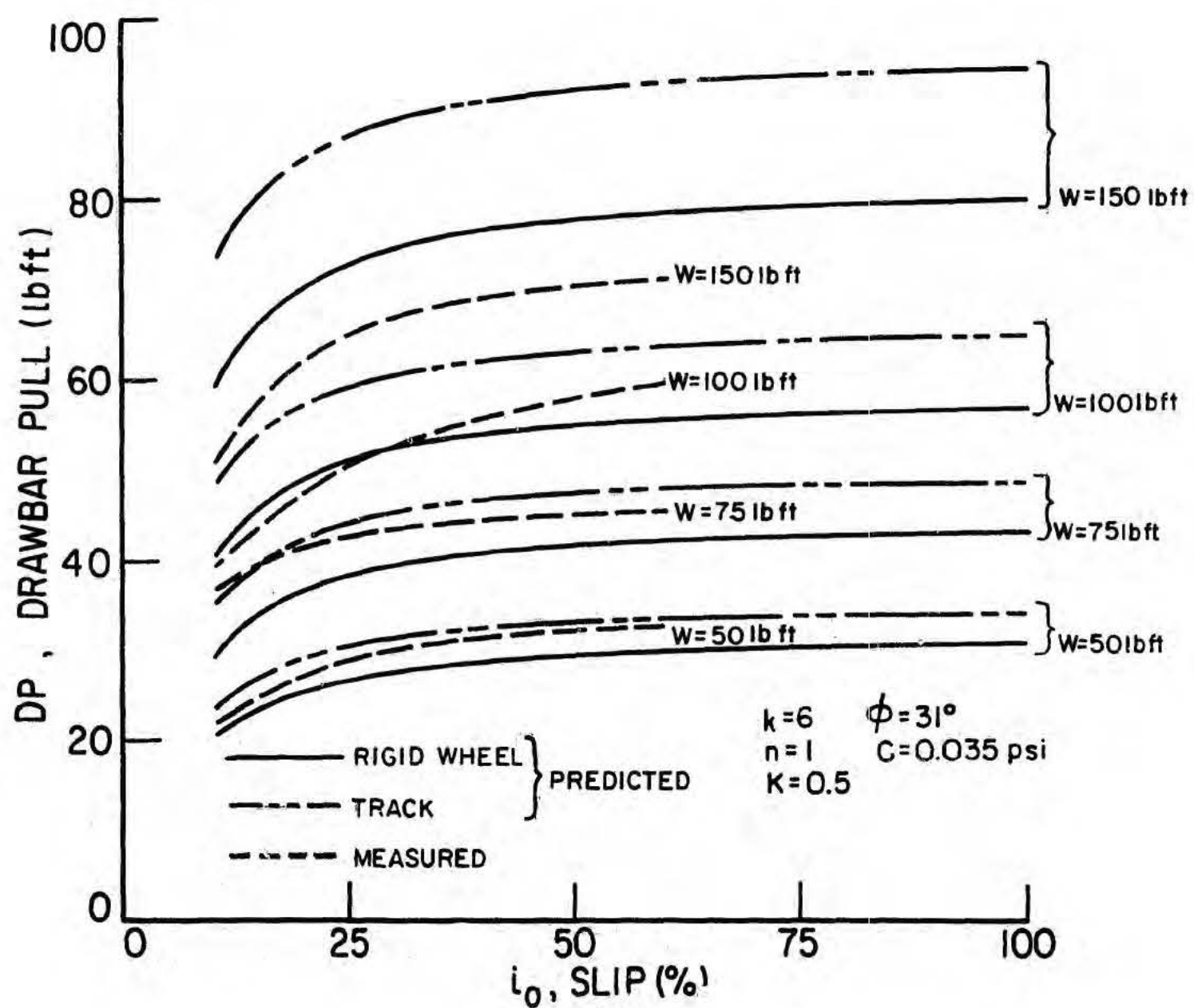


FIGURE 11. Comparison Between Predicted and Actual Drawbar Pull vs. i_0 Slip.

Bibliography

1. AC Electronics - Defense Research Laboratories (1967), "Lunar Wheel and Drive Experiment Test Program," 2 vols., Contract NASB-20267, June 1967.
2. Bekker, M. G. (1960), "Off-the-Road Locomotion," University of Michigan Press, Ann Arbor.

List of Symbols

- b - wheel or track contact width
- c - soil cohesion
- D - wheel diameter
- DP - wheel or track drawbar pull
- H - wheel or track thrust
- i_0 - slip of wheel or track
- K - soil stress-strain parameter
- k - soil composite load-deflection parameter
- k_c - soil load-deflection parameter
- k_ϕ - soil load-deflection parameter
- ℓ - wheel or track contact length
- n - soil load-deflection parameter
- R - wheel or track motion resistance
- W - wheel or track load
- ϕ - soil angle of internal friction

IV. CHEMICAL IMPREGNATION TECHNIQUES
AS RELATED TO LUNAR ENGINEERING APPLICATIONS

(T. S. Vinson and J. K. Mitchell)

1. INTRODUCTION

In the First Quarterly Report⁴ it was indicated that potential applicability of foamed plastics for the stabilization of unconsolidated lunar surface materials and for sealing of porous rock and soil masses for storage and shielding purposes was under investigation. The possibility of using foamed plastics for soil stabilization, particularly for lunar applications is attractive for the following reasons:

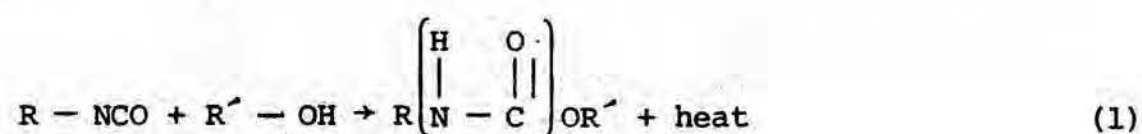
- a. The density of foamed plastics can be very low, thus providing the possibility of treatment of large soil and/or jointed rock masses with smaller quantities of stabilizer than would be possible using conventional stabilizers.
- b. Reactants of relatively low viscosity may be employed.
- c. The formation of closed-cell foams in soil pores will give impermeabilization.
- d. Foaming action may serve to force the stabilizer into larger soil volumes than reached by the initial injection.
- e. Reaction times are controllable.
- f. The economics appear favorable.

The current studies are aimed at determining the degree to which each of these factors may be realized. We are aware of no previous work with the specific purpose of soil stabilization by injection of foamed plastics. It is recognized that different potential lunar applications, e.g., preservation of unconsolidated soil structure for sampling purposes, treatment of large soil masses for strengthening purposes, sealing of cavity walls, will place different requirements on the material properties and injection techniques. It is also recognized that the harsh lunar environment will undoubtedly lead to differences in foaming action and treated soil properties from what would be obtained under terrestrial environment conditions.

Without losing sight of these factors, it has been considered appropriate first to investigate in some detail the chemistry of foamed plastics, the properties of the various ingredients in their initial state, the properties of foams by themselves, and the degree of success that can be obtained in injection under more favorable conditions than represented by fine-grained lunar soil and the lunar environment. As knowledge and experience accumulate the work will move more in the direction of actual lunar conditions and applications.

2. CHEMISTRY

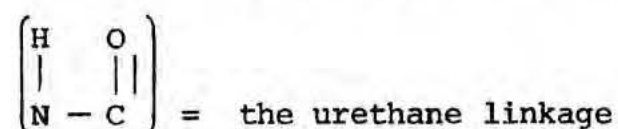
As noted in the First Quarterly Report urethane plastics have been selected as potentially the most useful of the different foam types. Urethanes are produced by the reaction of polyols with polyisocyanates. The general reaction is:



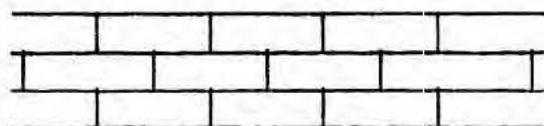
where,

$R - NCO$ = a polyisocyanate such as toluene diisocyanate

$R' - OH$ = a polyol; more generally any polyhydroxyl compound
(e.g. polyol, glycol, polyester, or polyether)



The above reaction involves mono-functional reactants, however, if polyfunctional chemicals are used polymers result. Functionality refers to the number of reactive sites per molecule. For example, toluene diisocyanate (TDI) may be represented as $NCO - R - NCO$. Since there are two NCO groups per molecule, TDI is said to be di-functional. If a tri-functional polyol is used with a diisocyanate then a cross-linked structure results. This may be represented diagrammatically as follows:

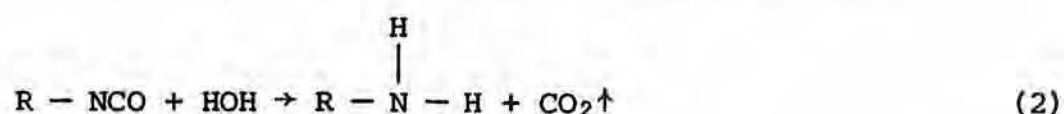


Catalysts, surfactants, and blowing agents may be incorporated in the reaction expressed by equation (1). Commonly used catalysts are tertiary amines and tin salts and are added to control or accelerate the rate of reaction so that gelation will be synchronized with maximum rise of the foam. Surfactants control cell surface tension and thus can render the foam large-celled or fine-celled. Polyglycol-silicone polymers represent a general class of compounds that can be used as surfactants.

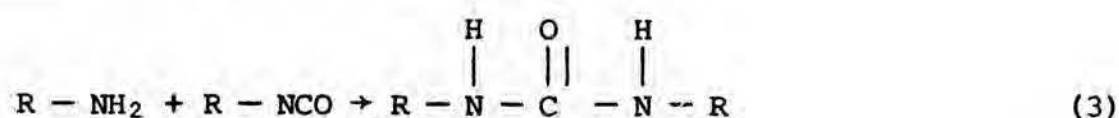
Blowing agents expand to form a gas in the polymer structure hence they are the agent responsible for the foam-like structure. Two classes of chemical blowing agents are possible. In the first the gas is produced by a chemical reaction within the polymer. In the second a chemical blowing agent decomposes in the presence of the exothermic heat of the reaction to produce the gas. Water would be in the former class of compounds. The gas produced in this instance is CO_2 . Low boiling fluorocarbons would be in the latter class of compounds.

The flexibility or rigidity of urethane foamed plastic is controlled by the functionability and molecular weight of the polyol and isocyanate used. Rigid foams result when low molecular weight highly functional polyols are used. Conversely, flexible foams result when high molecular weight low functional polyols are used. Variations between these two extremes for specific applications are possible.

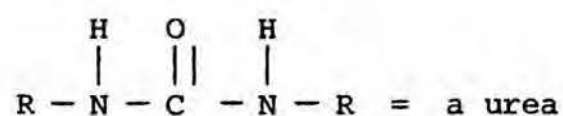
Ideally the urethane linkage would be the only one found in the polymeric structure. This is not the usual case. There are several other important linkages that may be present. One of the most common subordinate linkages occurs when water is present. The general reaction is:



This reacts with another isocyanate as follows

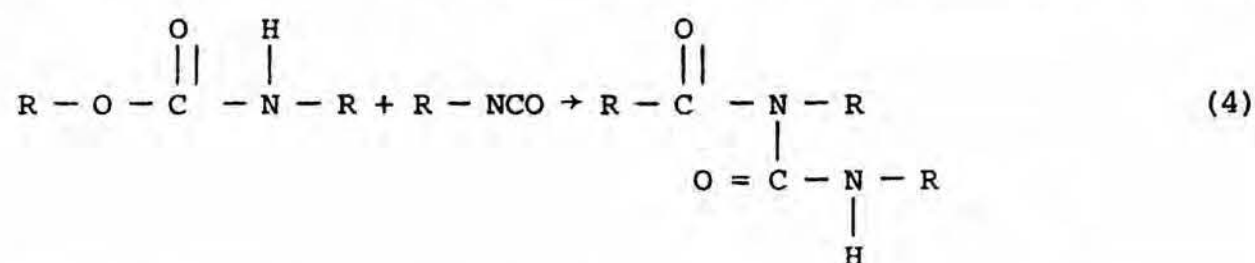


where,



Further, a cross-linking reaction will occur when the hydrogen on the nitrogen atom of the urethane group reacts with an isocyanate group.

This is known as the allophanate linkage and may be represented as follows:



In the general case all of these linkages will be forming simultaneously.

The preceding is intended only as a general presentation of the chemistry of urethane foamed plastics. More detailed treatments are presented in references 1, 2, and 5.

3. SELECTION OF URETHANE SYSTEM FOR PRELIMINARY INJECTION TESTS

For lunar engineering application there are three primary criteria that should be satisfied by a grout: (1) low viscosity, (2) a controllable gel time, and (3) a high ratio of stabilized volume to transported weight. Initial studies were concerned with satisfying the latter criterion. Current efforts are directed at determining the "best" system relative to the first two criteria while still satisfying the latter criterion. These investigations were made by mixing small quantities of the appropriate reactants in different proportions and observing the initial viscosity,

gel time, and characteristics of the foam after the reaction was complete. A urethane system consisting of a polyethylene glycol, toluene diisocyanate, nitrilotriethanol (a combination catalyst and crosslinking agent), and water appeared promising and was selected for preliminary injection tests into a coarse uniform sand.

4. PRELIMINARY INJECTION TESTS

It was found that this urethane system could be successfully injected into the voids of a loose, uniform coarse sand and that the mixture would foam in the voids of the soil mass. Fig. 1 presents the approximate relationship between volume of soil mass stabilized per gram of stabilizer versus catalyst content for stabilizer water contents of 2% and 4% (by weight). The urethane was composed of 55% polyol and 45% diisocyanate (by weight).

The general procedure used for obtaining these data was to place the sand in a mold and then insert a syringe cannula to a depth of 5 inches. A surcharge was then added to the sand. A given urethane mixture was poured into the syringe and injected into the soil mass producing a spherical stabilized mass. The volume of the mass was determined by jacketing the stabilized mass with a thin rubber membrane and observing the volume of water it displaced. The initial weight of the injected mixture was known. Also shown in Fig. 1 is the relationship for AM-9, a commonly used terrestrial chemical grout which polymerizes in the voids of the soil mass into which it is injected.

The chemical system used for these tests is more viscous than desirable and it is potentially useful only for injection into a fairly porous media with adequate overburden pressure. The tests have shown, however, that urethanes can be made to foam in the voids of a soil mass.

5. FURTHER STUDIES

Research presently underway is directed toward formulating a system with extremely low viscosity components and highly controllable gel times. A system employing a 1,3-propanediol, diisocyanate, and 4-methylmorpholine catalyst has been tentatively selected. The final formulation together with data pertinent to gel time-viscosity relationships will be given in a subsequent report. Once the finalized system has been selected it will be injected into a fairly porous soil media and the resultant stabilized soil mass will be tested for strength and impermeabilization and the characteristics of the foam structure and foam-soil interaction will be studied in some detail. Should these experiments prove highly successful experiments will be initiated on injection into a simulated lunar soil mass.³

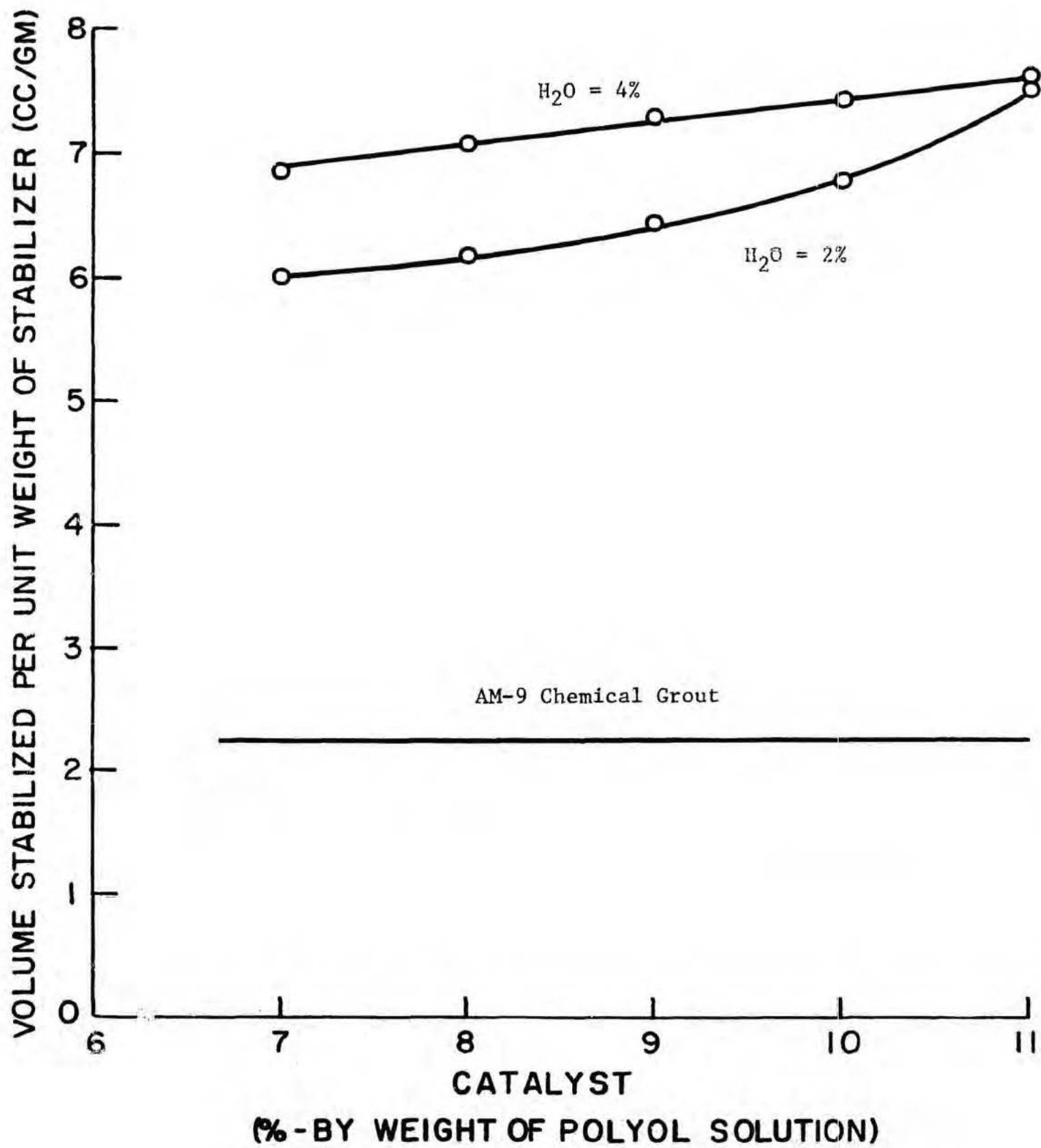


Figure 1. Volume of soil stabilized per gram of stabilizer versus catalyst content for stabilizer water contents of 4% and 2%.

REFERENCES

- ¹Dombrow, B. A., 1963, Polyurethanes, Reinhold Publishing Corporation.
- ²Ferrigno, T. H., 1963, Rigid Plastic Foams, Reinhold Publishing Corporation.
- ³Houston, W. N., Mitchell, J. K., Namiq, L. I., 1968, Lunar Soil Simulation, Lunar Surface Engineering Properties Experiment Definition. First Quarterly Report, submitted to National Aeronautics and Space Administration George C. Marshall Space Flight Center, October 1.
- ⁴Mitchell, J. K. and S. S. Smith, 1968, Chemical Impregnation Techniques as Related to Lunar Engineering Applications, Lunar Surface Engineering Properties Experiment Definition. First Quarterly Report, submitted to National Aeronautics and Space Administration George C. Marshall Space Flight Center, October 1.
- ⁵Phillips, L. N. and Parker, D. B. V., 1964, Polyurethanes, The Plastics Institute.

V. FAILURE OF A BOREHOLE IN SOIL OR ROCK UNDER DILATOMETER
LOADING AND UNDER BOREHOLE JACK LOADING.

(T. K. Van and R. E. Goodman)

1. INTRODUCTION

The failure of an infinitely long circular borehole under dilatometer loading in an infinite homogeneous mass has been studied by many investigators. Solutions have been obtained for different property assumptions and failure criteria, for soils and for rocks. Solutions to the same problems with borehole jack loading are not available, to our knowledge. Studies are being made, using finite element analysis, analytical limit analysis, and also by experimentation in the laboratory.

2. FAILURE OF AN INFINITELY LONG BOREHOLE BY DILATOMETER LOADING

The problem is that of a thick-walled cylinder under internal pressure, with the outer radius approaching infinity. For a homogeneous and isotropic medium, due to the condition of symmetry, radial stress and circumferential stress are principal stresses. The solutions were first obtained by Lamé (Seely and Smith, 1959). For small values of ambient pressure (pressure at infinity), p , the maximum value of circumferential stress occurs at the inner surface and equals the applied pressure. The borehole will fail in tension at every point on the borehole surface when the applied dilatometer pressure reaches the tensional strength of the medium. As the

dilatometer increases, fracture lines are formed, and extend to a radius R . The lines of fracture can be assumed to be logarithmic spirals (Bray, 1967) making a constant angle δ to the principal radial direction at every point (Fig.2). In the fractured zone, the shear resistance (on spirals) includes cohesion and friction, the failure criterion is: $(\Sigma_r + H) = K(\Sigma_\theta + H)$

$$\frac{1}{K} = \cot(|\delta| + \phi) \tan|\delta| \quad (1)$$

$$(\Sigma_r + H) = (p_i + H) \left(\frac{r}{a}\right)^q \quad q = \frac{1}{K} - 1 < 0 \quad (2)$$

The stress distribution in the remaining elastic mass:

$$\begin{cases} \Sigma_r = p + \frac{b}{r^2} \\ \Sigma_\theta = p - \frac{b}{r^2} \\ \tau_{r\theta} = 0 \end{cases} \quad (3)$$

Assume that the failure criterion of the solid is of Coulomb-Navier

type: $\Sigma_r = h\Sigma_\theta + j$

at $r = R$

$$\begin{cases} \Sigma_r = h\Sigma_\theta + j = p + \frac{b}{R^2} \\ \Sigma_\theta = \frac{1}{K}(p_i + H) \left(\frac{R}{a}\right)^q - H = p - \frac{b}{R^2} \end{cases} \quad (4)$$

$$R = a \left\{ K \frac{(2p - j) + H(h + 1)}{(h + 1)(p_i + H)} \right\}^{\frac{1}{q}}$$

$$b = \left\{ \frac{(h - 1)p + j}{1 + h} \right\} R^2 \quad (5)$$

It can be seen that the weaker the material the greater the radius of the fractured zone. It is a function of angle δ which is related to the failure criterion of the solid mass. Bray suggested that the appropriate value for δ would be $45^\circ + \phi_s/2$, with $\tan \phi_s$ as the friction constant. The parabolic Griffith criterion of failure, and a modified form suggested by McClintock and Walsh, composed of the Griffith parabola and a straight line, do not well approximate the actual fracture strength of rock. Fairhurst proposed a more flexible empirical criterion (Fairhurst, 1964):

$$\Sigma_3 = T_s \quad \text{if} \quad \Sigma_1 + m(m - 2) \Sigma_3 < 0$$

$$\text{or} \quad \frac{(\Sigma_1 - \Sigma_3)^2}{\Sigma_1 + \Sigma_3} = 2(m - 1)^2 T_s \left(1 + \frac{2T_s}{\Sigma_1 + \Sigma_3} \left\{ \frac{(m - 1)^2}{2} - 1 \right\} \right) \quad (6)$$

$$\text{if} \quad \Sigma_1 + m(m - 2) \Sigma_3 \geq 0$$

Mohr's representation of the failure criterion is given by the equation of the Mohr's envelope

$$\tau^2 = (m - 1)^2 T_s (T_s - \Sigma) \quad (7)$$

where $m = (n + 1)^{1/2}$ with $n = -\frac{Q_u}{T_s} = \frac{\text{unconfined compressive strength}}{\text{tensile strength}}$

Ladanyi, (1967, 1968) solved the problem of the static expansion of spherical and cylindrical cavities in an infinite medium which is linearly elastic before failure, and which obeys the Fairhurst's failure criterion; after failure, the crushed mass possesses a Mohr-Coulomb failure criterion. The solutions for a cylindrical cavity could be used for dilatometer problems. For low absolute values of the ratio of the ambient pressure to the tensile strength (Ladanyi, 1967), at failure, three zones exist simultaneously: the crushed, radially cracked, and elastic zones (Fig. 3a). The material in the radially cracked zone cannot carry tension in the circumferential direction. At high ambient pressure, this zone does not appear. For $n \geq 4.82$ there is no radially cracked zone. The stress distribution and the displacements everywhere are known, as well as the pressure-expansion relationships $p_i = f(V_i/V_{i_0}) = \frac{\text{internal volume}}{\text{initial internal volume}}$

$$\frac{p_i + S_c}{Q_u + S_c} = \left(\frac{1 - (1 - e_{av})(V_i/V_{i_0})}{2(u_f/r_f) + e_{av}} \right)^b$$

(8)

$$b = \frac{\sin \phi}{1 + \sin \phi} \quad S_c = c \cot \phi$$

$\frac{u_f}{r_f}$ = relative displacements of the inner boundary of the cracked zone
 where u_f = displacement at the inner boundary of the cracked zone and
 r_i = inner radius of the cracked zone.

$$\frac{u_f}{r_f} = \frac{1 + \nu}{E} (p_0 - T_s) \frac{Q_u}{2p_0 - T_s} + \frac{Q_u}{E} (1 - \nu)^2 \frac{1}{2} \left(\frac{Q_u}{2p_0 - T_s} \right)$$

$$e_{av} = \frac{\text{Volume of crushed zone after expansion}}{\text{Volume of intact rock in the crushed zone}} - 1$$

The ultimate internal pressure is that for $\frac{V_i}{V_{i0}} = \infty$

$$\frac{p_{ult} + S_c}{Q_u + S_c} = \left(\frac{u_f}{2r_f} + e_{av} \right)^{-b} \quad (9)$$

For high values of the ratio (p_0/T_s) the radially cracked zone is absent (Fig. 3b). The pressure-expansion relation is given by:

$$\frac{p_i + S_c}{p_0 + S_c + Q_u \cdot G} = \left(\frac{1 - (1 - e_{av}) [V_i/V_{i0}]}{[2(1 + \nu)/E] Q_u \cdot G + e_{av}} \right)^b$$

with

$$G = \frac{1}{m + 1} \left(n \frac{p_0}{Q_u} + 1 - \frac{1}{4} (m - 1)^2 \right)^{1/2} \quad (10)$$

The ultimate internal dilatometer pressure (Ladanyi, 1967)

is obtained implicitly as follows:

$$\frac{p_{ult} + S_c}{p_0 + S_c + Q_u \cdot G} = \left(2 \frac{1 + \nu}{E} Q_u \cdot G + e_{av} \right)^{-b} \quad (11)$$

It can be seen that the ultimate cavity pressure is controlled by many factors: the strength parameters in intact and broken states; deformability (E); the ambient pressure; and the density change due to the change of state (Ladanyi, 1967).

The problems of dilatometer loading and borehole jack loading in soils are different from those in rocks, mainly due to the plastic behavior of soils and their inability to carry tension. The interpretation of the failure in soil masses caused by a dilatometer can be based on a number of available solutions. In the studies of punching of metals, Bishop, Hill and Mott (1945) solved the problem of an expanding spherical or cylindrical cavity in an infinite frictionless medium. In the investigation of the problem of the dilatometer in clays, Menard (1957), Kérisel, Anderson and Gibson (1961) solved the cases of an expanding cylindrical cavity in a cohesionless medium. The same problem for an expanding spherical cavity was obtained by Skempton, Yassin, and Gibson (1953) in the study of pile bearing capacity. To deal with the problem of the expansion of a cavity in a saturated clay medium under undrained condition, Ladanyi (1963) treated the problem semi-empirically. The solution is based on stress-strain curves and strain-volume change relationships obtained by conventional triaxial tests. The problem is solved by step-by-step numerical integration method. More general solutions for expanding spherical and cylindrical cavities in media possessing both cohesion and friction were obtained by Vesic and Barksdale (1963), in a study on cratering mechanisms. For special cases, frictionless or cohesionless media, these solutions reduce to those obtained by earlier investigators for these cases.

The assumptions made by Menard (1957) in the solution for clay ($\phi = 0$) were based on observation of the curve relating deformation to pressure. Within the low initial pressure range, linear elasticity applies. Radial deformation is obtained by Lamé's solution for an infinitely thick cylinder. Poisson's ratio is taken as 0.50 for saturated clay. At intermediate pressure range, a zone of plastic equilibrium develops around the cavity in which the clay is assumed to be incompressible. Outside this zone, elastic equilibrium exists. The deformation increases exponentially with pressure in this range (Fig. 4). For an interval of pressure $p_1 - p_2$ in the plastic range, the average value of the radius of the Mohr's circle is given by Menard (1957):

$$R = \frac{p_1 - p_2}{\log u_1 - \log u_2} \quad (12)$$

where u = displacement

$$u = \rho \frac{1 + \nu}{E} c p^2 e^{\frac{p - p_0 - c}{c}} \quad (13)$$

and $c = \text{a constant} = \frac{dp}{du} u$

There is a stage of the loading where the deformation increases greatly without any increase in pressure. The deformation becomes very large compared to the initial cavity radius. The pressure deformation curve is limited by a vertical asymptote $p = p_{ult}$.

$$p_{ult} - p_0 = c(1 + K)$$

p_0 = pressure at zero deformation.

$$K = \log \frac{E}{2c(1 + \nu)} = \text{relative rigidity}$$

To analyze the cratering caused by a concentrated point charge of explosive or line charge, Vesic and Barksdale (1963) obtained the solution of an expanding spherical or cylindrical cavity of zero radius in a soil mass possessing both friction and cohesion.

At an internal pressure p_u , plastic deformation takes place around the cavity until it becomes large enough to maintain equilibrium (Fig. 5). A zone of plastic equilibrium exists around the borehole (cavity); the rest of the medium is in elastic equilibrium. The solid is assumed to be rigid-plastic in the plastic zone, and linear-elastic in the zone outside. The change in cavity volume is equal to the change of volume in the elastic zone. The infinite medium is subject to a hydrostatic initial pressure q . The solution for the ultimate pressure can be rearranged into the form (Vesic, Barksdale, 1963):

$$p_u = cF_c + qF_q \quad (14)$$

F_c, F_q = cavity expansion factors.

$$F_q = (1 + \sin \phi) \left(\frac{I_r}{2 \cos \phi} \right)^{\frac{\sin \phi}{1 + \sin \phi}} \quad (15)$$

$$F_c = (F_q - 1) \cot \phi$$

I_r = soil rigidity index, the ratio of soil rigidity $\frac{E}{1 + \nu}$ to initial shear strength $(c + q \tan \phi)$.

The radius of the plastic zone is given by:

$$\left(\frac{R_p}{R_u} \right) = \left(\frac{I_r}{2 \cos \phi} \right)^{1/2} \quad (16)$$

For frictionless media ($\phi = 0$), $F_c = \ln \left(\frac{I_r}{2} \right) + 1$, equal to the value found by Gibson and Anderson. The expansion factors for a spherical cavity are larger than those of a cylindrical one. The slope effects increase with increasing ϕ and increasing I_r . The actual expansion factors for a dilatometer should be larger than those of an infinitely long cylinder. The values for the factors are available for the whole range of ϕ and rigidity index (Vesic and Barksdale 1963).

3. FAILURE OF A BOREHOLE UNDER JACK LOADING

To our knowledge little had been done with the problems of failure of a borehole in rocks or in soils under jack loading. There are a number of factors that complicate the problem. The problem is not axisymmetric. The distribution of contact pressure, the induced state of stress, the deformation, and the mode of failure, are all affected by the properties of the medium, and the geometry of the problem.

The distribution of contact pressure depends on the relative rigidity between the bearing plate and the material, the bearing plate dimensions, the roughness of the borehole wall, the properties of the material, and the magnitude of the applied pressure. Wyanecki (1968)

(Fig. 6a) assumed that the contact pressure is purely radial, with the maximum value at the center of the bearing plate. The distribution was based on radial and tangential strains measured by strain gages very close to the edge of the borehole. Goodman, Heuzé, and Van (1968) assumed that the contact pressure is unidirectional and uniform (Fig. 6b). For a small bearing plate width, it is reasonable to assume that there is uniform radial contact pressure. When the medium is soil, the problem is closer to that for uniform unidirectional displacement, because the bearing plate is much more rigid than the medium. For sand the contact pressure at the edges of the bearing plate is small because of low confinement (Fig. 6c). For clay ($\phi = 0$), the minimum value is at the center, because at the edges, larger pressure is needed to cause the same amount of deformation as at the center (Fig. 6d). For $c - \phi$ materials, the minimum contact pressure is at the center of the plate for low load range, and the maximum contact pressure is at the center for large loads (Fig. 6e).

The mode of failure depends on the properties of the medium and the geometry of the loading. The problems are different for soils and for rocks.

(a) Failure of solid under borehole jack loading:

Some experimentation done on concrete cylinders and on plaster-based simulated brittle materials during this project showed that one mode of failure is tensional cracking. Maximum tensional stresses are developed at the edge of the borehole, but not necessarily at $\theta = \pm 90^\circ$ ($\theta = 0^\circ$ at the center of the bearing plate) because of the non-axisymmetry

of the problem. The magnitude and the location of the maximum tensional stress depend on the magnitude, distribution and direction of contact pressure. For uniform unidirectional jack pressure in a homogeneous elastic, isotropic medium, finite element analysis showed that maximum tension occurs very close to the edge of the bearing plate. The maximum tension occurs at $\theta = 90^\circ$ when the bearing plate is a semi-circle ($2\beta = \pi$). For a given applied load the magnitude of the maximum tensional stress decreases rapidly and the maximum compressional stress, at the center of the plate increases as the bearing plate width is reduced. For a given material under jack loading, it is conceivable that when the width of the bearing plate is small enough, a different mode of failure occurs before the maximum tensional stress reaches the tensional strength of the medium. The problem is to find the proper failure criterion. It is impractical to solve this intractable problem analytically.

Finite element analysis is being used to study the problem. The approach, assumptions and failure criteria are those used by Goodman (1968) in a study on effects of joints on strength of tunnels. The rock masses are blockwise isotropic or orthotropic, linear elastic. The failure criterion is

$$\tau_{\text{oct}} = N + D \Sigma_{\text{oct}}^B \quad \text{for} \quad \Sigma_{\text{oct}} > 0$$

and

$$(\Sigma_{\text{oct}})_{\text{min}} = \Sigma_t \quad \text{for} \quad \Sigma_{\text{oct}} < 0$$

where Σ_t = uniaxial tensile strength Σ_{oct} and τ_{oct} are the octahedral normal and shear stresses, and N , D , B are material properties.

With the finite element computer program available, both loadings in form of pressures and point loads can be accommodated. The effects of joints and different materials in the rock mass can be included and the propagation of cracks can be considered. Study is in progress for a range of material properties.

There is another mode of failure — local punching — which could apply here. This mode is observed in brittle material under concentrated loading (Ladanyi, 1968).

(b) Modes of failure of soils under borehole jack loading:

For soils, the problem is different mainly due to plastic behavior and inability to carry tension. The failure mechanism of a borehole in soil under jack loading will be proposed here. The validity of the hypothetical mechanism and its solution are to be verified by experimentation. The mechanism of failure is different for expanding soils (dense sands and stiff clays) than for contracting soils (loose sands and soft clays).

a) Expanding soils. For a wide bearing plate, as the load is increased, tensional stresses are developed in the regions close to the edges of the plates. Tensional fracturing occurs at the early stage of loading, creating zones of no stress as shown in Fig. 7. The no-stress zones extend deeper into the medium as the load is increased and two half spaces are formed. The material below the plate shears along the surfaces shown. Probably a crushed zone forms below the plate.

With narrow bearing plates, there is no tension failure. The problem is that of a strip footing on a curved surface. Both Prandtl mechanism of failure and Hill mechanism are possible (Fig. 8). The Hill mechanism is chosen because it gives a more appropriate velocity field (Finn, 1965; Hill, 1951).

β) Contracting soils. Under jack loading, loose sands and soft clays fail by forming a plastic bulb below the plate. The material in the bulb is in plastic equilibrium, the material outside is in elastic equilibrium (Fig. 12).

(c) Upper and lower bound failure solutions in soils:

Limit analysis method in plasticity is being used to find the solutions for the problems of failure of expanding soils by jack loading by the proposed mechanisms. In principle, it is difficult to find an exact solution, therefore an upper bound and a lower bound are estimated. The true solution is within their range. If the two bounds coincide, they are the solution (Finn, 1965; Ladanyi, 1968). To find a lower bound one tries to guess a statically admissible stress field, then to determine the load which induces this stress field. For the upper bound, a kinematically admissible velocity field is guessed. A failure mechanism is assumed based on experience and intuition, and one finds the load which causes this failure. A number of stress fields are considered; the smallest upper bound and the largest lower bound constitute a bracket. The brackets are narrowed by repeated trials.

α) Upper bound solution for small bearing plate in expanding soils.

For small bearing plate widths, the plate is assumed to be flat (Fig. 9). The failure surface includes: the straight line AC, making an angle $(45 + \phi/2)$ with the base AB; a logarithmic spiral CD, making an angle ϕ with every radius drawn from B, and a curve which can be approximated by a number of straight lines DE, EF, FG. Radial shear exists in the spiral zone BCD. The amount of energy dissipated along AC, CD, and within the deformable zone of radial shear is readily calculated. The remaining discontinuous velocities are determined graphically by a hodograph.

The energy dissipated on each discontinuous line is equal to $cLV \cos \phi$ where,

c = cohesion

L = length of the line

V = velocity obtained from hodograph

The energy dissipated on CD and in BCD is equal to (Finn, 1965):

$$c \cot \phi V_1 BC (e^{\pi \tan \phi} - 1)$$

V_1 = velocity for AC.

The total energy is minimized by using various assumptions of discontinuous surfaces AEFG.

β) Lower bound solution for small bearing plate in expanding soils.

A lower bound solution of a strip foundation at a bottom of a symmetrical valley, solved by Chen (1966), is adapted to the given problem as shown in Fig. 10. The lower bound is improved by an improved stress field which includes stress fields in the trapezoid (FDDF) and the wedge (CDH) under a unilateral pressure. The trapezoid supports a vertical pressure Q_1 which produces a horizontal compression q_1 in DDB and compression P_1 in the two legs of the trapezoid. In the vertical region DDCC below the plate, horizontal and vertical compressions Q_2 are arbitrarily added. The unilateral pressure Q_2 acting on face CD of the wedge CDH has the maximum safe value of (Chen, 1966):

$$Q_2 = c \cot \phi \left(\tan^2 \left(\frac{\pi}{4} + \phi/2 \right) \frac{\sin (\nu + \alpha_2)}{\sin (\nu - \alpha_2)} - 1 \right) \quad (17)$$

where $\cos \nu = \sin \phi \sin \alpha_2$

The same value was obtained earlier by Shield (16) through the application of the general jump condition. The inclination α_1 and stress p_1 are chosen so that the legs EBDF are plastic. The yield condition and the value of Q_2 give (Chen, 1966):

$$p_1 = \frac{4c(\sin \phi + \cos 2\alpha_1)}{\cos \phi (1 - \sin \phi)} \frac{\sin (\beta_2 - \mu_2)}{\sin (\beta_2 + \mu_2)} \quad (18)$$

and $\sin \alpha_1 = \cos \frac{\phi}{2}$

where $\sin \mu_2 = \sin \phi \sin \beta_2$

Q_1 is obtained by using the condition of equilibrium of forces, the condition of plastic yield in DDB, and values of p_1 and α_1 obtained above. The lower bound $Q_L = Q_1 + Q_2$ is given as (Chen, 1966):

$$Q_L = c \cot \phi \left\{ \tan^2 \left(\frac{\pi}{4} + \phi/2 \right) \frac{\sin (\beta_2 - \mu_2)}{\sin (\beta_2 + \mu_2)} - 1 \right\} + \frac{c}{2} \tan^3 \left(45 + \frac{\phi}{2} \right) \frac{\sin (\beta_2 - \mu_2)}{\sin (\beta_2 + \mu_2)} \quad (19)$$

$$\left\{ 4 + \sin \phi + \sin^2 \phi + (1 + \sin \phi) (4 + \sin^2 \phi)^{1/2} \right\}$$

γ) Solution for large bearing plates in expanding soils.

Due to the presence of the "no-stress" zones, it is assumed that two half spaces are formed. This assumption is more correct when the bearing plate angle 2β is close to 180° . For smaller bearing plates the boundary AD deviates from the direction perpendicular to the direction of loading. The failure surface is that of the Prandtl

mechanism (Fig. 11). The upper bound for $c - \phi$ medium is given by (Finn, 1965):

$$Q^u = c \cot \phi \left\{ e^{\pi \tan \phi} \tan^2 (45 + \phi/2) - 1 \right\} \quad (20)$$

The lower bound is given by equation (19) above with $\beta_2 = \frac{\pi}{2}$. The lower bound becomes (Chen, 1966):

$$Q_L = c \cot \phi \left\{ \tan^2 (45 + \phi/2) - 1 \right\} + \frac{c}{2} \tan^2 (45 + \phi/2) \left[4 + \sin \phi + \sin^2 \phi + (1 + \sin \phi) (4 + \sin^2 \phi)^{1/2} \right] \quad (21)$$

For smaller bearing plate widths, the upper bound and lower bound are smaller than those calculated by equation (19) and (20), because the surfaces of the half spaces are sloping.

δ) Borehole jack loading in contracting soils. A few laboratory tests conducted in this research project on sand-mica-paraffin mixtures suggest that contracting soils (relatively loose sands and soft clays), under jack loading, fail by forming a plastic bulb below the plate. The plastic bulb exerts pressure on the outside elastic mass. A solution by Vesic and Barksdale (1963) for an expanding cylindrical cavity in $c - \phi$ material applies here when the plastic bulb is approximated by half of a circular ring as shown in Fig. 12. The load against the bearing plate is replaced by the internal pressure p_{ult} against the wall of a cavity of radius equal to the width of the bearing plate. Assume that the total force against the cavity wall in

the direction of jacking is equal to the ultimate load p_{ult} :

$$p_{ult} = q_{ult}$$

q_{ult} = average ultimate pressure against bearing plates, equal to p_{ult} / plate width.

$$p_{ult} = cF_c + qF_q \quad (14)$$

q = initial ambient isotropic pressure. The cavity expansion factors F_c and F_q are functions of cohesion, friction, modulus of elasticity, Poisson's ratio, and ambient pressure.

Further literature studies are in progress as is an experimental program to define the actual failure modes in all cases and to check the validity of the proposed mechanisms and their solution.

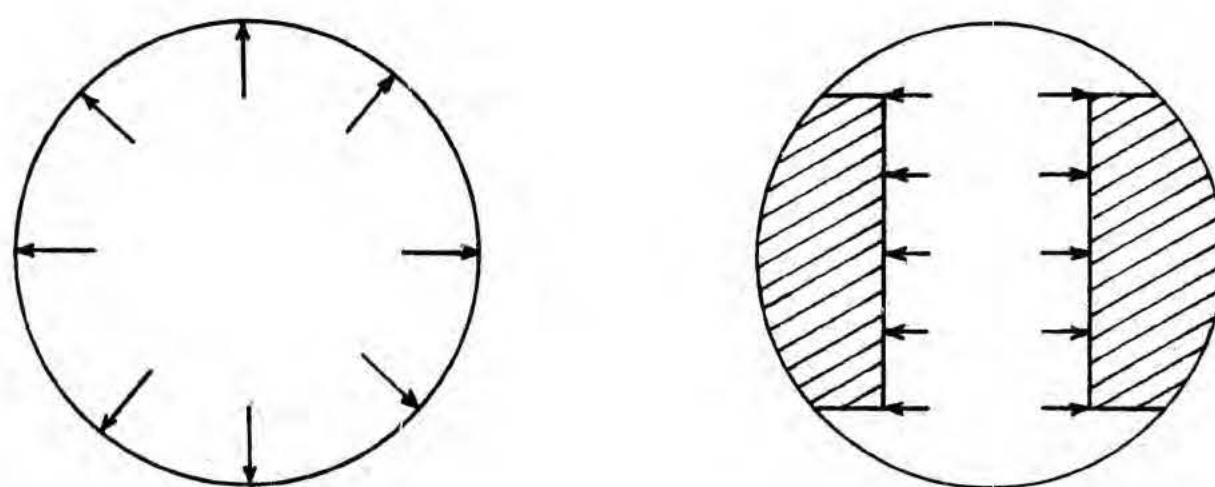
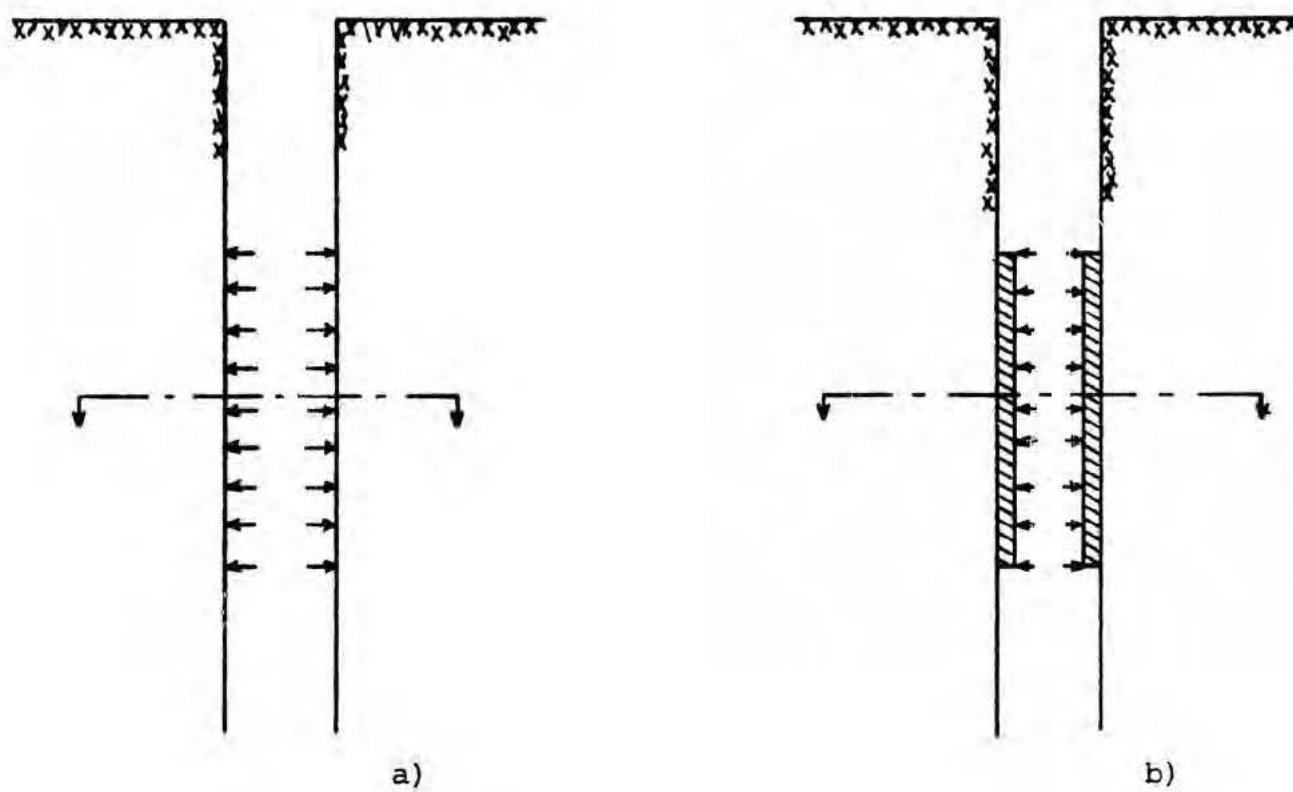


FIGURE 1. a) Dilatometer loading
b) Borehole jack loading

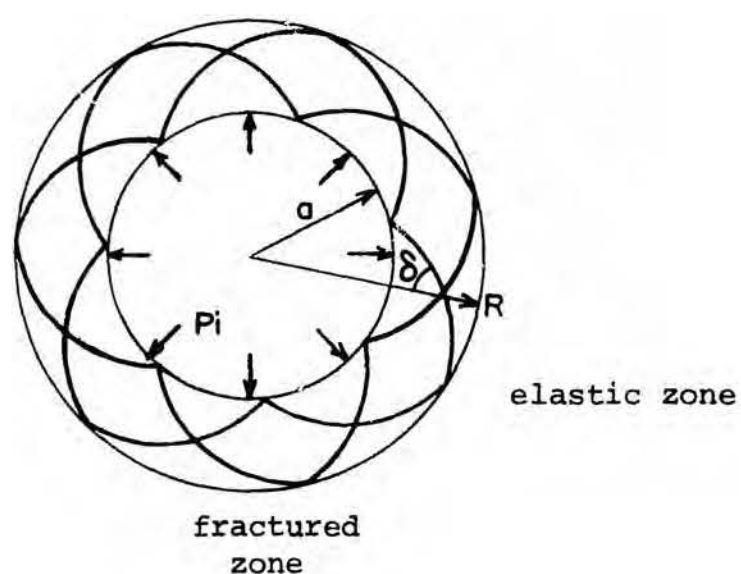


FIGURE 2. Logarithmic spiral fracture zone around circular hole under dilatometer loading (after Bray, 1967).

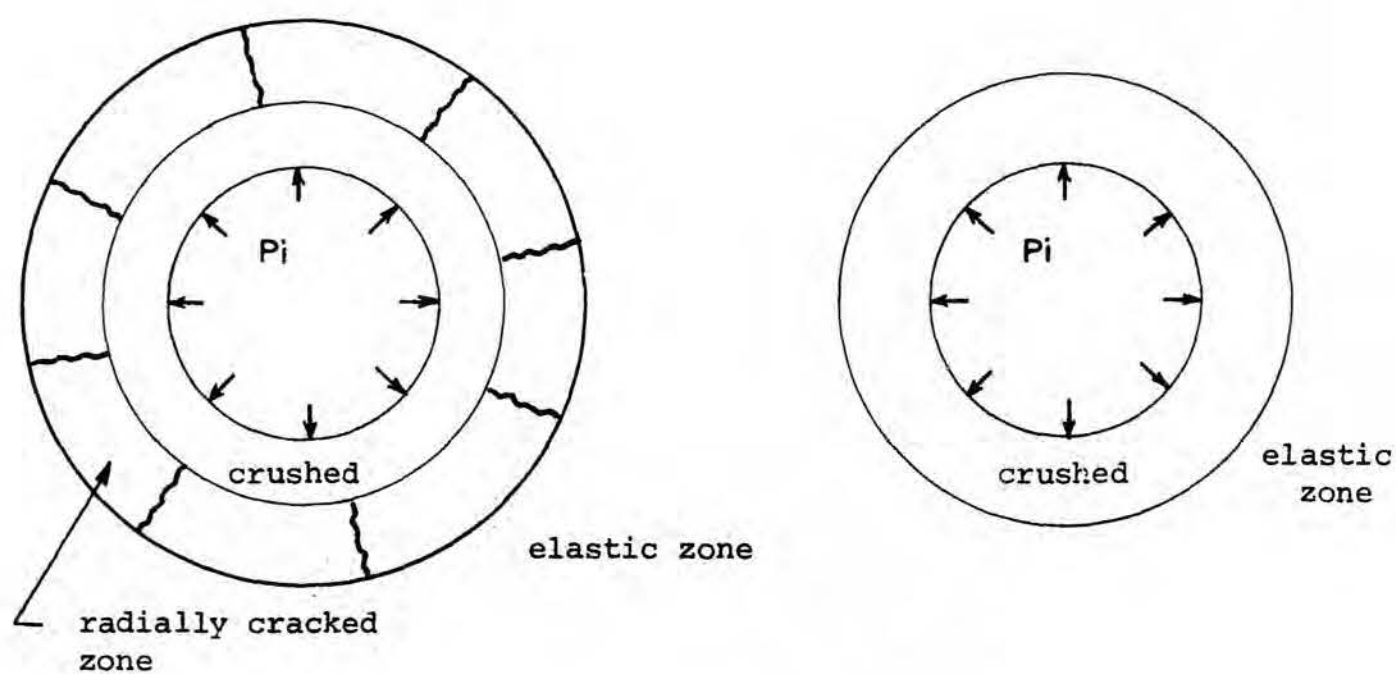


FIGURE 3. Rock failure around a cylindrical cavity (after Ladanyi, 1967).

$$a) \quad \left(\frac{p_0}{-T_s} \right) < \frac{m(m-2)-1}{2}$$

$$b) \quad \left(\frac{p_0}{-T_s} \right) \geq \frac{m(m-2)-1}{2}$$

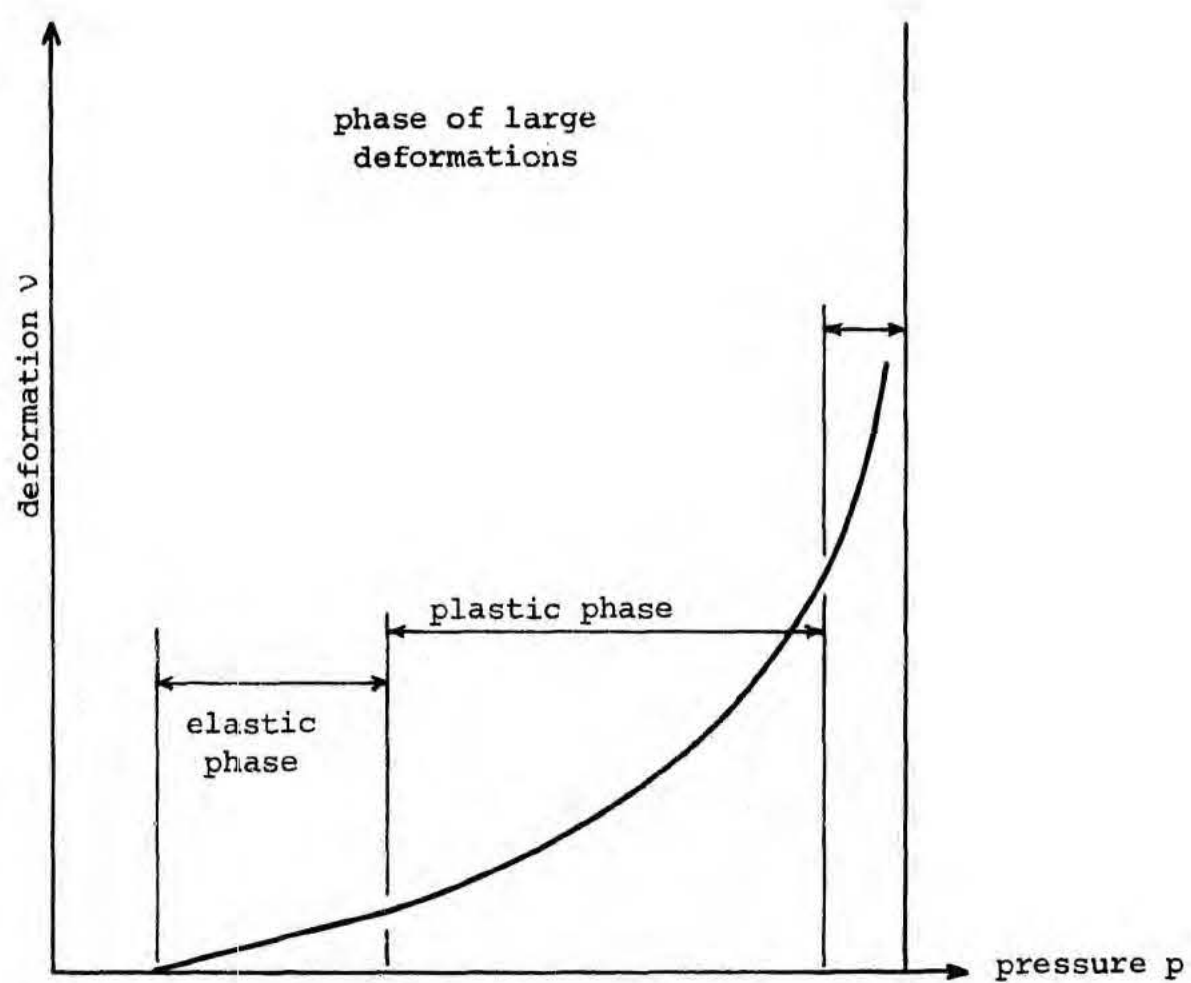


FIGURE 4. Deformation-pressure relationship for dilatometers in soils (after Menard, 1957).

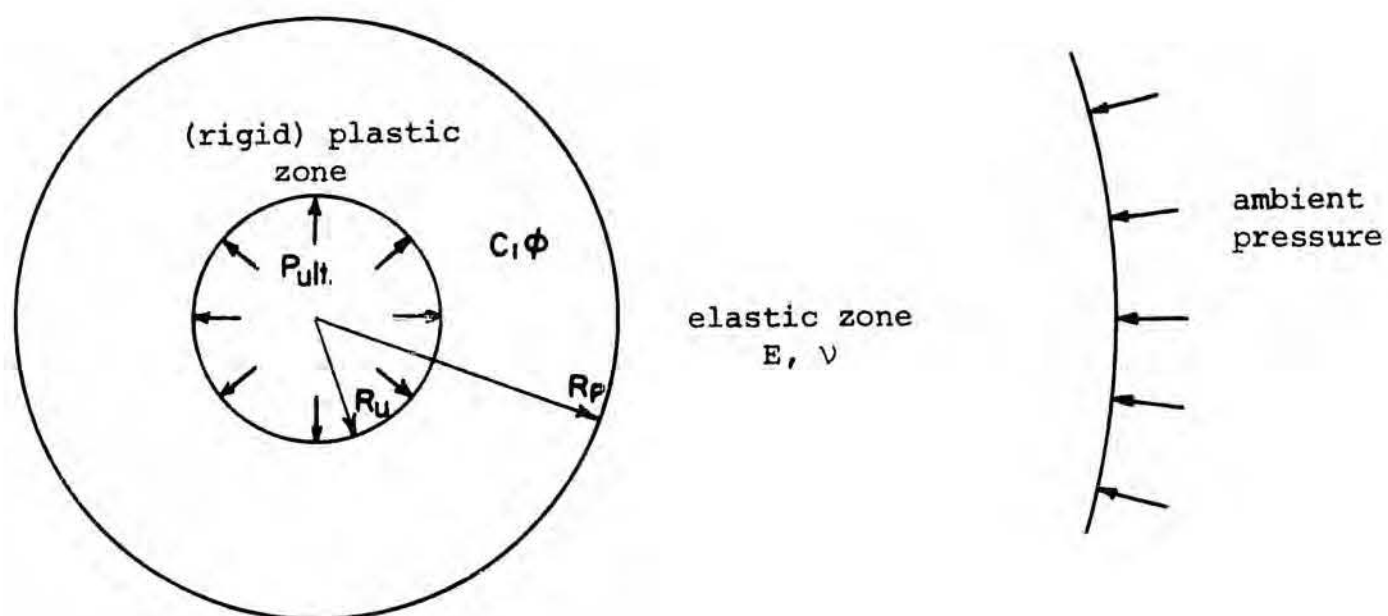


FIGURE 5. Expansion of a cylindrical cavity in a $c - \phi$ material (after Ladanyi, 1967).

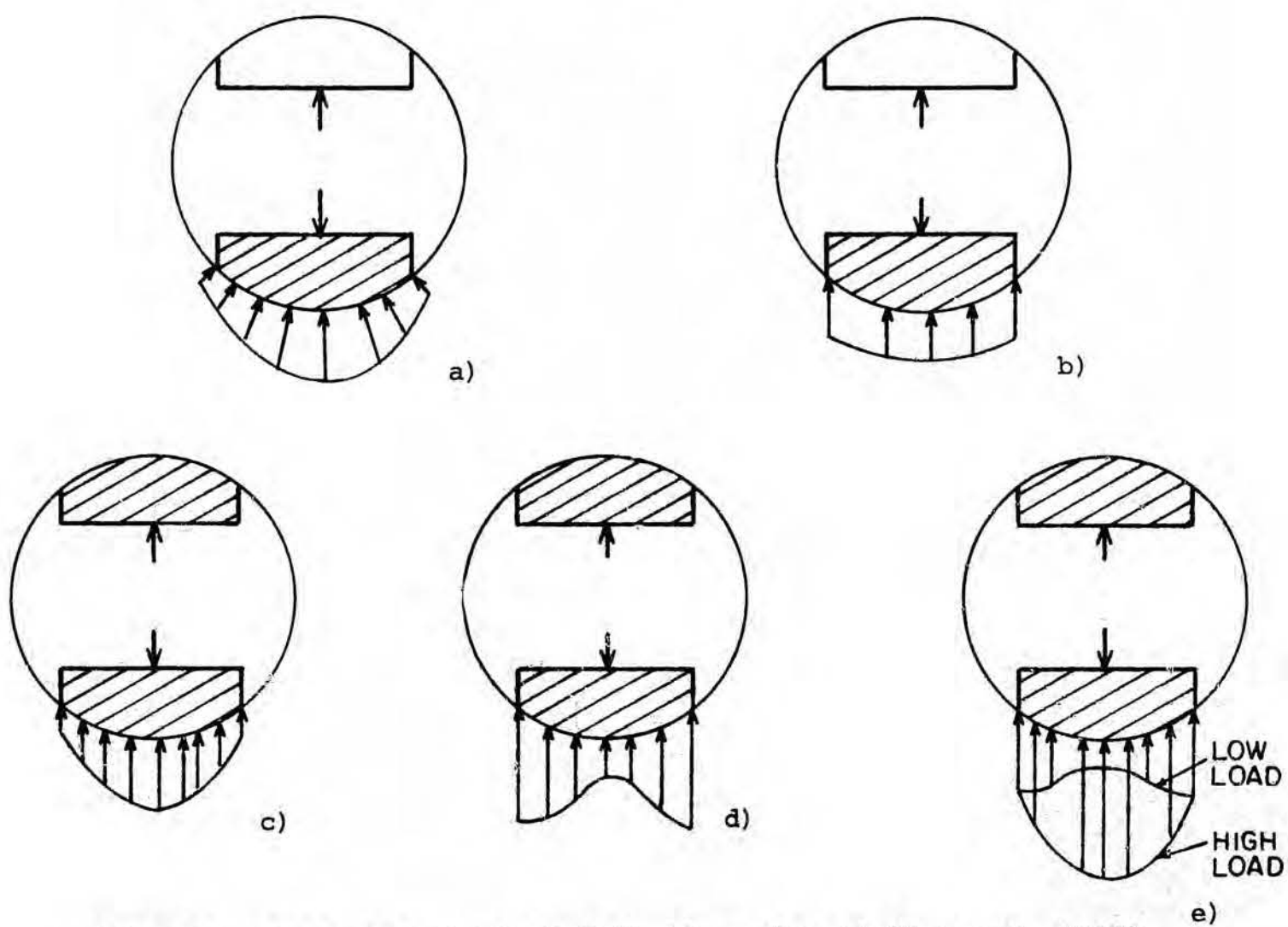


FIGURE 6. Contact pressure distribution a) rock (Wyanecki, 1968) b) rock (Goodman et al., 1968) c) sand d) clay e) $c - \phi$ soil.

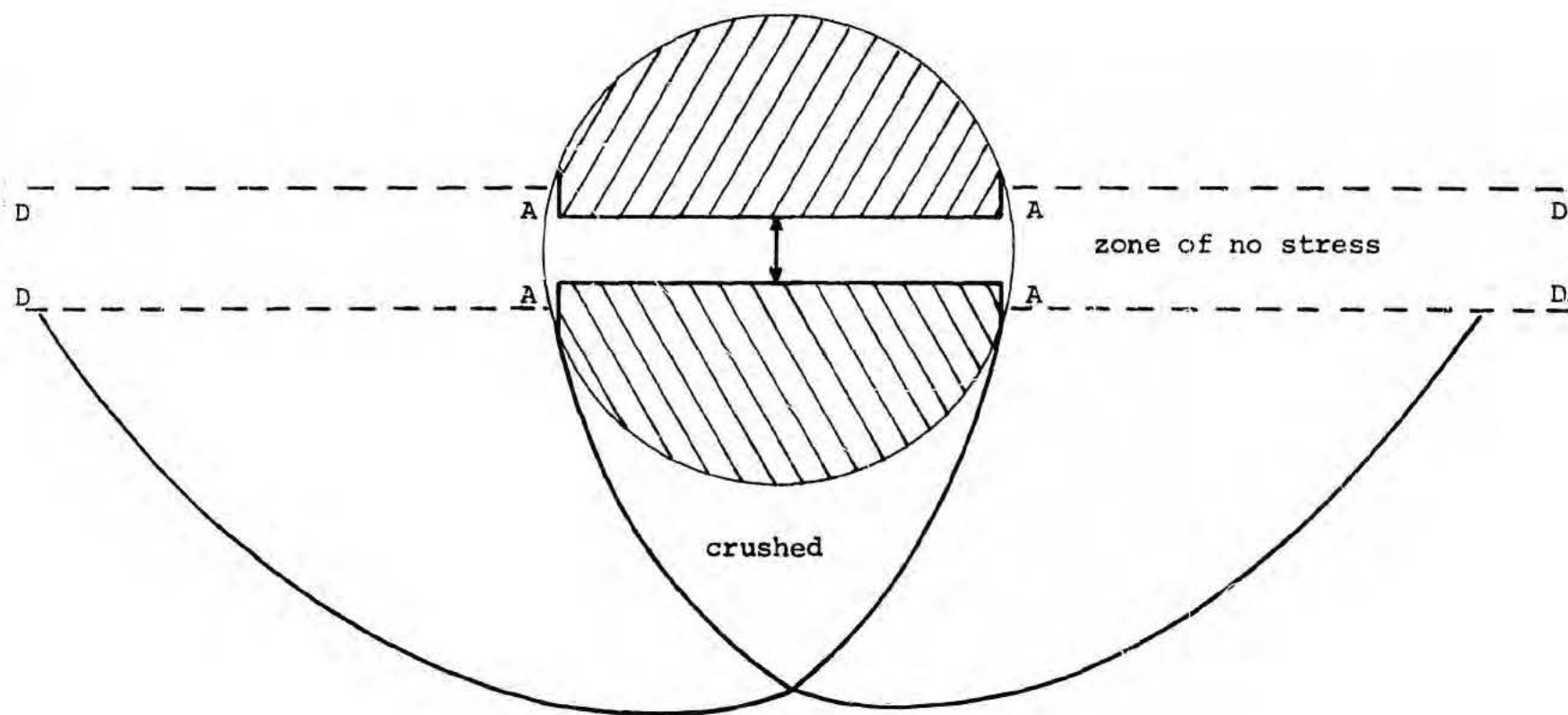
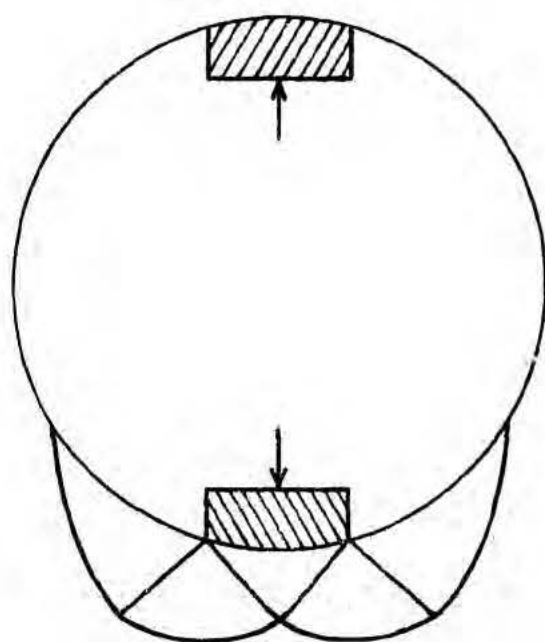
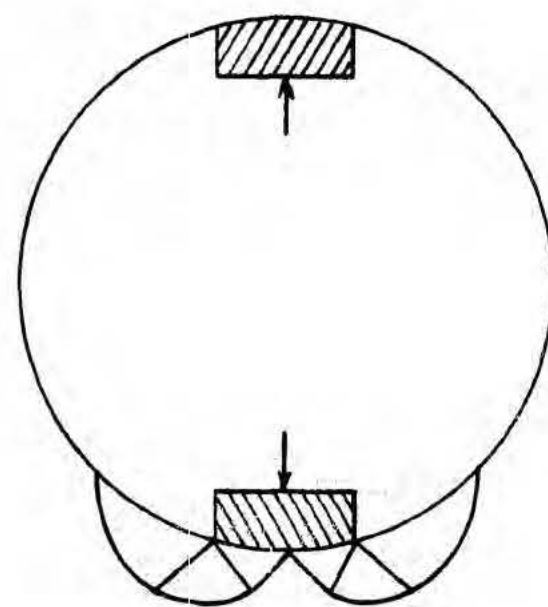


FIGURE 7. Failure for large bearing plate.



a) Prandtl mechanism



b) Hill mechanism

FIGURE 8. Mechanism of failure for small plates in expanding soils.

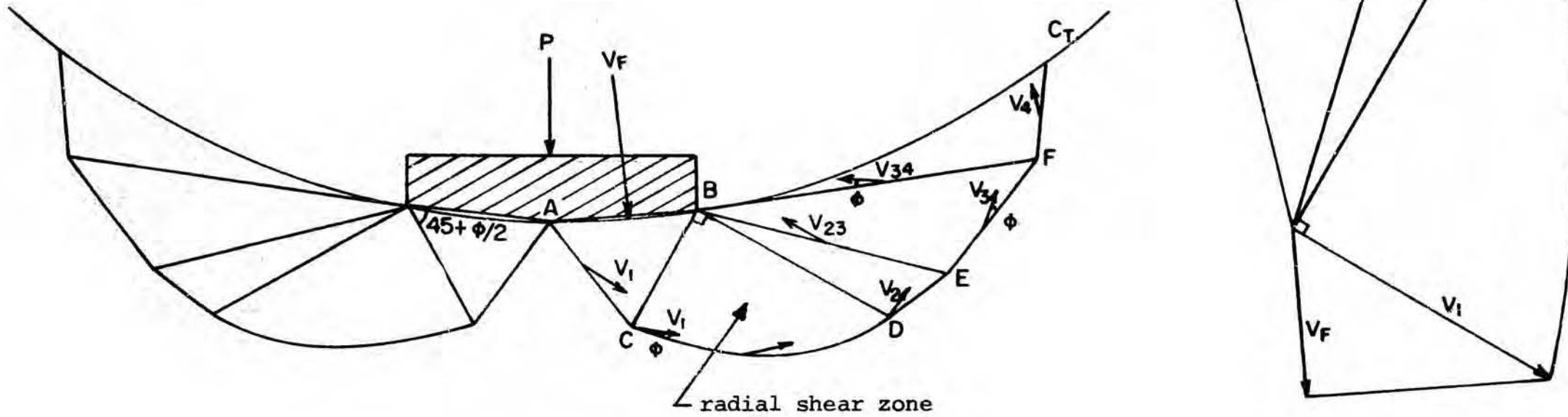


FIGURE 9. Upper bound solution. Velocity field by hodograph.
Hill mechanism for small bearing plates on plastic materials.

LOWER BOUND (APPROXIMATION)

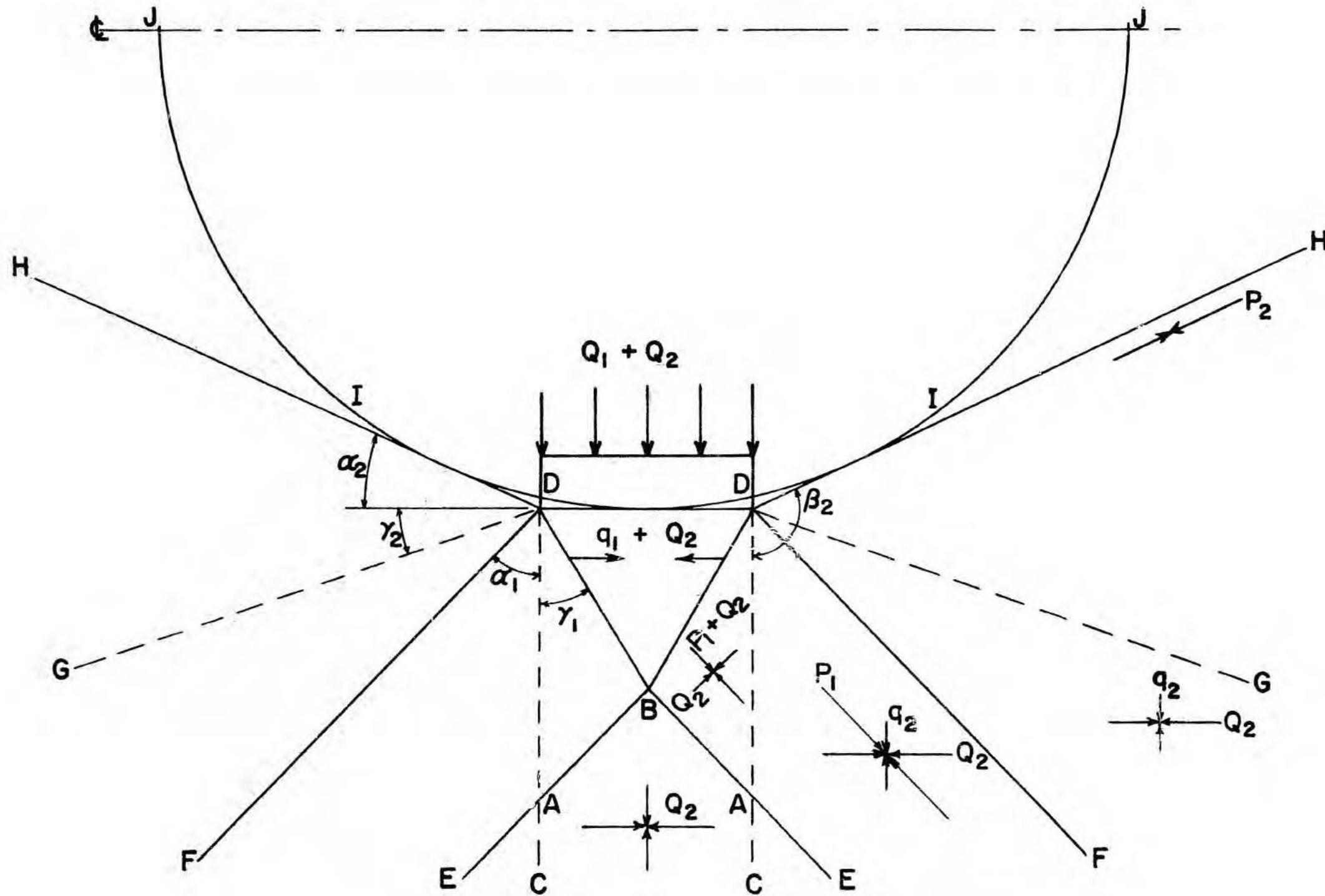


FIGURE 10. Lower bound solution for small bearing plates on plastic materials (after Wai-Fah Chen, 1966).

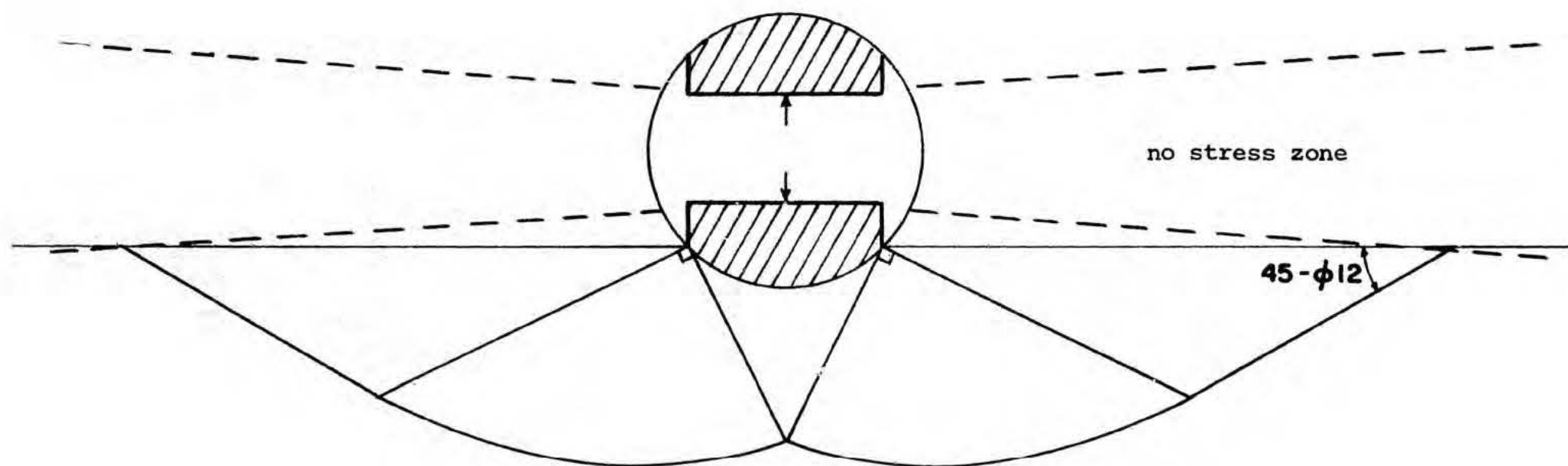


FIGURE 11. Failure mechanism for large bearing plate in expanding soil

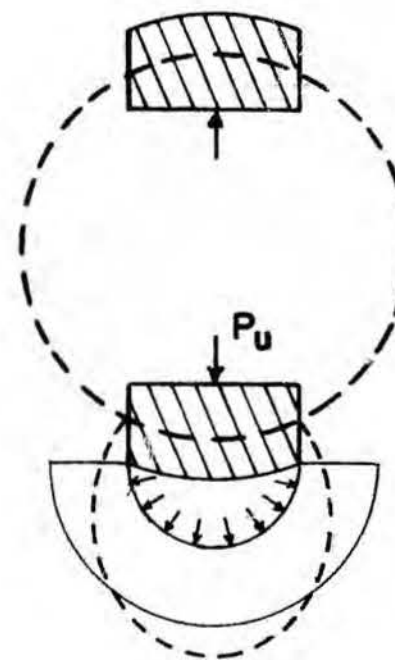
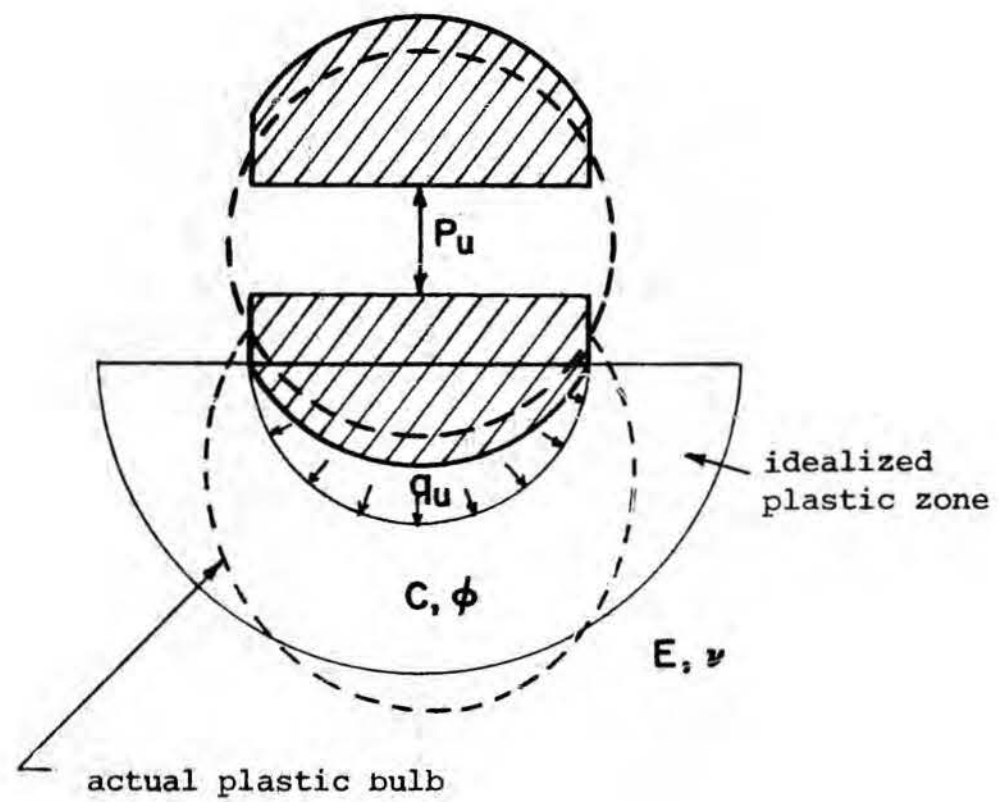


FIGURE 12. Mechanism of failure in contracting soils

SOURCES OF REFERENCE

1. Bishop, R. F., Hill, R., and Mott, N. F., "The Theory of Indentation and Hardness Tests", Proceedings of the Physical Society, London, 57/3, pp. 147-159, 1945.
2. Bray, J. W., "A Study of Jointed and Fractured Rocks, Part II, Theory of Limiting Equilibrium", Rock Mech. and Engineering Geology, Vol. 4, 1967.
3. Chen, W. F., "On Solving Plasticity Problems of Relevance to Soil Mechanics. The Bearing Capacity of Concrete". Ph.D. Thesis Brown University, 1966.
4. Fairhurst, C., "On the Validity of the Brazilian Test for Brittle Materials", Int. Journal of Rock Mechanics & Mining Sciences, 1, pp. 535-546, 1964.
5. Finn, W. D. L., "Application of Plasticity in Soil Mechanics". Soil Mechanics and Bituminous Materials Research Laboratory, Univ. of California, Berkeley, August 1965.
6. Gibson, R. E., and Anderson, W. F., "In-situ Measurement of Soil Properties with the Pressuremeter." Civil Engineering & Public Works Review 56, pp. 615-618, 1961.
7. Goodman, R. E., Van, T. K., and Heuzé, F., "The Measurement of Rock Deformability in Boreholes." Proceedings of the 10th Symposium on Rock Mechanics, AIME, 1968.
8. Goodman, R. E., "Effects of Joints on the Strength of Tunnels, Analysis of Piledriver Drifts." Report of Investigation for U.S. Army Engineer District, Omaha, August 1968.
9. Hill, R., "The Mathematical Theory of Plasticity." Oxford University Press. 1951.
10. Kérisel, J., "La Mécanique des Sols: recherches et investigations récentes." Travaux 42, pp. 874-878, 1968.
11. Ladanyi, B., "Expansion of a Cavity in Saturated Clay Medium"; Proceedings ASCE, Journal of Soil Mechanics and Foundation Division, 89, No. SM-4, pp. 127-161, 1963.
12. _____, "Expansion of Cavities in Brittle Media", Intern. Journal of Rock Mechanics & Mining Sciences, Vol. 4, pp. 301-328, 1967.
13. _____, "Rock Failure under Concentrated Loading", Proceedings of the 10th Symposium on Rock Mechanics, Texas, 1968.
14. Menard, L., "Mesures In-situ des Propriétés Physiques des Sols." Annales des Ponts et Chaussées, 127, pp. 357-377, 1957.

15. Seeley, F. B., and Smith, J. O., "Advanced Mechanics of Materials." John Wiley and Sons, Inc., pp. 295-341, New York, 1959.
16. Shield, R. T., "Stress and Velocity Field in Soil Mechanics", Journal of Mathematical Physics, Vol. 33, No. 2, pp. 144-156, 1954.
17. Skempton, A. W., Yassin, A. A., and Gibson, R. E., "Théorie de la Force Portante des Pieux dans le Sable", Annales de l'Inst. Tech. Bâtiment, No. 63-64, p. 285, 1953.
18. Vesic, A. B., and Barksdale, R. D., "Theoretical Studies of Cratering Mechanisms Affecting the Stability of Cratered Slopes." Project No. A-655, Eng. Exper. Station, Georgia Inst. of Tech., 1963.
19. Wyanecki, J., "Les Géoextensomètres du Centre Expérimental de Recherches et d'Etudes du Bâtiment et des Travaux Publics, Etude Expérimentale sur Modèles Réduits." Laboratoire du Bâtiment et Travaux Publics, Supplément aux Annales, No. 246, June 1968.

APPENDIX — DETAILED DESCRIPTION OF MODEL STUDIES

(K. Drozd, T. K. Van, R. E. Goodman)

During the period October 1 to December 31, 1968 research proceeded in the following domains:

- (1) Theoretical determination of the mode of failure taking place, when a hole in a rock or soil material is uniaxially loaded by opposed bearing plates.
- (2) Model testing to guide and check the theoretical solutions.

The theoretical work (1) was described in the body of the quarterly report. This appendix describes details of the testing program (2) conducted during the quarter. The results of these tests will be presented in the final report of the project.

The research of the fourth quarter of 1968 continued model studies begun during the summer, in which the following equipment was used:

- (1) Uniaxial jack for tests in a circular hole 3" in diameter and 1-1/2" deep, equipped with pairs of bearing plates of 4 different dimensions. The jack was fitted with a complete hydraulic device (hydraulic oil pump and lines, manometer for pressures up to 4000 psi).
- (2) Four model plates made of the following mixture (by weight):

plaster	1.0
celite	0.4
water	1.6
retarder	0.002

The plates were 36" × 36", 1-1/2" thick, and with a central hole 3" in diameter.

- (3) Testing bench with base steel plate and upper plexiglass plate with screws for achieving plain strain condition on the tested plate.

During the conduct of the model tests it became necessary to modify some of the procedures as the results became available. The modifications were of four types:

- A) Adjustment of the model jack to include a load cell
- B) Development of new model materials and improved fabrication techniques
- C) Determination of a convenient method for deformation measurements
- D) Preparation of new devices for further model explorations

A. Modification and Adjustment of the Model Jack

During calibration studies the hydraulic pressure measuring system displayed intolerable hysteresis. Therefore a strain gauge dynamometer was constructed. The dynamometer is a steel ring fitted between the hydraulic cylinder and one bearing plate. It has a sensitivity of 1 micro strain per 2.65 pounds, constantly and reproducibly throughout the entire 4000 psi range.

B. Adjustment of Model Plates

The model plates made of plaster and celite were cast in a special form in vertical position. Even if both casting plates were stiffened by frames, the pressure of liquid mixture caused a small deflection of plates, especially in the center part, in the place of the central hole.

The deflection amounted to $3/16$ " over the standard thickness of $1-1/2$ ". This deflection caused a breaking of one plate during the Test 2 when the model plate, inserted between steel and plexiglass plate was loaded by screwing the periphery bolts. We tried to eliminate this deflection by inserting some thin layers of papers under the model plate. This arrangement proved to be sufficient but influenced the deformation in the environment of the loaded bearing plates owing to the high friction between both units. It was shown that the next model plates should be cast in a horizontal position directly on the model table.

At the end of the quarter we tried casting a model plate from a mixture of sand and parafin. The sand was clean and poorly graded in the range 0.5 - 1.0 mm (Monterey Sand No. 20). The two components were mixed hot in a ratio 25:1 (sand:parafin). At the end of the quarter the characteristic values (ϕ , c , E_0) were not yet available. The unit weight obtained from three separately made samples was 1.67, 1.61, and 1.73 g/cm^3 .

C. Improvement of Deformation Measurements

Plate displacements were measured with a dial gauge. Owing to the small thickness of the testing plate, it was not possible to guarantee parallel movement of both bearing plates. Also a small force in the spring of the dial gauge indicator increased the deformations during the decreasing of load so that the modulus of elasticity of the tested plate could not be determined. Improvements were made to remedy these deficiencies. Several methods were used to measure borehole deformation.

1) The tested area was covered by a brittle coating. This method failed totally because: a) the coating penetrated the model and changed its properties; b) the surface of the model plates was insufficiently smooth; and c) the modulus of elasticity of the plates was too high.

2) The Moiré Method of Strain Analysis was used. This method proved to be quite reliable when plaster-celite plates were used but proved inapplicable for plates made of sand-parafin mixture.

3) For parafin-sand plates, regular patterns were created on the surface of the plates using a mica powder which was sifted over the surface through a grid of holes. Photogrammetric techniques of recording and measuring the deformation of grid points were developed.

D. Preparation of New Devices for Further Model Explorations

The model tests will continue with other materials of varying properties. Models during this quarter failed either by a tension cracking, without any visible changes around the hole (plaster-celite plates) or by a local punching of the bearing plates (sand and parafin mixture). Dilatent materials are being prepared to study shear modes of failure. It is planned to perform tests as well with simulated lunar soils. The temporary stability of the hole wall will be created by placing the model under vacuum inside a closed steel frame.

Arrangements started for making a small dilatometer to study failure modes under this loading configuration as well. A cast was made for molding the rubber coat of a special polymer. (Adiprene-Liquid Urethane Elastomer hardened by Moca).

VI. STUDIES ON FLUID CONDUCTIVITY OF LUNAR SURFACE MATERIALS

(D. F. Katz, D. R. Willis, P. A. Witherspoon)

1. INTRODUCTION

In the first quarterly report, the problems in developing a means of measuring permeability of lunar rocks and soils in situ, using a gas, were introduced. The design of a lunar permeability probe is dependent upon a knowledge of the equations of motion for a gas flowing through porous media under lunar conditions. Because of the lack of any atmosphere on the moon, the specific nature of these equations is not well understood. Thus, it was first necessary to develop the fundamental physics of gaseous flow in lunar soils and rocks.

During the second quarter, theoretical analysis of the physics was continued. As a result of the physics developed to date, a general form of the equations governing flow of gases in lunar soils and rocks has been deduced. On the basis of only this general form, a simple method has been developed for measuring lunar permeabilities in situ. The method utilizes an assumption of local similarity and provides a basis for the first experimental approach to the problem.

2. LOCAL SIMILARITY ANALYSIS OF FLOW IN POROUS MEDIA

In the first quarterly report, a general qualitative momentum relationship was described

$$\underline{v} = C(p) \nabla p \quad (1)$$

where \underline{v} is the average fluid velocity vector in a pore (see Appendix I), p is the average pressure, and C is a master diffusion coefficient. Consider a steady, isothermal flow field dependent upon only one space variable, denoted by r , i.e. a one-dimensional, cylindrically symmetric, or spherically symmetric problem. Henceforth, such flow problems will be referred to as "symmetric." Then Eq. (1) becomes

$$v = C(p) \frac{dp}{dr} \quad (2)$$

$C(p)$ can be rendered dimensionless by defining

$$C(p) \equiv \frac{L^2}{\mu} \tilde{C}(p) \quad (3)$$

where μ is viscosity, \tilde{C} is the dimensionless form of C , and L is an effective cross-sectional dimension of a pore, the square of which is termed the permeability, k .

$$L^2 \equiv k \quad (4)$$

It is assumed that \tilde{C} is a function of local pressure (or Knudsen number)^{*} only, as in the Wakao formula described in the first report. This is the basic local similarity assumption. As applied to Eq. (2), it embodies all the necessary physics of the flow field. The specific form of \tilde{C} need not be known.

^{*} Pressure and Knudsen number are inversely proportional. See Appendix B.

Consider now the continuity equation [see Appendix A]

$$\alpha \rho v r^j = \hat{Q} \quad (5)$$

where α is the area fraction, ρ the average density, and \hat{Q} takes on different values, as shown in Table 1, depending upon the nature of the symmetric problem.

TABLE 1

Symbol	Type Symmetric Problem		
	One-Dimensional	Cylindrical	Spherical
j	0	1	2
\hat{Q}	Q/A	$Q/2\pi\ell$	$Q/4\pi$

Here Q refers to the dimensional mass flow rate, A is the total cross-sectional area of the rock in one-dimensional flow, and ℓ is the cylinder length for cylindrically symmetric flow. Combining Eqs. (2), (3), and (5),

$$\hat{Q} = \alpha \frac{L^2}{\mu} \rho r^j \tilde{C}(p) \frac{dp}{dr} \quad (6)$$

Assume that the gas is perfect, so that $p = \rho RT$, where R is the gas constant and T is average temperature. Then

$$\hat{Q} = \alpha \frac{L^2}{\mu RT} r^j p \tilde{C}(p) \frac{dp}{dr} \quad (7)$$

Now, $\hat{C}(p)$ is dimensionless; hence it can be expressed as a function of a dimensionless pressure ζ :

$$\hat{C}(p) \equiv \frac{1}{F(\zeta)} \quad (8)$$

The particular form of ζ is motivated by the fact that \hat{C} can be considered a function of Knudsen number only (see Appendix II). Thus

$$\zeta \equiv \frac{\bar{L}\bar{V}}{2\mu RT} p = \frac{1}{Kn} \quad (9)$$

where $\bar{V} = \sqrt{\frac{8RT}{\pi}}$, the mean thermal speed, and Kn is the Knudsen number.

Substituting in Eq. (7) and rearranging,

$$\alpha L^2 \frac{1}{2\mu RT} r^j p \frac{dp}{dr} = F(\zeta) \quad (10)$$

This is a fundamental similarity relation. $F(\zeta)$ is a "universal" function, in that data from all symmetric problems, plotted according to Eq. (10), fall on the same curve. It should be noted that $F(\zeta)$ is not the only possible universal curve. Multiplication by any real function of ζ yields an equally universal curve.

3. METHOD FOR DETERMINING PERMEABILITY AND AREA FRACTION

By developing dimensionless relationships in this manner, Eq. (10) can be used to determine both permeability, L^2 , and the area fraction, α . For example, if the flow field for the lunar probe can be approximated as

spherically symmetric, as has been found by Selim et al.¹ for a related problem, then $j = 2$ and $\hat{Q} = Q/4\pi$. Equation (10) becomes

$$\alpha L^2 \left(\frac{4\pi}{Q\mu RT} r^2 p \frac{dp}{dr} \right) = F(\zeta) \quad (11)$$

Since $F(\zeta)$ presumably holds for any symmetric flow in porous media, this function can be uniquely determined by appropriate experimentation in the laboratory.

To apply Eq. (11) to an unknown rock sample, one must fix the flow rate Q and measure temperature T , from which $\mu = \mu(T)$ is easily determined. If pressure taps are appropriately spaced in the skirt of the probe (cf. Fig. 1 of first quarterly report), then $r^2 p \frac{dp}{dr}$ can be measured at two or more different values of r . This enables one to determine two different values of the bracketed expression in Eq. (11), which are sufficient to determine both L and α .

A simple procedure illustrating the method of calculation can be outlined as follows. From Eqs. (9) and (11)

$$\ln \zeta = \ln p + \ln \left(\frac{\bar{V}}{2\mu RT} L \right) \quad (12a)$$

$$\ln F(\zeta) = \ln \left(r^2 p \frac{dp}{dr} \right) + \ln \left(\alpha L^2 \frac{4\pi}{Q\mu RT} \right) \quad (12b)$$

$$\frac{d \ln F(\zeta)}{d \ln \zeta} = \frac{d \ln \left(r^2 p \frac{dp}{dr} \right)}{d \ln p} \quad (12c)$$

It follows that curves of $F(\zeta)$ vs ζ and $r^2 p \frac{dp}{dr}$ vs p , plotted on identical log-log scales, differ only in the positions of their respective origins of coordinates. Thus, the two measured values of $r^2 p \frac{dp}{dr}$ are plotted versus

p on log-log paper, and $F(\zeta)$ vs ζ is plotted on identical paper. The two plots are then placed on top of each other, and maneuvered, keeping respective axes mutually parallel, until the two experimental points lie on the known curve. The coordinates of the origin of the experimental plot relative to the universal one then clearly yield both α and L . See Fig. (1).

As drawn in Fig. (1), $F(\zeta)$ will be a monotonic function of ζ . However, a problem of uniqueness in determining α and L will arise if there are regions where, on the log-log scale, $F(\zeta)$ is locally linear. If the experimental points correspond to such regions, then the position of the origin of the experimental plot is not uniquely determined. This difficulty can, in principle, be circumvented, however, by redefinition of the universal curve such that it has adequate curvature throughout.

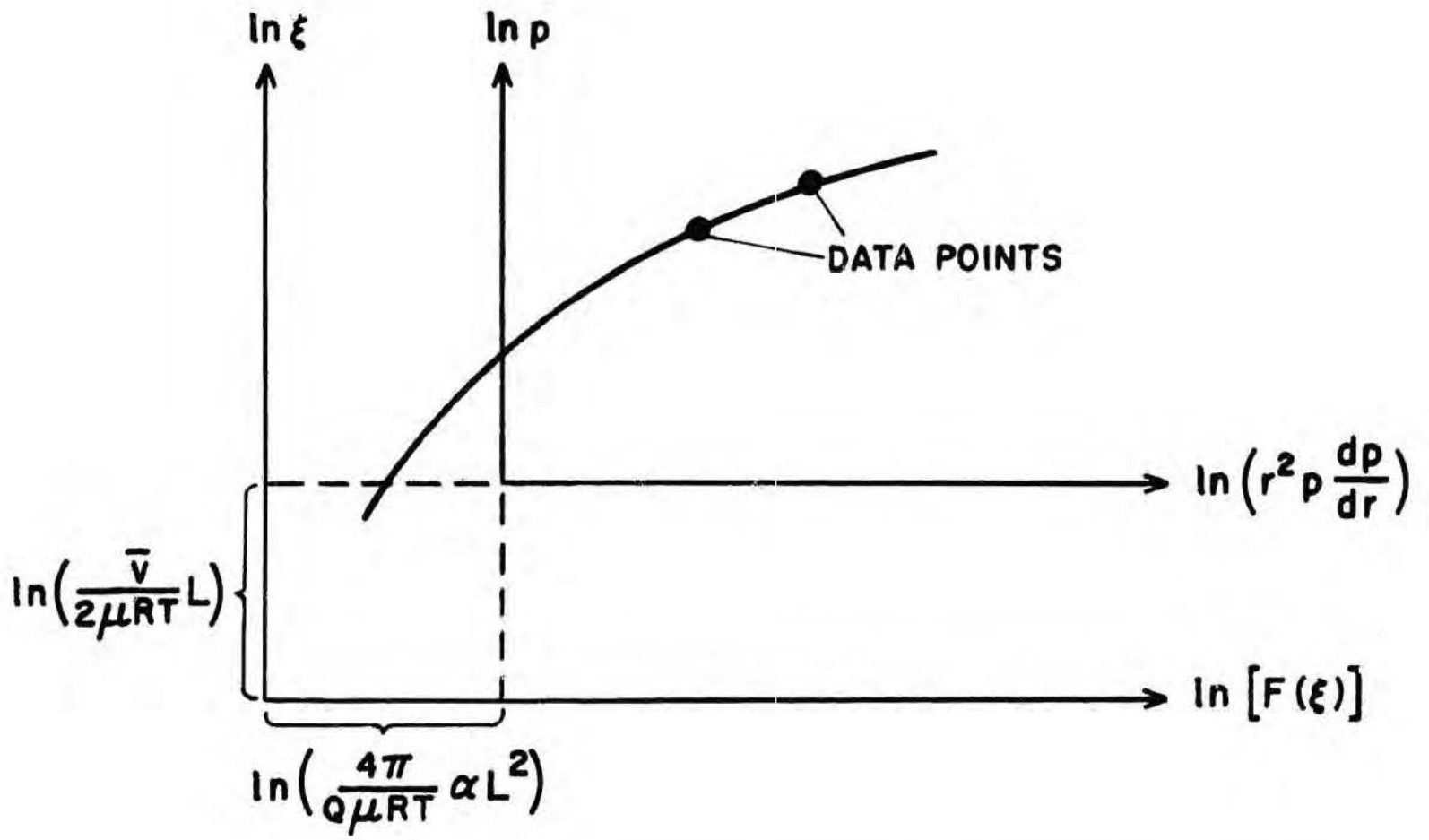


FIGURE 1. Example of matching procedure in determining permeability and area fraction

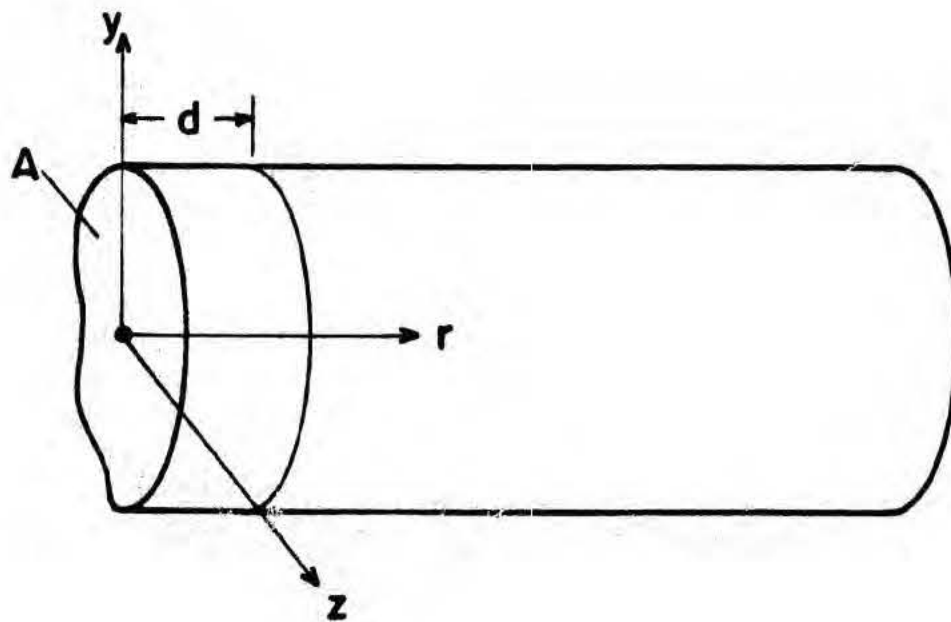


FIGURE 2

REFERENCES

¹Selium, M. A., I. Fatt, and W. H. Somerton, "Temperature Rise in a Semi-Infinite Medium Heated by a Disc Source. Proc. Konkl. Ned. Acad. Wet., Amsterdam, A, 66, 5 (November, 1963), pp. 705-720.

²Carman, P. C., Flow of Gases Through Porous Media, Academic Press, New York (1956), pp. 8 and 30.

APPENDIX A

In Eq. (5), the area fraction α is defined

$$\alpha \equiv \frac{\bar{A}_p}{\hat{A}} \quad (\text{I-1})$$

where

$$\bar{A}_p \equiv d^{j-1} \int_{d_0}^d r^{-j} A_p(r) dr \quad (\text{I-2})$$

$$\hat{A} \equiv \begin{cases} A & \text{-- one dimensional} \\ 2\pi d l & \text{-- cylindrical symmetry} \\ 4\pi d^2 & \text{-- spherical symmetry} \end{cases} \quad (\text{I-3})$$

Here d is a reference length large compared to a typical pore length, d_0 is the diameter of the fluid source (taken to be zero for one-dimensional flow), and $A_p(r)$ is the total pore area normal to the flow. Thus \bar{A}_p represents the pore area, normal to flow, averaged along d ; and \hat{A} is the total cross-sectional area of the porous medium at $r = d$. The significance of these quantities will be illustrated for the case of one dimensional flow. Similar descriptions apply to flows with cylindrical or spherical symmetry.

Consider a one dimensional flow through a hollow cylinder of cross-section A , cf. Fig. (2). A Cartesian coordinate system r, y, z is fixed in the cylinder. The "average" velocity and density at any station r are defined, respectively

$$\bar{v}(r) \equiv \frac{1}{A} \int \int_A v(r, y, z) dy dz \quad (I-4)$$

$$\bar{\rho}(r) \equiv \frac{1}{A} \int \int_A \rho(r, y, z) dy dz \quad (I-5)$$

The applied mass flow rate Q is given by

$$Q = \int \int_A \rho(r, y, z) v(r, y, z) dy dz = \text{constant} \quad (I-6a)$$

$$\equiv \bar{\rho v} A \quad (I-6b)$$

$\bar{\rho v}$ represents the average mass flow rate per unit area, and is constant.

Suppose now that the cylinder is filled with a porous material.

$A_p(r)$ here represents the total pore area projected on a $y - z$ plane, and \hat{A}_p is thus the total pore area on an average $y - z$ plane.* Now

$$Q = \int \int_{A_p(r)} \rho(r, y, z) v(r, y, z) dy dz = \text{constant} \quad (I-7a)$$

$$\equiv \bar{\rho v}(r) \hat{A}_p(r) \quad (I-7b)$$

The average velocity and density in a pore are defined

$$\bar{v}(r) \equiv \frac{1}{\hat{A}_p(r)} \int \int_{A_p(r)} v(r, y, z) dy dz \quad (I-8)$$

* That is, \hat{A}_p is the average of $A_p(r)$ along the length d on the rock sample, where d is large compared to a typical pore length so that a large number of different pore cross-sections are included.

$$\bar{\rho}(r) \equiv \frac{1}{A_p(r)} \int_{A_p(r)} \rho(r,y,z) dy dz \quad (I-9)$$

Written without the bars, these are the quantities which appear throughout this report. Similar definitions apply to average pressure and temperature.

Thus far, the continuity equation, cf. Eqs. (I-6b) and (I-7b), contains only the product $\bar{\rho}\bar{v}$, and is therefore insufficient to be applicable to the momentum equation, cf. Eq. (2), since no distinction is made between density and velocity.* In order to perform the necessary separation, some kind of statistical postulate is needed. It is therefore assumed that

$$\bar{\rho}(r)\bar{v}(r)\tilde{A}_p = \bar{\rho}\bar{v}(r)\tilde{A}_p(r) \quad (I-10)$$

Since Eq. (I-10) must apply to both compressible and incompressible flow, it is thus required that $\tilde{A}_p(r) = \tilde{A}_p = \text{constant}$. This has been verified experimentally for unconsolidated materials.² For consolidated materials, this assumption is valid for one-dimensional flow; however, for cylindrically and spherically symmetric flow, it may not hold due to the effects of anisotropy. It follows that

$$\bar{\rho}\bar{v}(r) = \bar{\rho}(r)\bar{v}(r) \quad (I-11)$$

Then, from Eq. (II-7b)

$$\bar{\rho}(r)\bar{v}(r)\tilde{A}_p = Q \quad (I-12)$$

* For incompressible flow, this problem does not arise, and the average velocity is simply the volumetric flow rate per unit pore area normal to the flow.

Hence, using Eq. (II-1),

$$\begin{aligned}\alpha \bar{\rho}(r) \bar{v}(r) &= \frac{Q}{A} \\ &= \hat{Q}\end{aligned}\tag{I-13}$$

This is the continuity equation for one-dimensional flow in porous media.
For a general symmetric flow

$$\alpha \bar{\rho}(r) \bar{v}(r) r^j = \hat{Q}\tag{I-14}$$

APPENDIX B^{*}

From the kinetic theory of gases,

$$\mu = \frac{1}{2} c \lambda \rho \bar{V} \quad (\text{II-1})$$

where c is a dimensionless constant of order one, and λ is the mean free path. Invoking the perfect gas law, taking $c = 1$, and rearranging Eq. (I-1),

$$\lambda = \frac{2\mu RT}{\bar{V}} \frac{1}{p} \quad (\text{II-2})$$

The Knudsen number is defined $\text{Kn} = \frac{\lambda}{L}$. Thus,

$$\text{Kn} = \frac{2\mu RT}{L\bar{V}} \frac{1}{p} \quad (\text{II-3})$$

and for an isothermal flow, Kn and p are inversely proportional.

* As a general reference, see Chapman, S. and T. O. Cowling, The Mathematical Theory of Non-Uniform Gases, Cambridge University Press, 1964.